applied sciences

Spatial Analysis for Landscape Changes

Edited by
Dario Gioia and Maria Danese

Printed Edition of the Special Issue Published in *Applied Sciences*

www.mdpi.com/journal/applsci

MDPI

Spatial Analysis for Landscape Changes

Spatial Analysis for Landscape Changes

Editors

Dario Gioia
Maria Danese

MDPI • Basel • Beijing • Wuhan • Barcelona • Belgrade • Manchester • Tokyo • Cluj • Tianjin

Editors
Dario Gioia
Institute of Science of the Cultural Heritage
Italy

Maria Danese
CNR
Istituto di Scienze del Patrimonio Culturale
Italy

Editorial Office
MDPI
St. Alban-Anlage 66
4052 Basel, Switzerland

This is a reprint of articles from the Special Issue published online in the open access journal *Applied Sciences* (ISSN 2076-3417) (available at: https://www.mdpi.com/journal/applsci/special_issues/SALC).

For citation purposes, cite each article independently as indicated on the article page online and as indicated below:

LastName, A.A.; LastName, B.B.; LastName, C.C. Article Title. *Journal Name* **Year**, *Volume Number*, Page Range.

ISBN 978-3-0365-2862-5 (Hbk)
ISBN 978-3-0365-2863-2 (PDF)

Contents

About the Editors

Dario Gioia was born in Lagonegro (Potenza, Italy) the 20th July, 1979 and earned his first degree in Geological Sciences at the University of Basilicata, with a thesis in morphotectonics. He received a PhD in 2009 at the University of Basilicata, with a dissertation dealing with the morphotectonic evolution of the Auletta basin (southern Apennines, Italy). At present, he is a researcher at the Istituto di Scienze del Patrimonio Culturale of the Italian National Council of Research (ISPC-CNR), and his research activity is mainly focused on studies of geomorphological hazard due to slope, fluvial and costal geomorphological processes, and its relationship with cultural and monumental heritage. He is the coordinator of several national projects of the ISPC-CNR, dealing with the analysis of geomorphological processes in areas of high cultural and archaeological value. From 2005, he has been involved as a member in many research projects dealing with issues of geomorphology and Quaternary geology. Moreover, his research activity includes participation as a member of several project programs, such as the National Relevant Research Projects (PRIN) program of the Italian Ministry for the University and Research (MIUR), LIFE and European Fund for Regional Development (EFRD) of the EU. In the March 2017, he qualifies as an Associate Professor of Physical Geography and Geomorphology. Dario Gioia works in the fields of tectonic geomorphology, geomorphological hazard geoarchaeology, landslide mapping and monitoring, the morphometry of drainage networks, and the stratigraphical and structural evolution of tectonic basins. His activity is also focused on the topics of quantitative and theoretical geomorphology such as the application of the Landscape Evolution Model (LEM) to investigate the recent evolution of fluvial and coastal environments and the development of geomorphic indexes to solve issues of landscape/landform classification. His research methodological approaches include geomorphological and geological surveys and photo-aerial interpretation, DEM-supported morphometric studies of landscape and river network evolution, and satellite- and field-based monitoring of landslide activity. He is the co-author of more than 90 papers, 50 of which are published in ISI journals with an impact factor. He is usually the referee of relevant international journals such as *Earth Surface Processes* and *Landforms, Geomorphology* and *Journal of the Geological Society* and has recently been a guest editor for high-impact journals' Special Issues on quantitative geomorphology.

Maria Danese was born in Potenza (Italy) and received her first degree in Engineering, Planning and Territorial Management at the University of Basilicata, with a thesis on spatial analysis and urban planning. She achieved a PhD at the University of Pisa, with a dissertation dealing with spatial autocorrelation and its application in urban planning, seismic risk, archaeology and material pattern decay. At present, she is a researcher at the Institute of Heritage Science of the Italian National Council of Research (ISPC-CNR), and her research activity is mainly focused on Geographic Information Science applied to cultural heritage, from archaeological predictive models, to integrated risk analysis, to remote sensing; from the management of heritage data to support for diagnostics and analysis of the architectural and artistic heritage. She is the co-author of more than 100 papers, many of which are published in ISI journals with an impact factor. She is usually the referee of relevant international journals.

applied sciences

MDPI

Editorial

Spatial Analysis for Landscape Changes

Dario Gioia * and Maria Danese *

ISPC-CNR, C.da S. Loja, Tito Scalo, I-85050 Potenza, Italy
* Correspondence: dario.gioia@cnr.it (D.G.); maria.danese@cnr.it (M.D.)

Landscape is the backcloth over which environmental and anthropic events occur, and recent increasing trends of natural and anthropic processes, such as urbanization, land-use changes, and extreme climate events, have a strong impact on landscape modification. Indeed, day by day, landscape changes are becoming more drastic and faster and there is a growing need for the implementation of effective instruments, tools, and approaches to understand and manage them. A great improvement in the availability of high-resolution DEMs, GIS tools, and algorithms of automatic extraction of landform features and change detections has favored an increase in the analysis of landscape changes, which became an essential instrument for the quantitative evaluation of landscape changes in many research fields. This special issue collects six papers that highlight the usefulness of the quantitative analyses of satellite images and DEMs to solve multidisciplinary issues of landscape changes.

Rui et al. (2020) [1] introduce an analysis of the erosion factors controlling the evolution of a badland area of the National Geological Park of Qian, China. The influence of geological features, climate, groundwater, and soil on the geomorphological evolution of the study area has been discussed, in order to reconstruct a synoptic scheme of the main stages of morpho-evolution.

Yan et al. (2020) [2] describe an interesting approach of the semi-automatic extraction of subaqueous landforms using multibeam bathymetric data. The comparison of three different methods of landform classification (i.e., Wood's criteria, SOM, and geomorphons) highlights that the geomorphon method has the highest degree of accuracy for the automatic extraction of the bedforms of a delta system in China.

Gioia and Schiattarella (2020) [3] investigated the scenarios of sediment flux variation and topographic changes due to dam removal in a small catchment of the southern Italian Apennines. The application of a landscape evolution model (i.e., the Caesar Lisflood LEM) provides a detailed reconstruction of the abrupt geomorphological change induced by base-level fall due to dam removal, which can be roughly summarized in the significant increase in the erosion ability of the main channels and a strong incision of the reservoir infill.

Martinez et al. (2021) [4] integrate satellite images and drone surveys to investigate the post-fire vegetation regeneration in a forest in Central-Eastern Spain. The spatial analysis of the topographic and image attributes and the application of vegetation indexes indicate that a similar analysis can be useful to evaluate the effect of post-fire vegetation restoration strategies.

Subudhi et al. (2021) [5] propose a new method of image segmentation of hyperspectral satellite images (i.e., the Superpixel-based SSA, SP-SSA), which can provide an improvement to the capturing of object-specific spatio-spectral information. The performance of the method is evaluated using an SVM classifier, suggesting that the proposed approach overperforms the standard SSA technique and various common spatio-spectral classification methods, in terms of classification accuracy.

Finally, Danese and Gioia (2021) present a review paper aimed at the bibliometric analysis of the research trends in the topic of the special issue, "Spatial Analysis for Landscape Changes". Such an analysis covers the last twenty years and investigates topics, trends, and methods that are connected to the research line through the statistical analysis

Citation: Gioia, D.; Danese, M. Spatial Analysis for Landscape Changes. *Appl. Sci.* **2021**, *11*, 11924. https://doi.org/10.3390/app112411924

Received: 6 December 2021
Accepted: 13 December 2021
Published: 15 December 2021

of different metrics, such as the number of citations, co-authorship networks, and keyword occurrences. The results of the bibliometric analysis highlight that the topic has received increasing attention in the last years, and research methods are moving toward computer-based automation or the unsupervised detection of landscape patterns and changes.

Author Contributions: All authors contributed equally to the preparation of this manuscript. All authors have read and agreed to the published version of the manuscript.

Funding: This research received no external funding.

Acknowledgments: This publication was only possible with the invaluable contributions from the authors, reviewers, and the editorial team of Applied Sciences.

Conflicts of Interest: The authors declare no conflict of interest.

References

1. Rui, X.; Nie, L.; Xu, Y.; Du, C.; Kong, F.; Zhang, T.; He, Y.; Wang, Y. Characterization of Evolution Stages, Groundwater and Soil Features of the Mud Forest Landscape at Qian-an (China). *Appl. Sci.* **2020**, *10*, 7427. [CrossRef]
2. Yan, G.; Cheng, H.; Teng, L.; Xu, W.; Jiang, Y.; Yang, G.; Zhou, Q. Analysis of the Use of Geomorphic Elements Mapping to Characterize Subaqueous Bedforms Using Multibeam Bathymetric Data in River System. *Appl. Sci.* **2020**, *10*, 7692. [CrossRef]
3. Gioia, D.; Schiattarella, M. Modeling Short-Term Landscape Modification and Sedimentary Budget Induced by Dam Removal: Insights from LEM Application. *Appl. Sci.* **2020**, *10*, 7697. [CrossRef]
4. Martinez, J.L.; Lucas-Borja, M.E.; Plaza-Alvarez, P.A.; Denisi, P.; Moreno, M.A.; Hernández, D.; González-Romero, J.; Zema, D.A. Comparison of Satellite and Drone-Based Images at Two Spatial Scales to Evaluate Vegetation Regeneration after Post-Fire Treatments in a Mediterranean Forest. *Appl. Sci.* **2021**, *11*, 5423. [CrossRef]
5. Subudhi, S.; Patro, R.; Biswal, P.K.; Dell'Acqua, F. Superpixel-Based Singular Spectrum Analysis for Effective Spatial-Spectral Feature Extraction. *Appl. Sci.* **2021**, *11*, 10876. [CrossRef]

applied sciences

MDPI

Article

Characterization of Evolution Stages, Groundwater and Soil Features of the Mud Forest Landscape at Qian-an (China)

XiangJian Rui, Lei Nie, Yan Xu *, Chao Du, FanSheng Kong, Tao Zhang, YuanYuan He and YuZheng Wang

Construction Engineering College, Jilin University, Changchun 130026, China; ruixj17@mails.jlu.edu.cn (X.R.); nielei@jlu.edu.cn (L.N.); duchao18@mails.jlu.edu.cn (C.D.); kongfs19@mails.jlu.edu.cn (F.K.); zhangtao18@mails.jlu.edu.cn (T.Z.); hyy20@mails.jlu.edu.cn (Y.H.); yuzhengw18@mails.jlu.edu.cn (Y.W.)
* Correspondence: xuyan8102@jlu.edu.cn

Received: 27 September 2020; Accepted: 21 October 2020; Published: 22 October 2020

Abstract: The research on geological landscape has received more and more attention worldwide. The National Geological Park of Qian-an mud forest, located in Qian-an Country, Songyuan City (Jilin Province, China) is a rare natural geological landscape formed by erosion. Mud forest landscape has undergone long-term geological processes, and it is still in continuous evolution due to subsurface erosion. In the process of the mud forest landscape formation and evolution, distinct stages have been recognized. The subsurface erosion factors of the mud forest area were identified by groundwater and soil samples characterization, and the mechanism of the formation of the mud forest is studied. Results show that the occurrence of subsurface erosion is controlled by four factors: (1) The head difference of terrace increases due to geological structure, (2) The dry and cold paleoclimate increases the accumulation of soluble salts. Concentrated precipitation in the short term also promotes subsurface erosion. (3) The high content of sodium ions in groundwater promotes the dispersion of soil, and (4) Loess-like soil is characterized by high porosity, low plasticity, and dispersibility.

Keywords: mud forest; erosion; subsurface erosion; landscape formation; landscape evolution; loess-like soil

1. Introduction

Soil erosion is a global problem and poses major issues in many countries [1,2]. Soil erosion can increase run-off by changing soil properties and particularly by destroying topsoil structure and reducing water holding capacity [3,4]. Soil erosion is not only a land degradation process, but also a geomorphological appearance [5]. When the rate of soil erosion exceeds the rate of soil formation, the process of land degradation helps shaping the natural geological landscape [6]. In other words, while soil erosion causes land degradation, it also forms some typical landscapes (Table 1). Kuhn, et al. [7] studied the effect of rainfall on the Zin Valley badlands in Israel. "Calanchi" and "biancane" are two typical badland landscapes in Italy. Ciccacci, et al. [8] analyzed the evolution of "biancane" landforms, whereas Pulice, et al. [9] investigated how topography and rainfall may affect runoff and slope processes in "calanchi" landforms. Most of the soil erosion landscapes studied above are gully shaped or round enveloped landscapes formed by surface erosion. The research object of this paper is a columnar geological landscape formed by both surface and subsurface erosion. As seen in Table 1, the studied landscapes are mainly composed of earth pillars, arranged together looking like a forest, hence it was named "mud forest" [10,11].

Table 1. Several typical geological landscapes formed by soil erosion. [7–9,12,13].

Name	State	Picture
Zin Valley badlands	Israel	
Badland landscape	Spain	
"Calanchi" badland landform	Italy	
"Biancane" badland landform	Italy	
Yuanmou Dry-hot Valley	China	
Mud forest landscape	China	

The process of erosion is caused by both surface and subsurface processes. Over the last decades, most studies on soil erosion have focused on surface processes, such as sheet, rill and gully erosion [5,14]. Although subsurface erosion has been reported to be a significant and widespread process, the disproportion in the number of studies on surface erosion compared to those on subsurface erosion is striking [5,15]. Subsurface erosion generally refers to various forms of erosion caused by groundwater below the surface [16]. This process and its effects have been described under a variety of names: subterranean erosion [17], subcutaneous erosion [18], sinking of the ground [19–21], sink-hole erosion [22,23], tunnel erosion [24], pothole gullying [25], tunnel-gully erosion [26,27], tunneling erosion [28], piping [29], soil piping [30], pothole erosion [31], and suffusion [32–34]. While degradation occurs in all kinds of landscapes over the world, the drivers of degradation vary from region to region [35]. Due to the complexity of subsurface erosion, no single factor can be held responsible for subsurface erosion development [5]. Vannoppen, et al. [36] pointed out that the

occurrence of subsurface erosion is controlled by soil and climate features [37–41]. The occurrence of subsurface erosion is also closely related to topography [42–45].

In 2009, the Qian-an mud forest landscape was officially approved as a national geological park in China. Due to its unique landform caused by erosion, this landscape has become the only protected "mud forest" site in China with these geological features, giving the area a high aesthetic and scientific investigation value [46]. However, mud forest is a very fragile geological landscape and suffers from serious soil erosion. In order to maintain mud forest stable for a long time, it is necessary to understand the causes of such landscape degradation. Previous researches on mud forest landscape have been carried out, including the formation mechanism, development and utilization, slope failure. Zhu and Liang [47] preliminarily analyzed the formation mechanism of the mud forest landscape. Zhou, Wang, Ren, Cai and Zhang [10] believed that the formation of the mud forest landscape was related to landform and wind force. On the basis of previous studies, Chi, Wang and Yang [11] proposed that the formation and development of mud forests were not only related to external factors, but also related to soil composition. Zhang et al. [48] concluded that the frost weathering is an important factor in the damage in the region. However, the formation mechanism of the mud forest has not been clearly analyzed since the influence of interflow was ignored in previous studies. In order for this landscape to remain stable for a long time, it is necessary to understand the causes of landscape evolution.

Therefore, this study focused on the role of subsurface erosion in the formation and evolution of the mud forest landscape, by using different evolution stages to describe such landscape development more intuitively. At the same time, the factors affecting the subsurface erosion in mud forest area were analyzed in details in order to provide theoretical basis for landscape protection.

2. Materials and Methods

2.1. Study Area

The National Geological Park of Qian-an mud forest is located in the southwest of Qian-an Country, Songyuan City, Jilin Province (Figure 1). It is 40 km away from Qian-an Country, across Suozi Town and Dabusu Town. The coordinates are longitude 123°36′–123°42′ and latitude 44°45′–44°50′, with a total area of 110 km^2. Mud forest scenic spot is located in the Dabusu nature reserve, and the area of the mud forest landscape is 7.5 km^2.

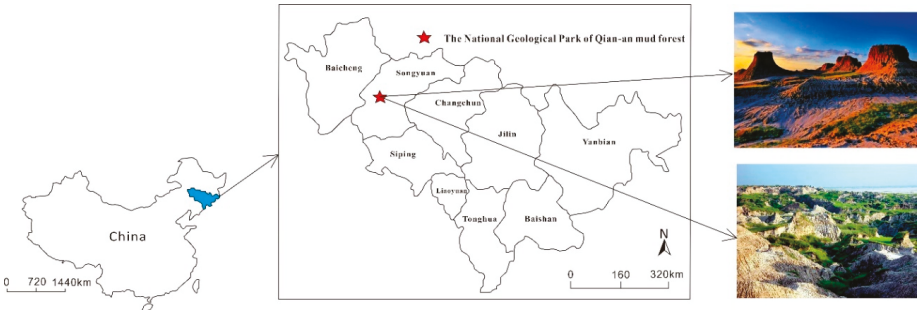

Figure 1. Location of the National Geological Park of Qian-an mud forest and mud forest landscape.

The study area has a continental arid and semi-arid monsoon climate in the north temperate zone. This climate zone presents the distinctive climate characteristics of dry and windy springs, warm and rainy summers, cool and short autumns, and long and cold winters. The perennial average temperature in the area is 4.7 °C. January records the lowest low temperature at −14.8 °C, while in July the temperature is 24.9 °C. Average annual precipitation is about 400–500 mm and two-thirds of this amount occurs in June, July, and August. The average sunshine duration reaches 2900 h within a year. The frost-free days are 145 per year. The vegetation in the study area is characterized by

meadow grassland. In the park there are 274 species of plants in 51 families, including huangying, sedge, hornwort, and *achnatherum splendens*.

The study area is distributed in the western alluvial plain of the Songnen Plain. The terrain is sloped from east to west and from south to north due to neotectonic movement. The elevation is 150–170 m in the east and 140–155 m in the west. This results in no transit rivers in the Qian-an area. However, a series of lake depressions closely related to the ancient channel are left, forming a relatively independent closed-stream area. In the west of the Songnen Plain, there are many lakes and marshes. Preliminary statistics shows that nearly 700 lakes exist within an area of over 6 km^2. Dabusu Lake is a large inland lake among these lakes [10]. Because of the hot weather in summer, the evaporation is much larger than precipitation, which causes a large accumulation of saline and alkaline substances near Dabusu Lake. Dabusu Lake has a low altitude and it is the center of groundwater gathering. Dabusu Lake receives the joint replenishment of atmospheric precipitation, surface runoff and subsurface current. The catchment area is nearly 230 km^2, and the lake basin area is about 81 km^2. As shown in Figure 2, there are 10 gullies in the west and 4 gullies in the east of Dabusu Lake.

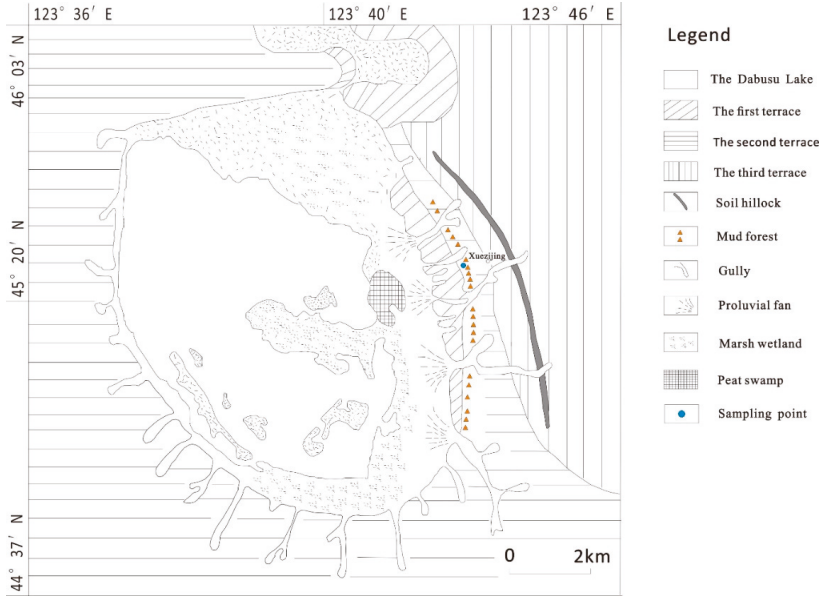

Figure 2. Dabusu Lake area plan.

The Songnen Plain, where the Dabusu Lake is located, is a basin type plain that has been continuously settled since Mesozoic and Cenozoic era and accumulated huge thickness of Mesozoic sediments. The basement of Songnen Plain is the metamorphic rock series of the pre-Jurassic period, and the caprock is the meso-Cenozoic deposit with a thickness of 4000–5000 m. According to relevant data, the stratigraphic lithology of Qian-an area is shown in Table 2 [10]. Dabusu mud forest geomorphologic landscape was produced in Guxiangtun formation (upper Pleistocene), consisting in silt, silty clay and clay. The mud forest area is located in the secondary terrace on the east side of Dabusu Lake (Figure 2). This area is located in the middle of the central sag of the secondary structure of the Songliao giant subsidence zone. Soils in the study area are characterized by poor profile differentiation and the area is classified as Cambisols according to the World Reference Base for Soil Resources (WRB) [49].

Table 2. Stratigraphic lithology of Qian-an area [10].

Geologic Symbols	Chronolithologic Unit	Lithostratigraphic Unit	Burial Depth (m)	Formation Thickness (m)	Lithology
Q4	Quaternary Holocene	-	0–1	0–1	Cultivated soil
Q_3g	Quaternary upper Pleistocene system	Guxiangtun formation	1–18	15–34	Loess-like soil
			18–34		Fine sand

The mud landscape geomorphologic group is mainly distributed in the leading edge of terraces, and the earth pillar height is 10–15 m. Figure 3 shows the geological evolution diagram of the mud forest landscape area. On the basis of the formation process of Mesozoic, early Pleistocene and middle Pleistocene, the area experienced the late Pleistocene lake paleogeographic depositional environment. The formation in this area is characterized by loess-like soil in the upper part and fine sand in the lower part. After the early late Pleistocene deposition, the crust in this area underwent the process of uplift in the east and depression in the west and inclination in the northwest in Neoid period. In the middle of late Pleistocene, due to the uplift of the crust in the Neoid period, erosion and subsurface erosion are intensified, thus forming the characteristic geological and geomorphic landscape of the mud forest. As subsurface erosion continues, the landscape of the mud forest is still changing.

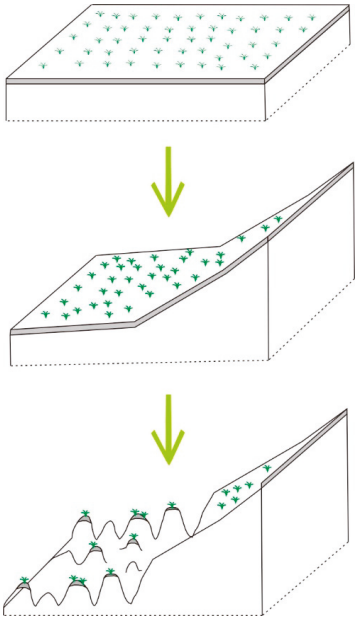

Figure 3. A schematic geological evolution diagram of the mud forest landscape area.

2.2. Field Survey and Laboratory Test

A detailed field survey was conducted in the study area in order to assess different evolution stages of the mud forest landscapes. In order to study the influence of soil on the subsurface erosion in mud forest area, three soil samples were collected between soil pillars at a depth of 10 cm, namely C1, C2, and C3. Three groundwater samples were also collected for experimental study, namely N1, N2, and N3 (Figure 2). The main ions content of groundwater and soluble salt in soil samples were measured. The test methods are shown in Table 3. The groundwater chemistry was analyzed

by piper diagrams and categorized by the Gibbs' model. In the piper diagrams in Figure 4a: (i) In region 1, alkali earth metal ions are greater than alkali metal ions. (ii) In region 2, alkali metal ions are greater than alkali earth metal ions. (iii) In region 3, weak acid root ions are greater than strong acid root ions. (iv) In region 4, strong acid root ions are greater than weak acid root ions. (v) In region 5, the carbonate hardness is greater than 50%. (vi) In region 6, the noncarbonate hardness is greater than 50%. (vii) In region 7, noncarbonate bases are greater than 50%. (viii) In region 8, carbonate base is greater than 50%. (ix) In region 9, no pairs of cation-anion were greater than 50%. Based on the analysis of water in the world's rivers, lakes and major oceans, Gibbs [50] believes that the controlling factors of ion origin can be divided into rock weathering type, atmospheric precipitation control type and evaporation-concentration type. Figure 4b shows the distribution principle of the Gibbs model.

Table 3. Test method for chemical composition of groundwater and soluble salt in soil samples.

Test Item	Method
HCO^-_3	Double indicator neutralization
Cl^-	Silver nitrate titration
$SO_4{}^{2-}$	Mass method
Ca^{2+}, Mg^{2+}	EDTA coordination titration
Na^+, K^+	Flame photometry
pH	pHS-3C tester

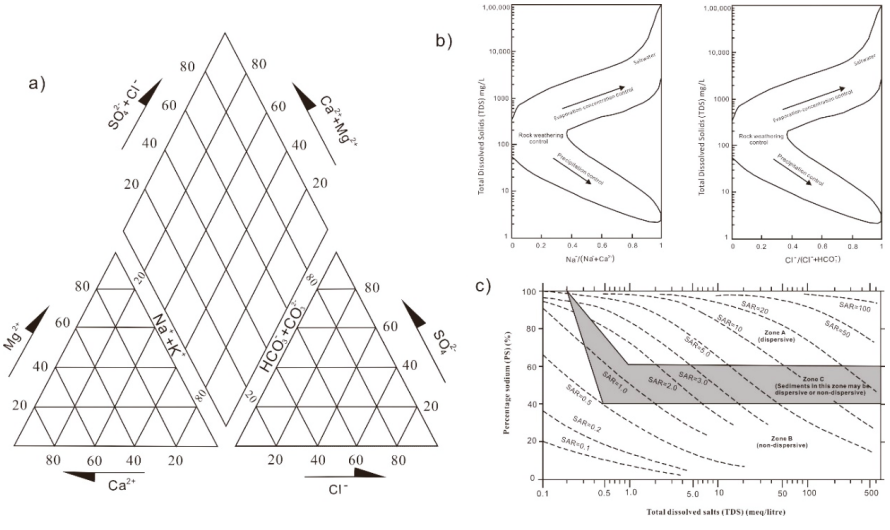

Figure 4. Methods used in the experimental analysis: (**a**) Piper diagrams. (**b**) Gibbs model. (**c**) Sherard diagram.

Grain size distribution was measured by a combination of sieving and hydrostatic sedimentation methods. The natural density was measured by cutting ring method. Natural moisture content was measured by means of drying. Liquid limit and plastic limit were determined by the combined determination of liquid limit and plastic limit. Porosity was measured by mercury injection. Major chemical elements were determined via X-ray fluorescence spectrometry following the analytical procedure of Franzini et al. [51] and Leoni and Saitta [52]. This method uses powder pellets and is based on the full matrix correction method. Total volatile components (H_2O and CO_2) were determined as loss on ignition (LOI) at 950 °C on powders dried at 105 °C [53–55]. Considering the high ion content of the soil sample, the double hydrometer method was not suitable, so the dispersibility of the soil sample was determined by Sherard diagram [56]. Several parameters are necessary to determine whether the soil has

dispersibility [57,58], among them: the "sodium adsorption ratio", SAR = $Na^+/[(Ca^{2+} + Mg^{2+})/2]1/2$; the "percentage sodium", PS = $[Na^+/(Na^+ + K^+ + Ca^{2+} + Mg^{2+})] \times 100$; the "total dissolved salts", TDS = $Na^+ + K^+ + Ca^{2+} + Mg^{2+}$. Sherard, Dunnigan and Decker [56] correlated TDS, SAR, PS and clay dispersibility (Figure 4c), according to these authors, the clays of zone A have a high tendency for spontaneous dispersion, the sediments of zone C may be dispersive or nondispersive and the materials of zone B are ordinary erosion-resistant clays [55].

3. Results and Discussion

3.1. Mud Forest Landscape Fetaures and Evolution Stage

According to the field investigation, it was found that the mud forest landscape in the study area is characterized by distinct stages, named infant stage, juvenile stage, youth stage and old stage. These four stages reflect to the germination, formation, development and extinction stages of the mud forest landscape (Figure 5).

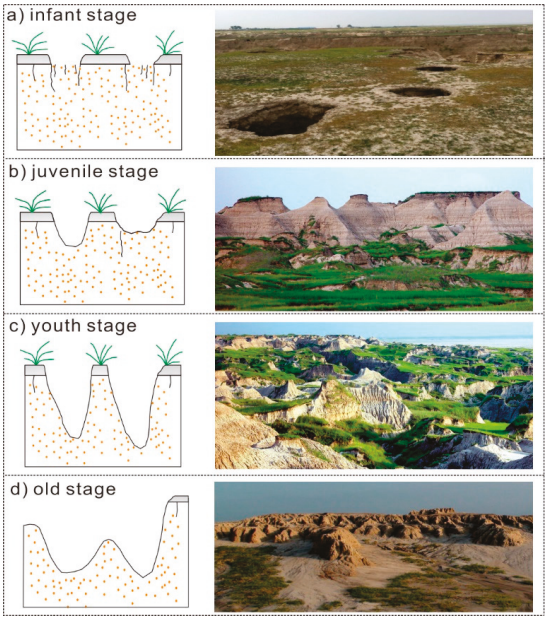

Figure 5. Geomorphologic evolution and different periods of the mud forest landscapes: (**a**) the infant stage; (**b**) the juvenile stage; (**c**) the youth stage; and (**d**) the old stage.

In the infant stage, because of surface erosion, small patches of cultivated soil are destroyed and the vegetation cannot grow. This exposed the loess-like soil directly (Figure 6a). First, the lack of cultivated soil layer makes terrain concave. Precipitation tends to accumulate there. Second, due to the lack of vegetation protection, the exposed loess-like soil is more conducive to rainfall infiltration. Precipitation penetrates along pores and vertical joints (Figure 5a). The eluviation makes the joints and fissures of loess-like soil enlarge. During long years of erosion, small cracks expand to form caves. Due to the special physical and chemical properties of loess-like soil, it is easy to disintegrate and dissolve when meeting water. This causes the soil layer to be vulnerable to subsurface erosion, thus expanding the cave range. Under the action of gravity, the top layer of soil collapses, creating holes (Figure 6b). With the continuation of the subsurface erosion, the sinkholes and the horizontal suffusion caves are developed. Some vertical sinkholes have also been formed (Figure 6c).

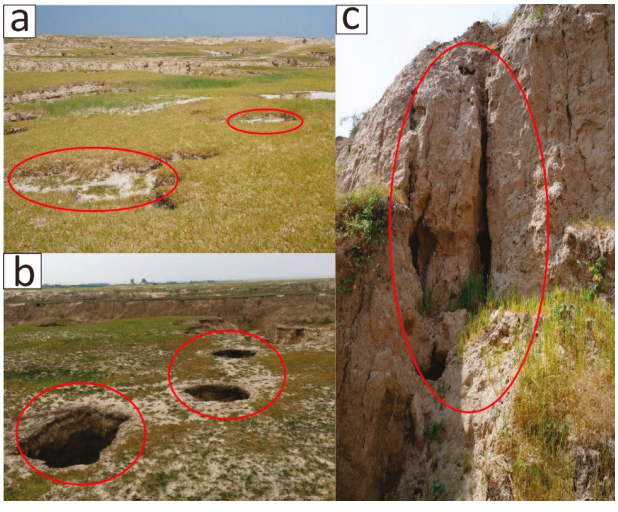

Figure 6. Geomorphologic features of the infant stage of mud forest evolution. (**a**) The lack of vegetation on a small area of the earth's surface leaves the loess-like soil exposed; (**b**) Many holes are shaped by subsurface erosion; (**c**) Vertical sinkhole are formed by subsurface erosion.

In the next juvenile stage, a large number of holes were formed. With the passage of time and the continuous occurrence of erosion, these holes expanded leading to a destruction of terraces integrity. Gradually, gullies of different sizes and shapes formed, showing accordingly the form of "island" (Figure 5b).

With further development of dissolution and subsurface erosion, the ornamental value of the mud forest reaches its peak in the youth stage of landscape development. The solitary peaks are irregular and varied in shape. Some look like conical and humped forms (Figure 5c).

After reaching the peak of mud forest landscape development, subsurface erosion continues to occur. However, continued subsurface erosion will begin to destroy the mud forest landscape. The mud forest landscape gradually loses its charm and looks like a series of small raised planes from a distance (Figure 5d). Although its form is unique, its ornamental value is far less than the youth stage of the mud forest landscape. This is the old stage of the mud forest landscape, it is also a stage of landscape degradation. At present, most of the mud forest landscape is in this stage.

3.2. Groundwater Analyses

The milligram equivalent percentage of each ion was calculated according to the content of each component of the groundwater (Table 4). It is easy to see that sodium ions account for the largest milligram equivalent percentage of cations, at 55.31%. Calcium ions were the second, accounting for 35.91%. Among the anions, chlorine ions accounted for 55.22%, which was the largest proportion of anions. The bicarbonate ions accounted for 37.92%. Water sample was analyzed by Piper diagrams [57,58]. The sample plots fall under zone 2, 4, and 7 (Figure 7). According to the Shukalev classification method, the groundwater chemistry in the study area is of type HCO_3 + Cl-Na + Ca. The calculated $Na^+/(Na^+ + Ca^{2+})$ value is greater than 0.6 and $Cl^-/(Cl^- + HCO^-_3)$ value is close to 0.5. The groundwater test data was plotted in the Gibbs model. The water sample plots the slightly upper right side of the model center (Figure 8). This reflects that the water characteristics in this region are controlled by evaporation and crystallization.

Table 4. Physical and chemical properties and main ion content of groundwater.

Test Item	Value (mg/L)	Test Item	Value (meq/L)	Milligram Equivalent Percentage (%)
Visible substances	White and turbid	SO_4^{2-}	2.065	6.86
Water temperature	15 (°C)	Cl^-	16.617	55.22
pH	7.01	HCO^-	11.411	37.92
ORP	127.1	Na^+	20.955	55.31
Water hardness	842.8	K^+	0.018	0.047
Total dissolved solids	2184	Ca^{2+}	13.605	35.91
Water alkalinity	571.1	Mg^{2+}	3.307	8.73

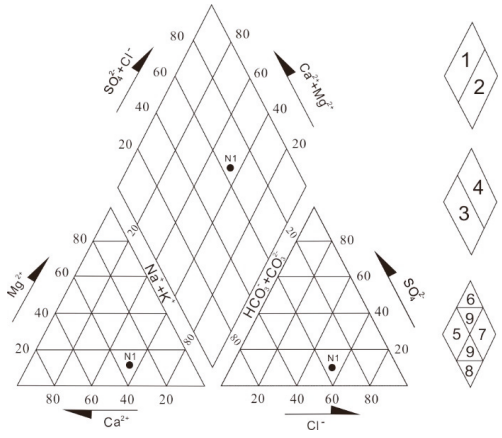

Figure 7. Piper diagrams of major ions in groundwater sample in the mud forest area.

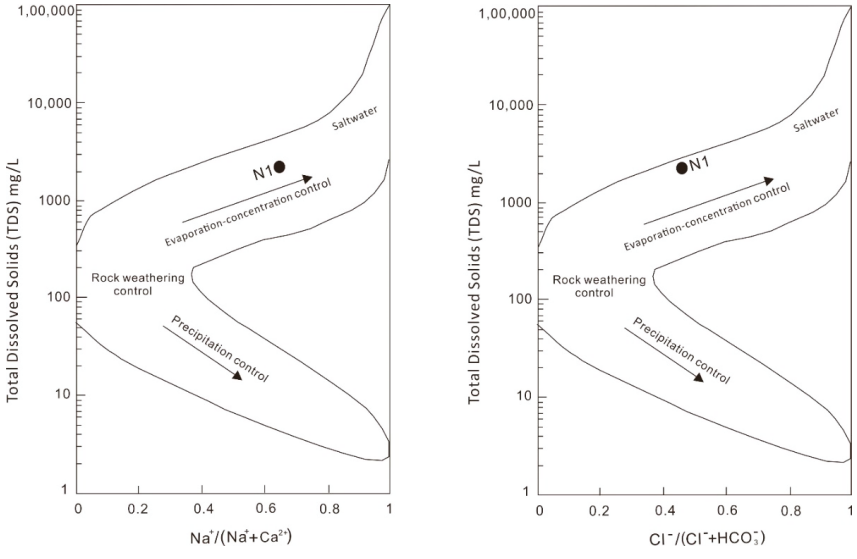

Figure 8. Plot of the major ions within the Gibbs model for groundwater in study area.

3.3. Soil Features

The development of subsurface erosion landform is closely related to soil properties. The soil that forms mud forest landform is a kind of loess-like soil (Figure 9). The results show that (a) all particles are smaller than 0.5 mm, (b) fine particle fraction (clay and silt) is more than three quarters, (c) a silt fraction (0.005–0.075 mm) accounts for the largest proportion, more than half. The soil was then classified as lean clay (CL) based on the Unified Soil Classification System (USCS) [57,58].

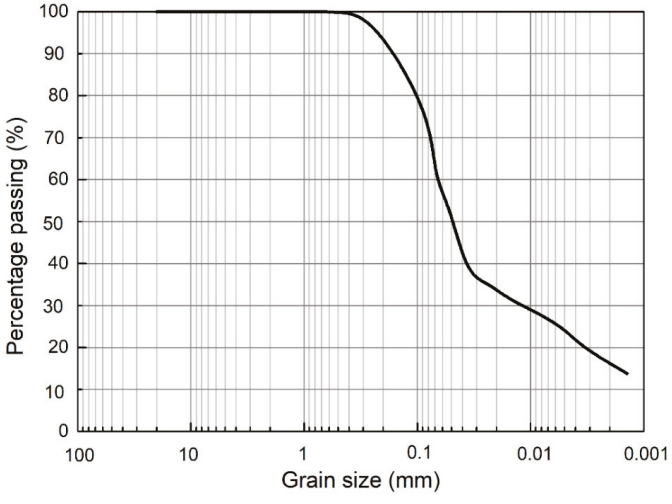

Figure 9. Grain size distribution of loess-like soil.

Table 5 shows the physical properties of loess-like soil sample, including particle size composition, plasticity index, liquid index, porosity, etc. Silt content accounts for 52%, which is the highest proportion. The plasticity index value of soil sample is low, and the liquid index is less than 0. The porosity of the soil sample is 57.46%.

Table 5. List of physical properties of loess-like soil sample.

Item	Value
Clay content (%)	24.42
Silt content (%)	52.75
Sand content (%)	22.83
Natural density (g/cm^3)	1.44
Natural moisture content (%)	13.23
Liquid limit (%)	26.78
Plastic limit (%)	18.26
Liquidity index	−0.59
Plasticity index	8.52
Soil classification	CL
Porosity (%)	57.46

Chemical composition of loess-like soil can be seen in Table 6. From the oxide composition, the content of silicon dioxide is the highest, followed by alumina. This is similar to the composition of loess. Due to the high content of calcium oxide, magnesium oxide and potassium oxide, it proves that the soil formation environment is relatively dry and cold. The calculated silicic acid coefficient ($Ki = SiO_2/Al_2O_3$) of the sample is 7.93. The larger Ki value indicated that the loess-like soil was formed

when the climate was relatively arid. Therefore, the soil was formed in a dry and cold environment by the analysis of the oxide content of the sample.

Table 6. Chemical composition of loess-like soil (major element, in wt.%).

SiO_2	Al_2O_3	Fe_2O_3	FeO	CaO	MgO	K_2O	Na_2O	TiO_2	P_2O_5	MnO	LOI
77.38	9.76	1.26	0.54	4.29	1.16	2.96	2.24	0.58	0.07	0.07	4.74

Clay dispersibility is a good indicator of the dispersion vulnerability of soil and, therefore, of the associated risks of soil erosion [57]. The soluble salt composition of soil sample investigated in the present study is given in Table 7, together with the calculated SAR, PS and TDS. The salt composition affects the properties of loess-like soil, especially dispersibility. Plotting of values presented in Table 7 in Sherard diagram clearly shows the zone of soil samples. All samples plot zone A (Figure 10). This indicates that the soil in mud forest area is dispersive.

Table 7. Soluble salt content (meq/L) and related parameters controlling clay dispersibility.

	Na^+	K^+	Ca^{2+}	Mg^{2+}	SO_4^{2-}	Cl^-	HCO^-	TDS	PS	SAR
C1	7.844	0.014	1.896	0.301	1.623	4.011	4.865	10.055	78.011	7.484
C2	7.452	0.011	1.513	0.228	1.733	5.255	3.586	9.204	80.965	7.987
C3	8.041	0.010	1.577	0.285	1.137	5.550	4.254	9.913	81.116	8.334

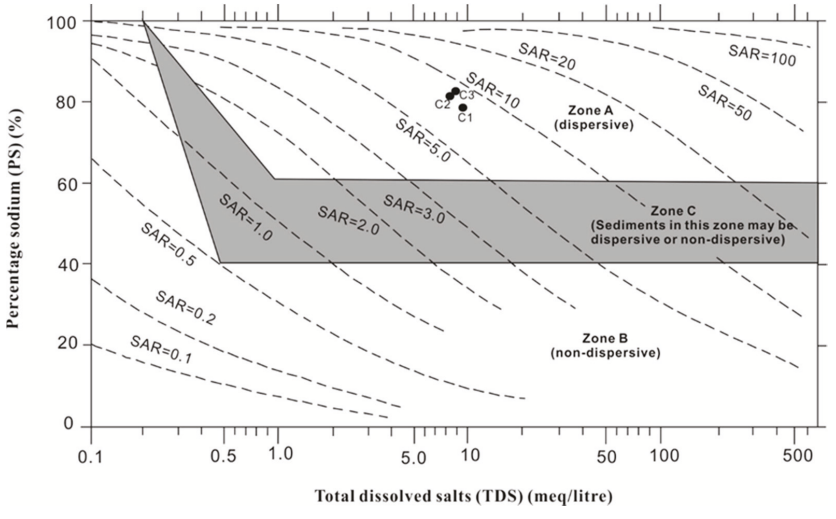

Figure 10. Relationships between clay dispersibility (susceptibility to colloidal dispersion) and salt composition (expressed through the PS, TDS and SAR parameters defined in Table 7).

3.4. Influence of Environmental Factors on Subsurface Erosion

Songnen Plain, a basin-like concave plain, provides a site for the formation of the mud forest landforms. Since the terrain is slightly concave, groundwater and precipitation tend to accumulate there. This, to some extent, aggravates the occurrence of subsurface erosion. During the Neoid period, gullies formed along the cutting of the earth's crust provided the possibility of erosion and subsurface erosion. Moreover, the uplift caused the inclined rise to the northwest, accompanied by new fault activities, which led to the asymmetry of landform between the east and west sides of the Dabusu Lake (Figure 11). Therefore, erosion and subsurface erosion on the east bank are more intense.

The asymmetry of the lake banks is not only the reason why the mud forest landscape began to occur, but also an important geological factor in the subsurface erosion that the mud forest is still experiencing.

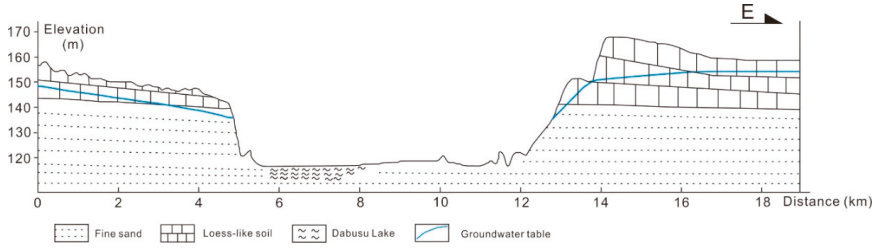

Figure 11. Profile of Dabusu Lake and its banks.

Due to the control and influence of neotectonic movement, the uplift of Xuezijing was active. In the late Pleistocene (about ten thousand years ago), there was a local uplift in Xuezijing, and the front edge of the second terrace formed a steep ridge more than 20 m high. The leading edge of the terrace floor was raised, showing an abnormal phenomenon that the front edge of the terrace slopes towards the back edge. The height difference between front edge and back edge was nearly 1 m. The terrace floor shows a north-south extension, with high in the middle, low on both sides. As the climate was dry and the ground rose again, the lake level dropped. Long-term, intense erosion and subsurface erosion occurred in lakeshore gullies.

Zhu and Liang [47] took sporopollen samples from the late Pleistocene lacustrine deposits and analyzed them. The results showed that the main sporopollen of woody plants were pinaceae and betulaceae, and the main sporopollen of herbaceous plants were artemisia and chenopodiaceae, ephedra and other drought-tolerant plant sporopollen also could be seen. This indicated that the Late Pleistocene climate was a dry and cold climate. This climate period corresponds to the Dali ice age in China. Fossils of fauna that lived in cold climates, such as mammoths and woolly rhinoceros, have been found, confirming a dry and cold climate. In this dry and cold environment, the lake water evaporates and condenses, increasing the salinity of the lake. The lake water with high salt content is deposited in direct contact with the sediments. This exacerbates the dissolution of soluble salts in loess-like soil. Thus, it is more prone to occur subsurface erosion.

Affected by the temperate monsoon climate, the study area is hot and rainy in summer and cold and dry in winter. Southwest winds prevail in the study area, with strong spring winds. The average annual wind speed is 4.1 m/s and the average annual maximum wind speed is 28.2 m/s [59]. Large amounts of clay and salt are blown toward the lakeshore. During the summer, some of the material is carried back into the lake by the wind. This ongoing wind cycle has a profound impact on molding the shape and physical structure of the lake basin. At present, the mud forest geological and geomorphic landscape is exposed to the wind, so the cutting and shaping of the lake basin and mud forest by wind force factors cannot be ignored. In addition, precipitation in summer is also a feature of this climate type. Annual precipitation is 400–500 mm [59]. In June, July and August, the precipitation reaches two-thirds of the annual precipitation. The average annual precipitation in summer is 359.9 mm [60]. Concentrated rainfall in a short period causes the exposed loess-like soil to be eroded. With the occurrence of rainfall infiltration and subsurface erosion, the geomorphology of mud forest changes and promotes the evolution and degradation of the mud forest landscape.

The formation and development of the mud forest geomorphic landscape is also closely related to the occurrence and movement of groundwater around it. Dabusu Lake and its surrounding areas are not only the center of precipitation and surface water collection in the Songnen alluvial plain, but also the center of groundwater collection. In addition, it is a confined water basin with multiple aquifers, which is rich in groundwater. Due to the uplift of the crust during the uplift period and the new faulting activities, the shallow groundwater was exposed. The Quaternary confined water may also

be exposed. So, the gully where the mud forest geological and geomorphic landscape is located is almost always filled with water. This provides a long-term underground water-rich environment for the formation of subsurface erosion geomorphology.

The buried groundwater level in the study area is shallow (Figure 11). The average groundwater level is 15.2 m. So the hydraulic gradient near the lakeshore is high. This leads to serious seepage damage of the soil. The subsoil of loess-like soil is a fine sand layer with good permeability. The water in the river is complementary through this highly permeable layer. Moreover, due to the high permeability of soil layer, groundwater has a higher velocity, and the decomposed soil particles can be carried away in time. As shown in Figure 12, infiltration of the precipitation converges with groundwater flow, continuously eroding loess-like soil, and over time, the mud forest landform landscape is formed. The content of sodium ion in water is higher, and it has the ability to disperse colloidal substance. At the same time, as this type of water circulates through the soil, it can increase the soluble salt content in the soil. While this is also an important reason for the degradation and destruction of the mud forest landscape.

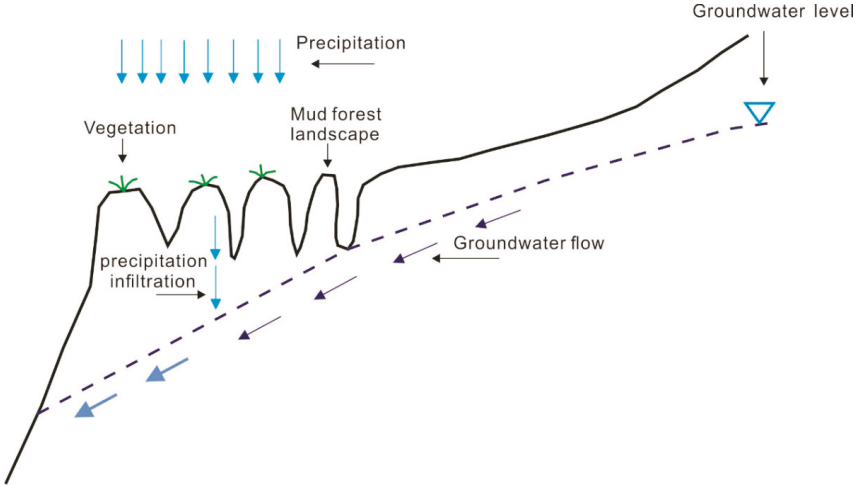

Figure 12. Groundwater flow and precipitation infiltration in mud forest area.

The results of the soil particle analysis tests showed that the soil sample contained the largest proportion of fine particles. While fine and very fine sand fractions were most important in controlling soil erosion [61], the high content of fine grained soil and weak hydrophilicity of the silt promoted the development of subsurface erosion in mud forest areas. Soil has no plasticity, more prone to subsurface erosion damage. Larger porosity of loess-like soil in mud forest area can promote the occurrence and development of subsurface erosion. Because the pores provide channels for the erosion products, accelerating the subsurface erosion process. The soil in mud forest area is dispersive (Figure 10). Thus, loess-like soil has a great propensity to produce a colloidal dispersion when groundwater flows through. After colloidal dispersed, small particles are carried along the pores by the water flow, forming cracks. Dispersive clays develop large pipes and erosion tunnels through rapid enlargement of small cracks and fissures as a consequence of the spontaneous dispersion of clays lining the fissure walls when these come in contact with water. This promotes subsurface erosion, thereby exacerbating the degradation of the mud forest landscape.

4. Conclusions

Mud forest landscape is a rare erosion landscape protected by the state because of its unique environmental features. In recent years, mud forest geological landscape began to degrade. In this paper, the evolution of the mud forest landscape was described, and the mechanisms for such evolution were analyzed.

After geological survey and analysis, mud forest landscape is the product of long-term geological processes. It is found that the mud forest landscape is in a dynamic evolution process. Therefore, it is named the dynamic evolution of the mud forest landscape into four stages in chronological order as infant stage, juvenile stage, youth stage and old stage, reflecting the evolution process of its formation to its extinction.

Therefore, it is discussed the factors that promote the subsurface erosion process in mud forest area and analyzed the influence of geological features, climate, groundwater and soil. It includes that: (1) The east and west banks are asymmetric, and the erosion of the east bank is more intense. Local uplift and lower lake levels lead to greater head differences; (2) The dry and cold paleoclimatic provides the environmental factor for the subsurface erosion, and the present arid-semiarid climate also facilitates the subsurface erosion; (3) There is abundant groundwater in the mud forest area, which provides a water-rich environment for the subsurface erosion. The groundwater is controlled by evaporation and concentration type, it provided abundant soluble salt for the soil in the cycle and promoted the occurrence of subsurface erosion; and (4) Loess-like soil has high content of silty grains, poor hydrophilicity, poor soil plasticity, and high porosity. It also has dispersibility, which makes it prone to subsurface erosion in contact with water. This is the root cause of subsurface erosion in mud forest areas.

Author Contributions: Data curation, X.R. and L.N.; Formal analysis, X.R., L.N. and Y.X. and C.D.; Funding acquisition, Y.X. and L.N.; Investigation, X.R., F.K. and Y.W.; Methodology, X.R., L.N. and T.Z.; Writing—original draft, X.R. and Y.H.; Writing—review & editing, Y.X and C.D. All authors have read and agreed to the published version of the manuscript.

Funding: This research received financial support from the Natural Science Foundation of China (grant no.41702300), (grant no.41502270), and (grant no. 41572254).

Acknowledgments: The authors are grateful for financial support from the National Natural Science Foundation of People's Republic of China (grant no.41702300), (grant no.41502270), and (grant no. 41572254). We wish to thank the testing science experiment center of Jilin University for supporting the experiment. We would also like to thank the Jilin Dabusu National Nature Reserve Administration for supporting our research work.

Conflicts of Interest: The authors declare no conflict of interest.

References

1. Guerra, A.J.T.; Fullen, M.A.; Jorge, M.d.C.O.; Bezerra, J.F.R.; Shokr, M.S. Slope Processes, Mass Movement and Soil Erosion: A Review. *Pedosphere* **2017**, *27*, 27–41. [CrossRef]
2. García-Ruiz, J.M.; Beguería, S.; Lana-Renault, N.; Nadal-Romero, E.; Cerdà, A. Ongoing and Emerging Questions in Water Erosion Studies. *Land Degrad. Dev.* **2016**, *28*, 5–21. [CrossRef]
3. Hui, L.; Xiaoling, C.; Lim, K.J.; Xiaobin, C.; Sagong, M. Assessment of soil erosion and sediment yield in Liao watershed, Jiangxi Province, China, Using USLE, GIS, and RS. *J. Earth Sci.* **2010**, *21*, 941–953. [CrossRef]
4. Lucà, F.; Buttafuoco, G.; Terranova, O. GIS and Soil. In *Comprehensive Geographic Information Systems*; Huang, B., Ed.; Elsevier: Oxford, UK, 2017; Volume 2, pp. 37–50.
5. Bernatek-Jakiel, A.; Poesen, J. Subsurface erosion by soil piping: Significance and research needs. *Earth Sci. Rev.* **2018**, *185*, 1107–1128. [CrossRef]
6. Alewell, C.; Egli, M.; Meusburger, K. An attempt to estimate tolerable soil erosion rates by matching soil formation with denudation in Alpine grasslands. *J. Soils Sediments* **2014**, *15*, 1383–1399. [CrossRef]
7. Kuhn, N.J.; Yair, A.; Grubin, M.K. Spatial distribution of surface properties, runoff generation and landscape development in the Zin Valley Badlands, northern Negev, Israel. *ESPL Earth Surface Processes Landf.* **2004**, *29*, 1417–1430. [CrossRef]

8. Ciccacci, S.; Galiano, M.; Roma, M.A.; Salvatore, M.C. Morphological analysis and erosion rate evaluation in badlands of Radicofani area (Southern Tuscany—Italy). *Catena* **2008**, *74*, 87–97. [CrossRef]
9. Pulice, I.; Di Leo, P.; Robustelli, G.; Scarciglia, F.; Cavalcante, F.; Belviso, C. Control of climate and local topography on dynamic evolution of badland from southern Italy (Calabria). *Catena* **2013**, *109*, 83–95. [CrossRef]
10. Zhou, X.; Wang, C.; Ren, G.; Cai, W.; Zhang, B. The genetic characteristics of the Dabusu mud forest, and its protection and development suggestions. *Jilin Geol.* **2003**, *22*, 62–67. (In Chinese)
11. Chi, Y.; Wang, Q.; Yang, J. Formation of Qian'an "Mud Forest" in Jilin Province. *J. Eng. Geol.* **2006**, *14* (Suppl. S1), 174–178. (In Chinese)
12. Regüés, D.; Nadal-Romero, E. Uncertainty in the evaluation of sediment yield from badland areas: Suspended sediment transport estimated in the Araguás catchment (Central Spanish Pyrenees). *Catena* **2013**, *106*, 93–100. [CrossRef]
13. Chen, A.; Zhang, D.; Yan, B.; Lei, B.; Liu, G. Main types of soil mass failure and characteristics of their impact factors in the Yuanmou Valley, China. *Catena* **2015**, *125*, 82–90. [CrossRef]
14. Lucà, F.; Conforti, M.; Robustelli, G. Comparison of GIS-based gullying susceptibility mapping using bivariate and multivariate statistics: Northern Calabria, South Italy. *Geomo* **2011**, *134*, 297–308. [CrossRef]
15. Poesen, J. Soil erosion in the Anthropocene: Research needs. *ESPL Earth Surface Processes Landf.* **2018**, *43*, 64–84. [CrossRef]
16. Li, X.; Song, Y.; Ye, W. *Engineering Geological Research on Tunnel-Ersion in Loess*; Tongji University Press: Shanghai, China, 2010; p. 151. (In Chinese)
17. Fuller, M.L. Some unusual erosion features in the Loess of China. *Geogr. Rev.* **1922**, *12*, 570–584. [CrossRef]
18. Guthrie-Smith, H. *Tutira: The Story of a New Zealand Sheep Station*, 2nd ed.; William Black Wood and Sons: London, UK; Edinburgh, Germany, 1926.
19. Rubey, W.W. Gullies in the Great Plains formed by sinking of the ground. *Am. J. Sci.* **1928**, *15*, 417–422. [CrossRef]
20. Wang, T.; He, F.; Zhang, A.; Gu, L.; Wen, Y.; Jiang, W.; Shao, H. A quantitative study of gully erosion based on object-oriented analysis techniques: A case study in Beiyanzikou catchment of Qixia, Shandong, China. *Sci. World J.* **2014**, *2014*, 417325. [CrossRef]
21. Buckham, A.F.; Cockfield, W.E. Gullies formed by sinking of the ground. *Am. J. Sci.* **1950**, *248*, 137–141. [CrossRef]
22. Thorp, J. Geography of the Soils of China. *Geogr. J.* **1940**, *96*, 57.
23. Cockfield, W.E.; Buckham, A.F. Sink-hole erosion in the White Silts at Kamloops, 3rd series. *R. Soc. Can. Trans.* **1946**, *40*, 1–10.
24. Bennett, H.H. *Soil Conservation*; McGraw-Hill: NewYork, NY, USA, 1939.
25. Cole, R.C.; Koehler, L.F.; Eggers, F.C.; Goff, A.M. The Tracy area, California. U.S. *Dep. Agric. Soil Surv. Ser.* **1943**, *1938*, 1–95.
26. Gibbs, H.S. Tunnel gully erosion on the Whithers Hills. *N. Z. J. Sci. Technol.* **1945**, *27*, 135–146.
27. Laffan, M.D. *The Soils and Tunnel-Gully Erosion of a Small Catchment in the Wither Hills*; Lincoln College, University of Canterbury: Christchurch, New Zealand, 1973.
28. Downes, R.G. Tunneling erosion in northeastern Victoria. *Aust. Counc. Sci. Ind. Res. J.* **1946**, *19*, 283–292.
29. Fletcher, J.E.; Carroll, P.H. Some properties of soils associated with piping in Southern Arizona. *Soil Sci. Soc. Am. J.* **1948**, *13*, 545–547. [CrossRef]
30. Carroll, P.H. Soil piping in south-eastern Arizona. United States Department of Agriculture, Soil Conservation Service, Region 6, Albuquerque, New Mexico. *Reg. Bull. 110 Soil Ser.* **1949**, *13*, 1–21.
31. Kingsbury, J.W. Pothole erosion on the western part of Molokai Island, Hawaii. *Territ. Hawaii. J. Soil Water Conserv.* **1952**, *7*, 197–198.
32. Czeppe, Z. Zjawiska sufozyjne w glinach zboczowych górnej części dorzecza Sanu [Suffosional phenomena in slope loams of the Upper San drainage basin]. *Biul. Inst. Geol. Z Badań Czwartorzędu* **1960**, *9*, 297–324.
33. Galarowski, T. New observations of the present-day suffosion (piping) processes in the Bereźnica catchment basin in The Bieszczady Mountains (The East Carpathians). *Stud. Geomorphol. Carpatho-Balc.* **1976**, *10*, 115–122.
34. Pavlov, A.P. About relief of plain sand its change under the influence of subsurface and surface water. *Geosciences* **1898**, *5*, 91–147.

35. Wieland, R.; Lakes, T.; Yunfeng, H.; Nendel, C. Identifying drivers of land degradation in Xilingol, China, between 1975 and 2015. *Land Use Policy* **2019**, *83*, 543–559. [CrossRef]
36. Vannoppen, W.; Verachtert, E.; Poesen, J. Pipeflow response in loess-derived soils to precipitation and groundwater table fluctuations in a temperate humid climate. *Hydrol. Process.* **2017**, *31*, 586–596. [CrossRef]
37. Jones, J.J.A. Soil piping and its hydrogeomorphic function. *Cuatern. Geomorfol.* **1994**, *8*, 77–102.
38. Faulkner, H. Piping Hazard on Collapsible and Dispersive Soils in Europe. In *Soil Erosion in Europe*; Wiley: Hoboken, NJ, USA, 2006; pp. 537–562.
39. Verachtert, E.; Van Den Eeckhaut, M.; Poesen, J.; Deckers, J. Factors controlling the spatial distribution of soil piping erosion on loess-derived soils: A case study from central Belgium. *Geomorphology* **2010**, *118*, 339–348. [CrossRef]
40. Zhang, T.; Wilson, G.V. Spatial distribution of pipe collapses in Goodwin Creek Watershed, Mississippi. *Hydrol. Process.* **2013**, *27*, 2032–2040. [CrossRef]
41. Leslie, I.N.; Heinse, R.; Smith, A.M.S.; McDaniel, P.A. Root Decay and Fire Affect Soil Pipe Formation and Morphology in Forested Hillslopes with Restrictive Horizons. *Soil Sci. Soc. Am. J.* **2014**, *78*, 1448–1457. [CrossRef]
42. Zhu, T. Gully and tunnel erosion in the hilly Loess Plateau region, China. *Geomo* **2012**, *153–154*, 144–155. (In Chinese) [CrossRef]
43. Atallah, N.; Shakoor, A.; Watts, C.F. Investigating the potential and mechanism of soil piping causing water-level drops in Mountain Lake, Giles County, Virginia. *Eng. Geol.* **2015**, *195*, 282–291. [CrossRef]
44. Holden, J. Controls of soil pipe frequency in upland blanket peat. *J. Geophys. Res.* **2005**, *110*, 1–11. [CrossRef]
45. Goldsmith, P.R.; Smith, E.H. Tunnelling soils in South Auckland, New Zealand. *Eng. Geol.* **1985**, *22*, 1–11. [CrossRef]
46. Rui, X.; Nie, L.; Xu, Y.; Wang, H. Land Degeneration due to Water Infiltration and Sub-Erosion: A Case Study of Soil Slope Failure at the National Geological Park of Qian-an Mud Forest, China. *Sustainability* **2019**, *11*, 4709. [CrossRef]
47. Zhu, Q.; Liang, X. A preliminary syudy on the origin of the "Wolf's fang shaped" topography on the eastern bank of the Dabusu lake. *Jilin Geol.* **1991**, *1*, 75–78. (In Chinese)
48. Zhang, W.; Chen, J.; Xu, Y. Destruction causes of subsurface flow in mud forest along bank of Dabusu Lake. *J. Hohai Univ. (Nat. Sci.)* **2017**, 197–203. (In Chinese)
49. IUSS Working Group WRB. *World Reference Base for Soil Resources 2014: International Soil Classification System for Naming Soils and Creating Legends for Soil Maps*; Food and Agriculture Organization of the United Nations: Rome, Italy, 2014.
50. Gibbs, R.J. Mechanisms Controlling World Water Chemistry. *Am. Assoc. Adv. Sci.* **1970**, *170*, 1088–1090. [CrossRef] [PubMed]
51. Franzini, M.; Leoni, L.; Saitta, M. A simple method to evaluate the matrix effects in X-Ray fluorescence analysis. *X-ray Spectrom.* **1972**, *1*, 151–154. [CrossRef]
52. Leoni, L.; Saitta, M. X-ray fluorescence analysis of 29 trace elements in rock and mineral standards. *Rend. Societa Ital. Mineral. Petrol.* **1976**, *32*, 497–510.
53. Tertian, R.; Claisse, F. *Principles of Quantitative X-ray Fluorescence Analysis*; Heyden: London, UK, 1982.
54. Wobrauschek, P. Total reflection x-ray fluorescence analysis—A review. *X-ray Spectrom.* **2007**, *36*, 289–300. [CrossRef]
55. Battagliaa, S.; Leonib, L.; Sartorib, F. Mineralogical and grain size composition of clays developing calanchi and biancane erosional landforms. *Geomorphology* **2003**, *49*, 153–170. [CrossRef]
56. Sherard, J.L.; Dunnigan, L.P.; Decker, R.S. Identification and nature of dispersive soils. *ASCE J. Geotech. Eng. Div.* **1976**, *102*, 287–301.
57. Mitchell, J.K. *Fundamentals of Soil Behavior*; Wiley: New York, NY, USA, 1976; p. 422.
58. Head, K.H. *Manual of Soil Laboratory*; Pentech Press: London, UK; Paris, France, 1988; Volume 2.
59. Xia, C. *Dynamic Remote Sensing Analysis of Sandy Desertification in West Jilin Province*; Jilin University: Changchun, China, 2017.

60. Ma, J.; Wang, X. Summer Climate Characteristics and Effects in Songyuan. *Yuan Lin Sheng Tai* **2014**, *13*, 65.
61. Manyevere, A.; Muchaonyerwa, P.; Mnkeni, P.N.S.; Laker, M.C. Examination of soil and slope factors as erosion controlling variables under varying climatic conditions. *Catena* **2016**, *147*, 245–257. [CrossRef]

applied sciences

MDPI

Article

Analysis of the Use of Geomorphic Elements Mapping to Characterize Subaqueous Bedforms Using Multibeam Bathymetric Data in River System

Ge Yan [1], Heqin Cheng [1,2,*], Lizhi Teng [1], Wei Xu [1], Yuehua Jiang [3], Guoqiang Yang [3] and Quanping Zhou [3]

1 State Key Laboratory of Estuarine and Coastal Research, East China Normal University, Shanghai 200000, China; yang13@lzu.edu.cn (G.Y.); 51163904014@stu.ecnu.edu.cn (L.T.); 52152601001@stu.ecnu.edu.cn (W.X.)
2 Institute of Eco-Chongming, Shanghai 200000, China
3 Nanjing Geological Survey Center, China Geological Survey, Nanjing 210000, China; jyuehua@mail.cgs.gov.cn (Y.J.); yangguoqiang@mail.cgs.gov.cn (G.Y.); zquanping@mail.cgs.gov.cn (Q.Z.)
* Correspondence: hqch@sklec.ecnu.edu.cn; Tel.: +86-21-54836006

Received: 2 September 2020; Accepted: 26 October 2020; Published: 30 October 2020

Featured Application: This work has application in separating subaqueous dune areas from the flat bed and assessing the scouring risk associated with the pit distribution. It verifies the feasibility of applying landscape analysis methods to characterize subaqueous micro-topography.

Abstract: Riverbed micro-topographical features, such as crest and trough, flat bed, and scour pit, indicate the evolution of fluvial geomorphology, and have an influence on the stability of underwater structures and overall scour pits. Previous studies on bedform feature extraction have focused mainly on the rhythmic bed surface morphology and have extracted crest and trough, while flat bed and scour pit have been ignored. In this study, to extend the feature description of riverbeds, geomorphic elements mapping was used by employing three geomorphic element classification methods: Wood's criteria, a self-organization map (SOM) technique, and geomorphons. The results showed that geomorphic element mapping can be controlled by adjusting the slope tolerance and curvature tolerance of Wood's criteria, using the map unit number and combination of the SOM technique and the flatness of geomorphons. Relatively flat bed can be presented using "plane", "flat planar", and "flat" elements, while scour pit can be presented using a "pit" element. A comparison of the difference between parameter settings for landforms and bedforms showed that SOM using 8 or 10 map units is applicable for land and underwater surface and is thus preferentially recommended for use. Furthermore, the use of geomorphons is recommended as the optimal method for characterizing bedform features because it provides a simple element map in the absence of area loss.

Keywords: multibeam; flat bed; scour pit; Wood's criteria; self-organization map; geomorphons

1. Introduction

Bedforms in river flows have an effect on bed roughness, flow conditions, and sediment transportation [1]. From an engineering perspective, they often present major navigation problems as they can reduce the local water depth. A large number of navigation channel regulations have been implemented and associated work has been conducted, which has changed the morphology and hydrodynamic behavior of rivers such as the Yangtze River. As bedforms are not static, it is also important to analyze them prior to laying pipelines and cables. In this respect, a multibeam echosounding system provides high-resolution bathymetric data that show the terrain of bedforms,

and extracting the features of bedforms from bathymetric data has thus been the focus of intensive research in recent years.

Many studies have focused on extracting the crest and trough of bedforms because height, wavelength, and asymmetry of bedforms provide an indication of the flow velocity and direction [2,3]. In this respect, a bedform tracking tool was developed to automatically detect the locations of crests and troughs from the curves of profiles [4–6]. In addition, Van Dijk et al. [7] used a geostatistical filter to generate crest and trough lines as a set of points from the filtered bathymetric surface, and Debese et al. [8] used geodesic morphology to extract the salient crest and trough lines of sand structures in three dimensions. However, for a flow with an increasing strength, many typical bedforms can be formed, such as ripples, dunes, anti-dunes, lower flat beds, and upper flat beds [9–11]. Flat beds are also identified as plane beds in some studies [12–14]. A flat bed is a widely spreading bedform in a river's subaqueous environment, and it may not contain many crest and trough features. The complicated development and spatial distribution of the bedform cannot be comprehensively identified using only crest and trough. In addition, scour pits can be contained in troughs with varying elevations with manual inspection, as indicated in many studies [15–18]. Therefore, a greater detailed geomorphic element layer is required to describe the texture or roughness information of features such as flat and plane beds, and scour pits. Particularly, scour pits have an influence on the stability of underwater structures.

Studies that previous classified terrestrial landform elements were used as a reference in this study, as the elements of flat, plane, and pit can be detected via variations in the terrain using these classification methods or techniques. Wood [19] developed criteria for dividing the land's surface into six elements (plane, pit, peak, ridge, valley, and pass) based on four morphometric parameters (slope, cross-sectional curvature, maximum curvature, and minimum curvature). Ehsani and Quiel considered the aforementioned four factors as the input vectors for the self-organization map (SOM) to classify terrain surface by training [20]. In the SOM technique, 10 elements are defined (including flat planar, gentle slope ridge, and gentle slope channel). Jasiewicz et al. used geomorphons instead of geomorphometric variables to divide the surface into flat, pit, valley, ridge, peak, shoulder, footslope, hollow, and spur elements based on the visual angle [21]. A fuzzy method [22] and an object-based method [23] have also been used to classify elements; however, they are relatively complicated to use. A few attempts have been made to apply Wood's criteria and geomorphons in the sea environment. For example, Stefano and Mayer [24] found that the use of geomorphons was superior to Wood's criteria for describing submarine sand waves, and Cui et al. [25] modified geomorphons to detect seafloor hill, depression, ridge, valley, shoulder, and foot-slope. However, these methods have not been used in the subaqueous environment of rivers, and the approach and features with respect to using these methods to characterize river bedforms are currently unclear.

This study aimed to conduct an experiment on extending the extraction of the following bedform features: the crest and trough of dunes, flat beds, and scour pits. Three methods, including Wood's criteria, the SOM technique, and geomorphons, were selected to map the geomorphic elements and to describe the bedforms of the river system, as it is relatively simple to implement all these methods. Although there is no pit-related element, the SOM technique was used to characterize bedforms as it contains the description of flat, ridge, and valley.

2. Materials and Methods

2.1. Study Area and Data

The geomorphic system from the lower reaches of the Yangtze River to the estuarine delta has undergone varying degrees of adaptive adjustment in recent years. The lower reaches of Datong (located in Chizhou City) are affected by the tide of the East China Sea, and they thus belong to the tidal reach area [26]. Numerous engineering construction projects have been implemented in the Yangtze River Estuary, and these have caused extension of the fluctuating section of the tidal zone [27].

The rise in relative sea level will ultimately lead to a rise in the tide level and changes in the dynamic conditions of the Yangtze River Estuary area. In addition, aggravation of river channel erosion in the mouth of the Yangtze River has seriously impacted the evolution of the river channel in the middle and lower reaches of the Yangtze River [28,29]. Therefore, in the past decade, many underwater micro geomorphology surveys and researches using multi-beam sounding systems have been conducted in the tidal reach area [16–18,30,31]. With respect to the importance of studying this area, the tidal reach region is also the focus of this study (see Figure 1a).

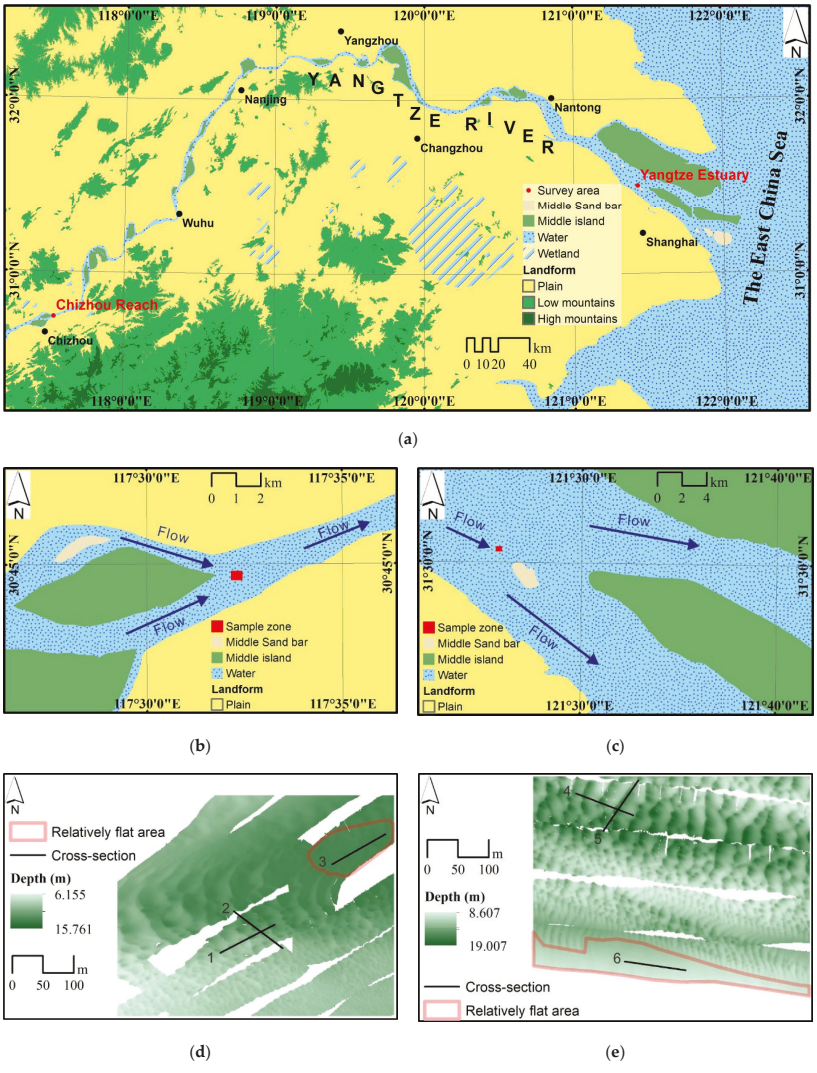

Figure 1. (**a**) Location of the two bathymetric survey areas in Yangtze River, (**b**) geomorphologic environment surrounding Chizhou Reach, and (**c**) that of the Yangtze Estuary. (**d**) Sample data for Chizhou Reach and (**e**) Yangtze Estuary. Six cross-sections were set in the sample zones and used to compare the water depth profiles with the distribution of mapped geomorphic elements.

Two bathymetric datasets were collected from the end and start of the tidal reach respectively, and were used as study cases (Figure 1a). The measurements of the first set were collected in Chizhou Reach within the Yangtze River (Figure 1b) where two flows converge in one direction, and the channel width ranges from 1 to 2 km (approximately), and those for the second set were collected in the North Port Channel of the Yangtze Estuary (Figure 1c) where the flow diverges in two directions and the channel width ranges from 4 to 10 km (approximately). Bathymetric point cloud data were acquired using a SeaBat 7125 multibeam system operating at a frequency of 400/200 kHz and DGPS (Differential Global Position System) -positioned. Data were input into PDS2000 software (Version 4.2.16, Teledyne RESON, Rotterdam, The Netherlands) to generate a grid model with a resolution of 1 × 1 m. Two sample zones (Figure 1d,e), both with an area of 450 × 360 m^2, were cut from the grid model and used to compare the feasibility of the three geomorphic element mapping methods. The two aforementioned zones were representative of dune and relatively flat areas. Interpretation by manual inspection separated dune areas and relatively flat areas, as shown in Figure 1d,e.

The water depth for the sample data of Chizhou Reach ranges from 6.155 to 15.761 m (Figure 1d), and the depth of the Yangtze Estuary ranges from 8.607 to 19.007 m (Figure 1e). Both sample zones contained blank areas with NODATA value that is always represented by −9999 in files in ASCII format. The actual areas excluding NODATA value were 131,041 and 138,623 m^2, respectively.

2.2. Wood's Criteria

Wood [19] used morphometric parameters, including slope and three curvatures, to classify geomorphic features relating to plane, pit, ridge, channel, peak, and pass. The aforementioned four parameters were calculated based on the study of Evans [32]. Wood [19] defined a set of criteria for defining geomorphic elements by comparing the aforementioned four parameters with slope tolerance and curvature tolerance (Table 1). Slope tolerance separates flat surfaces from slopes, and curvature tolerance separates planar surfaces from ridges and channels.

Table 1. Wood's criteria for the classification of geomorphic elements.

Slope	Cross-Sectional Curvature	Maximum Curvature	Minimum Curvature	Class Output
>Slope tolerance (Sloping surface)	>Curvature tolerance	-	-	Ridge
	< – Curvature tolerance	-	-	Channel
	<Curvature tolerance > – Curvature tolerance	-	-	Plane
<Slope tolerance (Horizontal surface)	-	>Curvature tolerance	>Curvature tolerance	Peak
	-	>Curvature tolerance	< – Curvature tolerance	Pass
	-	< – Curvature tolerance	< – Curvature tolerance	Pit
	-	> – Curvature tolerance	< – Curvature tolerance	Channel
	-	<Curvature tolerance	> – Curvature tolerance	Plane
	-	>Curvature tolerance	<Curvature tolerance > – Curvature tolerance	Ridge

The GRASS GIS version 7.6.1 (GRASS Development Team, Beaverton, OR, USA) provides a tool, r.param.scale, that directly implements Wood's criteria by adjusting the value of slope tolerance and curvature tolerance. The use of different slope and curvature tolerance settings enables the drawing of distinct geomorphic elements maps. This study aimed to determine suitable tolerance settings to be applied in extracting bedforms' features.

2.3. SOM Technique

The SOM technique also calculates the four parameters referred to in Wood's criteria; however, it combines the four parameters into an input vector to train the SOM. The SOM is a realistic model based on the function of the biological brain [33]. Formally, the SOM commonly arranges output map units in the form of one, two, or three dimensions and connects them to input vectors via weights. Close input vectors within the space are clustered into units that are also close [34,35]. This means that

surface points can be considered to be the same geomorphic element if their input vectors are very close compared to others.

In this study, the SOM technique was used in MATLAB 2019b (The MathWorks, Natick, MA, USA) via the command "newsom." Prior to learning, four input parameters were normalized to the range of 0–1, as indicated in previous researches [20,36]. The number of iterations affects the amount of computation required; therefore, to reduce the mapping time, it is necessary to control the iterations. The iteration values of rough tuning and fine tuning were thus set as 100 and 100, respectively. The number and combination of output map units was preset, as it is impossible to determine which number will provide a meaningful classification. Following the learning phase, the trained SOM was used to classify the geomorphic elements based on the input vectors for each cell, and the optimal number and the corresponding output were selected after analysis. One of the aims of this study was to determine a suitable map unit combination that enabled the identification of bedforms' features.

2.4. Geomorphons

Jasiewicz and Stepinski [21] identified local geomorphic elements using local ternary patterns [37]. In this respect, a ternary pattern depicts the terrain type in the adjacent domain of the central cell through quantifying the local surface using the line-of-sight principle [38].

Using this principle, eight elevation profiles beginning in the central cell and extending to the "lookup distance" along eight principal compass directions can be drawn from the digital elevation model (DEM) to calculate the zenith and nadir angles in the central cell. Using a comparison between zenith (ϕ_L^D) and nadir angles (ψ_L^D), Equation (1) can thus be employed to calculate a slot denoted by the symbol, Δ_L^D, where D is the direction and L is the lookup distance,

$$\Delta_L^D = \begin{cases} 1 & if \quad \phi_L^D - \psi_L^D < -t \\ 0 & if \quad \left|\phi_L^D - \psi_L^D\right| \le t \\ -1 & if \quad \phi_L^D - \psi_L^D > t \end{cases}. \tag{1}$$

As each elevation profile has one slot, 8 slots can be calculated for a ternary pattern. Based on the numbers of (−1) and (+1) in the slots, a lookup table established by Jasiewicz and Stepinski [21] can then be used to define 10 geomorphic elements: flat, pit, ridge, valley, peak, shoulder, spur, slope, hollow, and foot-slope.

The GRASS GIS version 7.6.1 provides a tool "r.geomorphon" for implementing geomorphons. The author wrote that the geomorphons in MATLAB 2019b extend the flatness to 0°, which cannot be used as a flatness value in GRASS GIS. The flatness threshold, t, is a kernel parameter which influences the mapping results. Therefore, another aim of this study was to find the suitable flatness setting for bedforms' features.

3. Results

3.1. Wood's Criteria-Based Geomorphic Elements Mapping for Describing Subaqueous Bedforms

The local range of the surface used to calculate the morphologic parameters is limited to the size of the window. If the size is too small, such as 3 × 3 m, the output will be substantially influenced by meaningless roughness relating to errors; however, if the size is too large, NODATA values will be attributed to more cells near the boundary. Therefore, a reasonable size of traversing window was set as 7 × 7 m in this study. Slope tolerance and curvature tolerance are two key parameters controlling classification. As shown in Figure 2, a larger area is regrouped into plane when the curvature tolerance is larger, while more ridge, pit, and pass can be defined when the slope tolerance is larger. Curvature tolerance should be set within 0.005–0.05, as this can provide an output that is close to eye-based recognition of the relatively flat area.

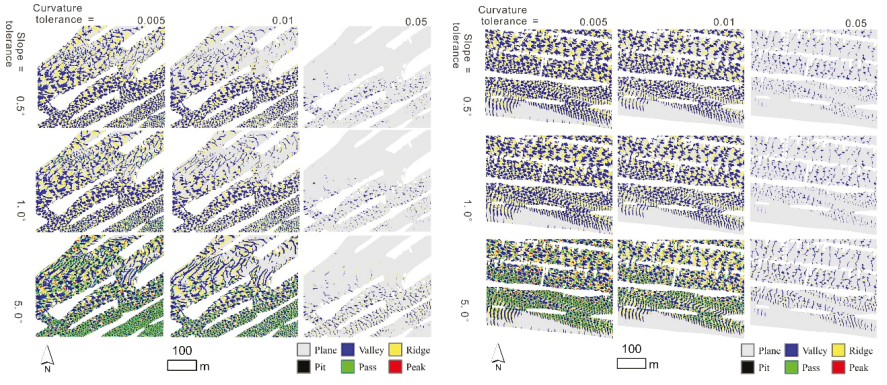

(**a**) (**b**)

Figure 2. Wood's criteria-based distribution of geomorphic elements with different slope tolerance in rows and curvature tolerances in columns for the sample data of (**a**) Chizhou Reach of the Yangtze River and (**b**) the Yangtze Estuary.

Six cross-sections were set (as shown in Figure 1) to draw the depth profile, and these were overlaid with identified elements, as shown in Figure 3. Cross-section 1 in the figure shows a longitudinal profile of large dunes (with a length of 19 m and height of 2 m) according to the classification of bedforms in Reference [39]. Cross-section 4 also shows the longitudinal profile of dunes on a similar scale. Cross-sections 2 and 5 show transverse profiles along the trough of dunes, respectively. Cross-section 3 shows a longitudinal profile of relatively flat bedforms (with a length of approximately 20 m and a height between 0.1 and 0.3 m), and Cross-section 6 shows a longitudinal profile of bedforms: it is basically flat and is considered to be a flat bed in this study.

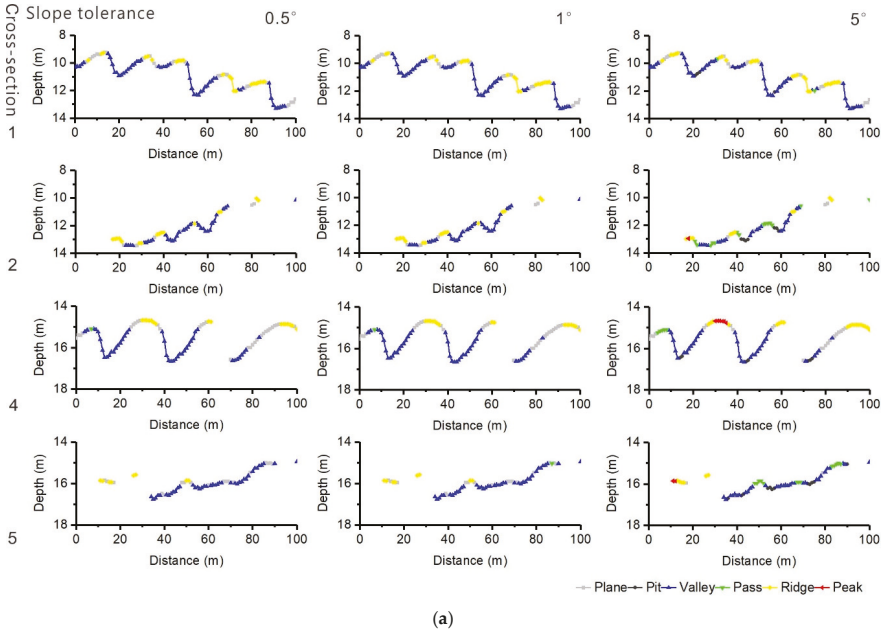

(**a**)

Figure 3. *Cont.*

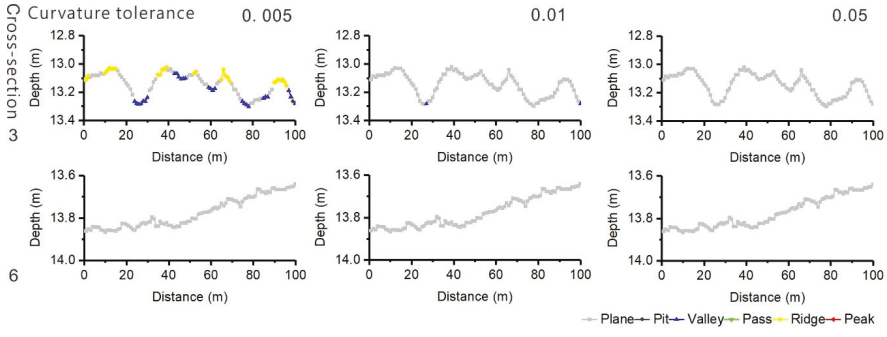

(**b**)

Figure 3. Water depth profiles overlaid by Wood's criteria-based elements for (**a**) Cross-sections 1, 2, 4, and 5 under various slope tolerances, and for (**b**) Cross-sections 3 and 6 under various curvature tolerances.

Trough and crest are the main features in dune areas [15–18]. Using Wood's criteria, the crest and trough were mainly represented by ridge and valley elements, as shown in Figure 3a. The widths of the ridges and valleys were determined by the curvature tolerance set: large values induced narrow ridges and valley, as shown in Figure 2. Many studies have ascertained that scour pits can be contained in the troughs of bedforms with varying elevations [15–18], and bedforms contain scour pits with diverse sizes. In the case of Wood's criteria, the size of the pit element was determined by the curvature and slope tolerance set, as indicated in Table 1. Large slope tolerance with smaller curvature caused larger areas to be defined as scour pits, as shown in Figure 3a, where the scale of pit element was enlarged in both the longitudinal and transverse profiles with a decrease in curvature tolerance. Many studies have identified flat bed as being a typical bedform [9–11]. With Wood's criteria, the element plane was used to indicate a relatively flat, smooth, inclined area, as shown in Figure 3b, and the value of the curvature tolerance determined the distribution of the plane elements. Using Wood's criteria, a curvature tolerance of 0.01 can be used to filter relatively flat bedforms using plane elements. As evident from Figure 3b, a relatively smaller curvature tolerance should be used to define plane elements on a flat bed.

3.2. SOM Technique-Based Geomorphic Elements Mapping for Describing Subaqueous Bedforms

The morphometric parameters calculated under a window size of 7×7 m when employing Wood's criteria were also combined into the input vector to train the SOM. When using the SOM technique, the number of output map units corresponds to the number of geomorphic elements, and the spatial arrangement form of the units can be one-, two-, or three-dimensional. Although the most reasonable number of map units is unknown, Yan et al. [36] found that two and three dimensions offer a more meaningful classification. As a result, arrangement forms including (3 2), (4 2), (2 2 2), (3 3), and (5 2) were considered for arranging the output map units (Figure 4). The mean slope and cross-section curvature for each map unit were calculated as coordinates to plot the units within the feature space. According to a previous study [20], the units should be concentrated in three lines that correspond to three main groups (channel, planar, and ridge) to ensure that the units are well-defined as geomorphic elements. The units can then be sub-defined by slope (such as flat, gentle slope, moderate slope, steep slope, and very steep slope).

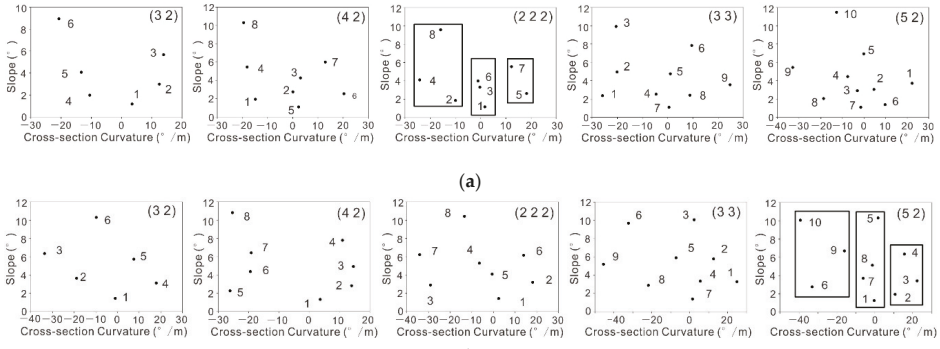

Figure 4. Distribution of map units in the feature space with different numbers and arrangement map units using the self-organization map (SOM) technique for the sample data of (**a**) Chizhou Reach and (**b**) the Yangtze Estuary.

For Chizhou Reach, the suitable number of output map units was found to be 8, and the units were arranged in the form of (2 2 2), as shown in Figure 4a. Table 2 lists the suitable definitions and areas associated with each map unit. Map units 3 and 6 were given the same definition (moderate slopes, planar) because they host relatively smaller areas and are situated very close within the feature space. For the Yangtze Estuary, (5 2) was selected as the suitable arrangement of map units (Figure 4b), and map units 7 and 8 were given the same definition (moderate slopes, planar).

Table 2. Statistical results for geomorphic elements under Wood's criteria, the SOM technique, and geomorphons.

Method	The Sample Data of Chizhou Reach			The Sample Data of Yangtze Estuary		
	(Map Unit) Element	Area (m^2)	Percentage (%)	(Map Unit) Element	Area (m^2)	Percentage (%)
Wood's criteria	Plane	36,586	32.05	Plane	35,455	29.54
	Pit	3668	3.21	Pit	4089	3.41
	Valley	30,124	26.39	Valley	29,972	24.97
	Pass	12,188	10.67	Pass	12,754	10.62
	Ridge	28,573	25.03	Ridge	33,267	27.71
	Peak	3029	2.65	Peak	4496	3.75
	Total	114,168	100.00	Total	120,033	100.00
SOM technique	(1) Flat, planar	28,645	25.09	(1) Flat, planar	21,239	17.69
	(2) Gentle slopes, channel	16,624	14.56	(2) Gentle slopes, ridge	13,209	11.00
	(3) Moderate slopes, planar	8960	7.85	(3) Moderate slopes, ridge	14,528	12.10
	(4) Moderate slopes, channel	12,308	10.78	(4) Steep slopes, ridge	9517	7.93
	(5) Gentle slopes, ridge	17,859	15.64	(5) Very steep slopes, planar	7255	6.04
	(6) Moderate slopes, planar	3232	2.83	(6) Gentle slopes, channel	12,141	10.11
	(7) Steep slopes, ridge	13,414	11.75	(7) Moderate slopes, planar	8927	7.44
	(8) Steep slopes, channel	13,126	11.50	(8) Moderate slopes, planar	11,827	9.85
				(9) Steep slopes, channel	11,310	9.42
				(10) Very steep slopes, channel	10,080	8.40
	Total	114,168	100.00	Total	120,033	100.00

Table 2. *Cont.*

Method	The Sample Data of Chizhou Reach			The Sample Data of Yangtze Estuary		
	(Map Unit) Element	Area (m^2)	Percentage (%)	(Map Unit) Element	Area (m^2)	Percentage (%)
Geomorphons	Ridge	16,184	12.35	Ridge	24,891	17.96
	Shoulder	17,360	13.25	Shoulder	15,918	11.48
	Spur	7361	5.62	Spur	11,827	8.53
	Slope	28,809	21.98	Slope	29,986	21.63
	Hollow	7238	5.52	Hollow	10,283	7.42
	Foot-slope	17,119	13.06	Foot-slope	7054	5.09
	Valley	11,779	8.99	Valley	13,816	9.97
	Pit	2029	1.55	Pit	2843	2.05
	Flat	21,858	16.68	Flat	20,679	14.92
	Peak	1304	1.00	Peak	1326	0.96
	Total	131,041	100.00	Total	138,623	100.00

The SOM technique not only divided the surface into channel and ridge but also further divided these two features based on their slopes, as shown in Figure 5. Gentle slope ridges are narrow and are located on the crest of dunes, and steep slope ridges are located on the lateral side of gentle slope ridges (Figure 6a). In addition, the gentle slope channel is narrow and located on the trough of dunes, whereas the steep slope channels are located on the lateral side of the gentle slope channel (Figure 6b). Therefore, gentle slope ridges and channels tend to be linear along crests and troughs. However, a pit element could not be identified using this technique, as shown in Figure 5 and Table 2. The SOM technique indicates relatively flat bedforms with flat, planar elements that correspond to the middle curvature and lowest slope while the middle curvature and relatively large slope are related to the relatively steep planar. However, it is difficult to precisely distinguish flat beds using this technique. Moreover, when the crest and trough are very wide, the lower slope planar can be generated in the crest and trough of bedforms.

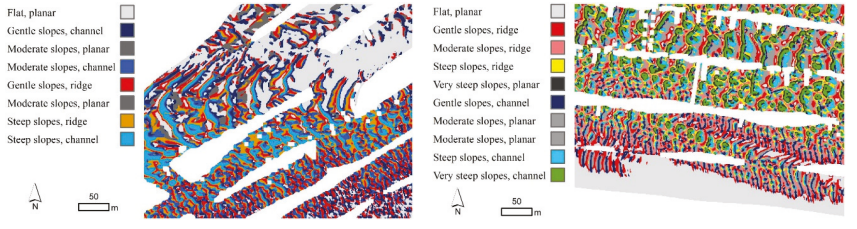

(**a**) (**b**)

Figure 5. SOM technique-based distribution of geomorphic elements for the sample data of (**a**) Chizhou Reach and (**b**) the Yangtze Estuary.

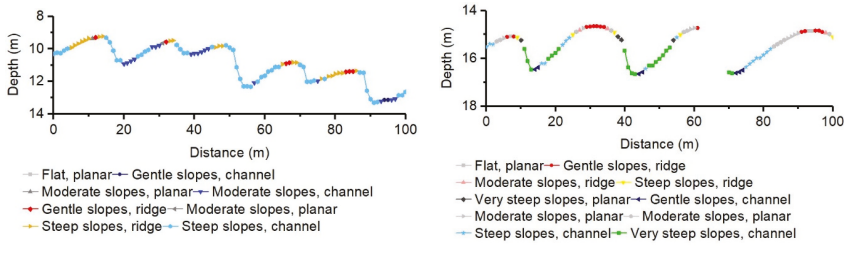

(**a**) (**b**)

Figure 6. Water depth profile overlaid by SOM technique-based elements for (**a**) Cross-section 1 and (**b**) Cross-section 4.

3.3. Geomorphons-Based Geomorphic Elements Mapping for Describing Subaqueous Bedforms

Geomorphons requires that the lookup distance has a relatively large size. Jasiewicz and Stepinski [21] suggested using 50 cells, as a larger distance provided no added benefits in their study. We also used a lookup distance containing 50 cells (equal to 50 m) in this study. The function of flatness is more important, and the slot is denoted by 0 for basically horizontal surface with the difference between the nadir and zenith angle smaller than flatness. When the area of flatness is large, a greater number of slots are denoted by 0, which means that a larger area is then defined as being a flat element, as shown in Figure 7. The figures show that the flat element area is too large when flatness is greater than 4°.

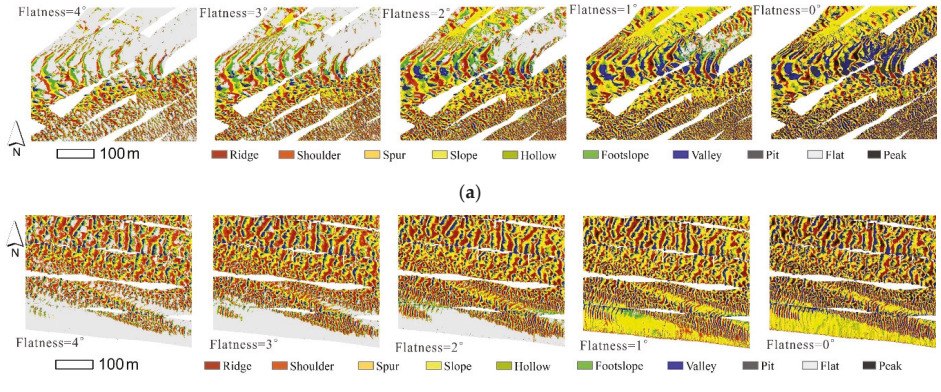

Figure 7. Geomorphons-based distribution of geomorphic elements with different flatness degrees for the sample data of (**a**) Chizhou Reach of the Yangtze River and (**b**) the Yangtze Estuary.

In the case of geomorphons, ridge and valley elements were also used to represent crest and trough bedforms: their scales were determined by flatness, and they increased in accordance with decrements in flatness (Figure 8). Similarly, the size of the pit element was determined by flatness, and smaller degrees of flatness created a greater surface with low roughness into a pit element within troughs of bedforms, as indicated in Figure 8, where the scale of the pit element is enlarged in both the longitudinal and transverse profiles and the decrements in flatness relate to those in cross-sections 1, 2, 4, and 5. Geomorphons use flat element to indicate relatively flat areas under suitable flatness degrees, and a flatness degree of 2° can be used to filter relatively flat bedforms using flat elements. Cross-section 6 in Figure 8 shows that when flatness was 0°, the flat bed could be redefined as a slope element without a ridge and a valley, and Cross-section 3 shows that relatively flat bedforms were redefined as slope elements coupled with a ridge and a valley (Figure 8). It thus seems feasible to use geomorphons to distinguish flat beds from relatively flat bedforms by combining geomorphons-based element maps when flatness is equal to zero and relatively smaller.

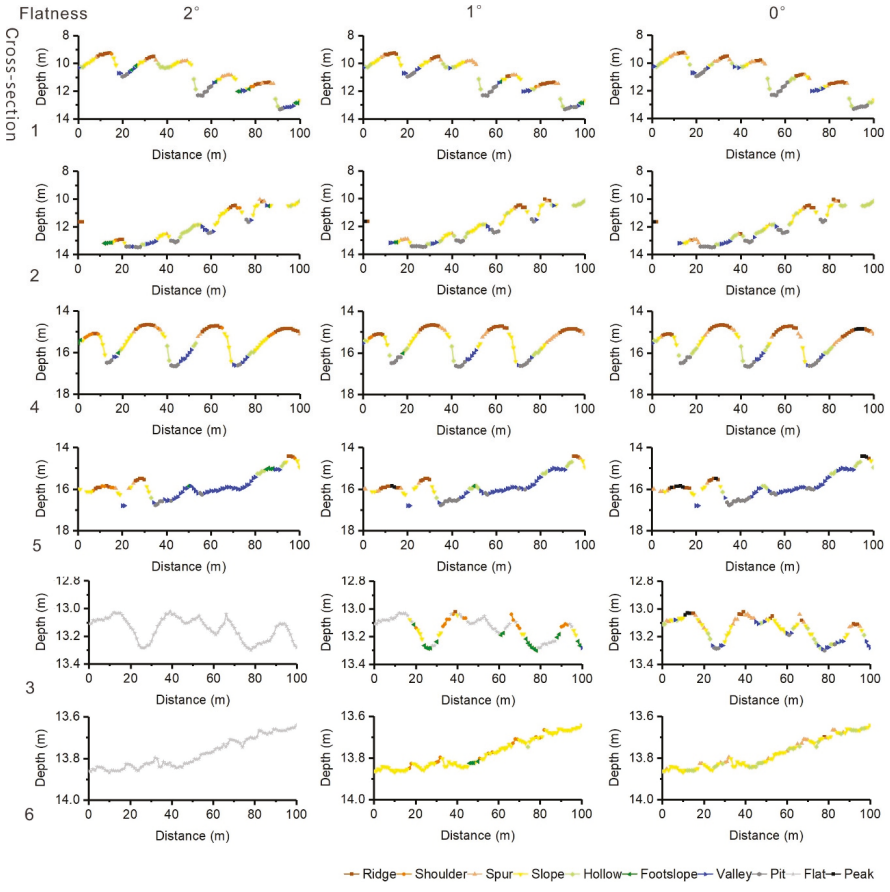

Figure 8. Water depth profile overlaid by geomorphons-based elements for Cross-sections 1–6 under various flatness degrees.

3.4. Comparison of the Three Methods

The number and combination of map units control the mapping result when using the SOM technique, while thresholds determine the results when using Wood's criteria and geomorphons. Table 2 lists the statistical results of elements for the three methods under suitable parameter settings. In this respect, a curvature tolerance of 0.01 and a slope tolerance of 5° is considered to be a suitable combination for separating relatively flat areas from subaqueous dunes areas when using the plane element in Wood's criteria. In this study, 2° was set as the optimal flatness to match flat elements with relatively flat areas. For Chizhou Reach, the total area of all the geomorphic elements defined by Wood's criteria and the SOM technique was 114,168 m^2, and an area of 16,873 m^2 provided a NODATA value or caused data loss. For the Yangtze Estuary, the total area was 120,033 m^2 and an area of 18,590 m^2 provided a NODATA value or caused data loss (Table 2). These morphometric parameters were calculated in a window of 7 × 7 m. A geomorphic element was defined as NODATA when the window contained a NODATA value (a cell of blank area). In contrast, geomorphons provided a superior result, and the area between output and input was equal.

For the description of flat bed, Wood's criteria uses the plane element to indicate relatively flat areas, and curvature tolerance determines the distribution of the plane element, which can host a

relatively larger slope angle. The SOM technique indicates a relatively flat area with flat, planar element corresponding to middle curvature and lowest slope. Middle curvature and relatively large slope relate to relatively steep, planar areas. Geomorphons uses flat elements to indicate relatively flat areas, and the definition of flat is related to a basically horizontal surface. As a result, the percentage of flat elements (in geomorphons) is the lowest, while that of plane (in Wood's criteria) is the largest (Table 2). For the description of scour pit, the size of the pit element is determined by the set of curvature and slope tolerance in Wood's criteria, and by the assignment of the flatness value in geomorphons; however, it cannot be defined using the SOM technique. To describe trough and crest, the SOM technique not only divides surface into channel and ridge but also further divides them based on their slope. Gentle-sloping ridge and channel tend to be the linear crest and trough of bedforms. For Wood's criteria and geomorphons, the crest and trough are present in an areal form, and their sizes change in accordance with slope tolerance and flatness. In comparison to the SOM technique, Wood's criteria and geomorphons provide a relatively simple element map matching with bedforms' features.

4. Discussion

4.1. Comparison with Terrestrial Landform Element Mapping

These three methods have different critical values for subaqueous bedforms in river systems and terrestrial landforms. Using Wood's criteria, the DEM (Digital Elevation Model) size employed in a geomorphologically diverse region of Central Mexico was 90 × 90 m, and the suitable tolerances of slope and curvature were set as 6° and 0.0001, respectively [40]. In addition, a 90 × 90 m DEM was used for morphologic element mapping and 1° and 0.0005 were employed as the suitable tolerances of slope and curvature respectively, at the border of Poland, Slovakia, and Ukraine [20]. Furthermore, a DEM of 50 × 50 m was utilized for landform delineation in South Tyrol with slope and curvature set as 14° and 0.002, respectively [41]. In this article, these critical values were set as 5° and 0.01 when data in the resolution of 1 × 1 m were obtained via measurements in two areas of the Yangtze River. Although the slope tolerance is similar to that of other studies, the curvature tolerance is considerably larger than that used for terrestrial landforms. For geomorphons, the reported flatness in the literature varies with the area of focus; however, it essentially ranges from 0° to 3° [21,42–45], which is close to the 2° used in this study.

For the SOM technique, the optimal classification was obtained when a suitable number and combination of map units were set. The optimal number of map units changed with the four input morphometric parameters, which was also mentioned in a previous study [36]. All studies have analyzed different terrain, which means that a variety of vectors have been input to the SOM. In a previous study, a suitable number of 10 map units was determined at the boundary between Poland, Slovakia, and the Ukraine [20], and 8 was suggested for use in a loess area [36]. In this research, 8 and 10 map units were used for the two samples, respectively. It thus appears that the common number of map units used is 8 or 10, although the optimal number of map units changes.

A digital terrain model obtained via remote sensing basically contains no missing data for entire regions. However, bathymetric data always contain blank areas in a general situation. The SOM technique and Wood's criteria do not operate effectively in the presence of blank data, because their use is based on the calculation of slope, cross-sectional curvature, maximum curvature, and minimum curvature.

4.2. Limitations and Prospects

Figure 9 presents a strategy for using geomorphic elements to characterize river bedform features. In this respect, the crest, trough, flat bed, and scour pit are considered. Many of the geomorphic elements shown in Figure 9 are indicative of special geographic units in other subaqueous environments; for example, peak and pit can be used to map seafloor hills and depressions [25]. Further studies are required to determine the indicative functions of the geomorphic elements for subaqueous objects;

for example, for erosional holes, erosional flutes, sand mining holes, and sinking boats, which relate to the anthropogenic drivers of subaqueous topographical changes [18], and for bank scarps, toes, and failure, which relate to bank slope stability.

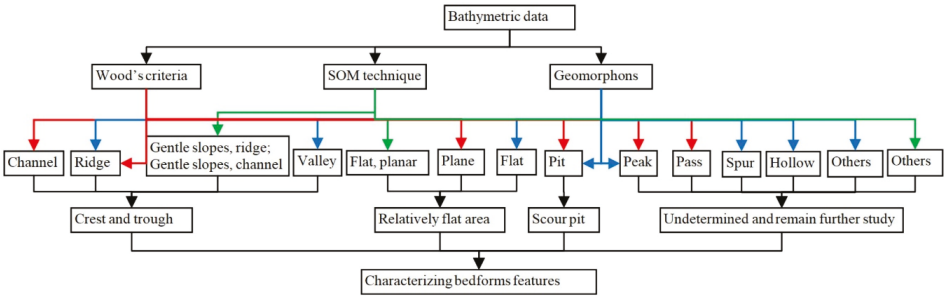

Figure 9. Strategy for describing subaqueous bedforms features using geomorphic elements in a river system.

The spatial scales of ripples in a bedform generally have lengths in the order of 0.05–0.50 m [46] and cannot be detected when using a cell size of 1 m. The bathymetric data used in this study were at a resolution of 1 × 1 m, which means that the ripples between subaqueous dunes and the flat bed were inevitably ignored. Geomorphic elements mapping using higher resolution bathymetric data are required in further studies to ameliorate this limitation. In addition, dunes often show superimposed relationships under various bedform scales [3,47], because of the effect of complex flow dynamics on different temporal and spatial scales. The bathymetric data cell size may thus need to be adjusted to identify superimposed regions on different scales.

Height, length, and direction of bedforms are important parameters relating to the dynamic features of flow [2]. Although the geomorphic elements map is not suitable for use in calculating these parameters, it provides the potential to narrow the analysis range by separating the dunes area from the relatively flat bedforms. Previous studies have inferred that subaqueous geomorphic elements have statistical relationships with the category of landforms [40,42]. Some studies have found that the spatial distribution of geomorphic elements presents a certain pattern that represents the type of landform [48,49]. As in the relationship between landform elements and landscape, all of the geomorphic elements listed in Figure 9 are meaningful for comprehensively depicting the pattern of elements and regionalizing the bedform areas; however, the development of a more detailed method remains the subject of further research. In addition, the generation of a geomorphic elements map has the great potential to be used in auto-tracking the movement of bedforms, which is significant for assessing bedform instability [50,51].

5. Conclusions

This study analyzed the use of geomorphic element mapping methods for depicting subaqueous bedforms in the Yangtze River. The main conclusions are presented as follows.

The plane element in Wood's criteria, the flat, planar element in the SOM technique, and the flat element in geomorphons can be used to indicate the existence of relatively flat bedforms. A curvature tolerance of 0.01 in Wood's criteria, and flatness of 2° in geomorphons, are considered to be optimal thresholds for automatically filtering relatively flat bedforms from subaqueous dunes. In addition, for the description of scour pit, the value of slope tolerance and flatness can be used to adjust the size of a pit element, which increases with a decrease in the threshold, while the SOM technique cannot extract pit. We recommend geomorphons as the optimal method for characterizing bedforms' features, because it provides a simple element map without any loss of area.

Slope tolerance and flatness are close to the landform element classification, while curvature tolerance is far larger. The optimal number and combination of map units appears to change for different areas but is generally 8 or 10, irrespective of the bedform or landform analyzed. Therefore, with the SOM, 8 and 10 map units should be recommended in future studies.

Using the three methods, many other elements (such as spur, hollow, peak, and pass) can be extracted to reflect the detailed roughness of bedforms or other subaqueous objects (bank scarp, erosional hole, and sinking boat), and this remains the subject of future studies. The spatial distribution of geomorphic elements presents a certain pattern of elements that represents the type of bedform, and it can be used to narrow the range of morphology and dynamic analysis of bedforms.

Author Contributions: Conceptualization, G.Y. (Ge Yan) and H.C.; methodology, G.Y. (Ge Yan); validation, G.Y. (Ge Yan), H.C. and L.T.; formal analysis, G.Y. (Ge Yan); investigation, G.Y. (Ge Yan); resources, H.C., Y.J., G.Y. (Guoqiang Yang) and Q.Z.; data curation, L.T. and W.X.; writing—original draft preparation, G.Y. (Ge Yan); writing—review and editing, H.C.; supervision, H.C.; project administration, H.C. and Y.J. All authors have read and agreed to the published version of the manuscript.

Funding: This research was funded by the China Geological Survey, grant number DD20190260, NSFC-NWO-EPSRC, grant number 51761135023, and the Natural Science Foundation of China, grant number 41476075.

Acknowledgments: We acknowledge Shuwei Zheng, Jiahao Zhang, and Kai Hua for their assistance with conducting field survey work.

Conflicts of Interest: The authors declare no conflict of interest.

References

1. Engelund, F.; Fredsoe, J. Sediment ripples and dunes. *Annu. Rev. Fluid Mech.* **1982**, *14*, 13–37.
2. Garlan, T. GIS and mapping of moving marine sand dunes. In Proceedings of the 24th International Cartography Conference (ICC 2009), Santiago, Chile, 15–21 November 2009.
3. Gutierrez, R.R.; Abad, J.D.; Parsons, D.R.; Best, J.L. Discrimination of bed form scales using robust spline filters and wavelet transforms: Methods and application to synthetic signals and bed forms of the Río Paraná, Argentina. *J. Geophys. Res. Earth Surf.* **2013**, *118*, 1400–1418.
4. Knaapen, M.A.F. Sandwave migration predictor based on shape information. *J. Geophys. Res. Earth Surf.* **2005**, *110*, F04S11.
5. Van der Mark, C.F.; Blom, A. *A New and Widely Applicable Tool for Determining the Geometric Properties of Bedforms (No. 2007R-003/WEM-002 ISSN 1568-4652)*; University of Twente: Enschede, The Netherlands, 2007.
6. Duffy, G. Patterns of morphometric parameters in a large bedform field: Development and application of a tool for automated bedform morphometry. *Ir. J. Earth Sci.* **2012**, *30*, 31–39.
7. Van Dijk, T.A.G.P.; Lindenbergh, R.C.; Egberts, P.J.P. Separating bathymetric data representing multiscale rhythmic bed forms: A geostatistical and spectral method compared. *J. Geophys. Res. Earth Surf.* **2008**, *113*, F04017.
8. Debese, N.; Jacq, J.J.; Garlan, T. Extraction of sandy bedforms features through geodesic morphometry. *Geomorphology* **2016**, *268*, 82–97.
9. Simons, D.B.; Richardson, E.V.; Albertson, M.L. Flume studies using medium sand (0.45 mm). In *Professional Papers of the United States Geological Survey*; United States Geological Survey: Reston, VA, USA, 1961; Volume 1498-A, pp. 1–76.
10. Simons, D.B.; Richardson, E.V. Resistance to flow in alluvial channels. In *Professional Papers of the United States Geological Survey*; United States Geological Survey: Reston, VA, USA, 1966; Volume 422-J, pp. 1–61.
11. Guy, H.P.; Simons, D.B.; Richardson, E.V. Summary of alluvial channel data from flume experiments, 1956–1961. In *Professional Papers of the United States Geological Survey*; United States Geological Survey: Reston, VA, USA, 1966; Volume 462-I, pp. 1–96.
12. White, S.J. Plane bed thresholds of fine grained sediments. *Nature* **1970**, *228*, 152–153.
13. Bennett, S.; Best, J.; Nnadi, F.N.; Wilson, K.C. Bed-load motion at high shear stress: Dune washout and plane-bed flow. *J. Hydraul. Eng. ASCE* **1997**, *123*, 375–377.
14. Camenen, B.; Larson, M.; Bayram, A. Equivalent roughness height for plane bed under oscillatory flow. *Estuar. Coast. Shelf Sci.* **2009**, *81*, 409–422.

15. Rubin, D.M. A unifying model for planform straightness of ripples and dunes in air and water. *Earth Sci. Rev.* **2012**, *113*, 176–185.
16. Zheng, S.; Cheng, H.; Wu, S.; Liu, G.; Lu, X.; Xu, W. Discovery and implications of catenary-bead subaqueous dunes. *Sci. China Earth Sci.* **2016**, *59*, 495–502.
17. Zheng, S.; Cheng, H.; Wu, S.; Shi, S.; Xu, W.; Zhou, Q.; Jiang, Y. Morphology and mechanism of the very large dunes in the tidal reach of the Yangtze River, China. *Cont. Shelf Res.* **2017**, *139*, 54–61.
18. Zheng, S.; Cheng, H.; Shi, S.; Xu, W.; Zhou, Q.; Jiang, Y.; Zhou, F.; Cao, M. Impact of anthropogenic drivers on subaqueous topographical change in the Datong to Xuliujing reach of the Yangtze River. *Sci. China Earth Sci.* **2018**, *61*, 940–950.
19. Wood, J. The Geomorphological Characterization of Digital Elevation Models. Ph.D. Thesis, University of Leicester, Leicester, UK, 1996.
20. Ehsani, A.H.; Quiel, F. Geomorphometric feature analysis using morphometric parameterization and artificial neural networks. *Geomorphology* **2008**, *99*, 1–12.
21. Jasiewicz, J.; Stepinski, T.F. Geomorphons—A pattern recognition approach to classification and mapping of landforms. *Geomorphology* **2013**, *182*, 147–156.
22. Schmidt, J.; Hewitt, A. Fuzzy land element classification from DTMs based on geometry and terrain position. *Geoderma* **2004**, *121*, 243–256.
23. Drăguţ, L.; Blaschke, T. Automated classification of landform elements using object-based image analysis. *Geomorphology* **2006**, *81*, 330–344.
24. Stefano, M.D.; Mayer, L.A. An automatic procedure for the quantitative characterization of submarine bedforms. *Geosciences* **2018**, *8*, 28.
25. Cui, X.; Xing, Z.; Yang, F.; Fan, M.; Ma, Y.; Sun, Y. A method for multibeam seafloor terrain classification based on self-adaptive geographic classification unit. *Appl. Acoust.* **2020**, *157*, 107029.
26. Shi, S.; Cheng, H.; Xuan, X.; Hu, F.; Yuan, X.; Jiang, Y.; Zhou, Q. Fluctuations in the tidal limit of the Yangtze River estuary in the last decade. *Sci. China-Earth Sci.* **2018**, *61*, 1136–1147.
27. Shi, S.; Cheng, H.; Zheng, S.; Xu, W.; Lu, X.; Jiang, Y.; Zhou, Q. Erosional topography of the tidal limit in the Yangtze River in flood seasons after the river closure at Three Gorges. *Haiyang Xuebao* **2017**, *39*, 85–95.
28. Cheng, H.Q.; Chen, J.Y. Adapting cities to sea level rise: A perspective from Chinese deltas. *Adv. Clim. Chang. Res.* **2017**, *8*, 130–136.
29. Cheng, H.Q.; Chen, J.Y.; Chen, Z.J.; Ruan, R.L.; Xu, G.Q.; Zeng, G.; Zhu, J.R.; Dai, Z.J.; Chen, X.Y.; Gu, S.H.; et al. Mapping sea level rise behavior in an estuarine delta system: A case study along the Shanghai coast. *Engineering* **2018**, *4*, 156–163.
30. Hua, K.; Cheng, H.; Zheng, S. Formation mechanism of near-shore erosional topography in the Hengsha passage of the Yangtze Estuary. *Acta Geogr. Sin.* **2019**, *74*, 1363–1373.
31. Xu, W.; Cheng, H.; Zheng, S.; Wang, S.; Chen, G.; Yuan, X. Evolution of Nanjing Channel in the Yangtze River and its response to human activities during the last 20 years. *Sci. Geogr. Sin.* **2019**, *39*, 663–670.
32. Evans, I.S. General geomorphology, derivatives of altitude and descriptive statistics. In *Spatial Analysis in Geomorphology*; Chorley, R.J., Ed.; Methuen & Co. Ltd.: London, UK, 1972; pp. 17–90.
33. Kohonen, T. *Self Organizing Maps*, 3rd ed.; Springer: New York, NY, USA, 2001.
34. Vesanto, J.; Alhoniemi, E. Clustering of the self-organizing map. Neural Networks. *IEEE Trans. Neural Netw.* **2000**, *11*, 586–600.
35. Bação, F.; Lobo, V.; Painho, M. The self-organizing map, the Geo-SOM, and relevant variants for geosciences. *Comput. Geosci.* **2005**, *31*, 155–163.
36. Yan, G.; Liang, S.; Ke, Y.; Liu, S.; Zhao, H.; Yang, Z. Optimizing classification of landform element using feature space: A case study in a loess area. *Electron. J. Geotech. Eng.* **2016**, *21*, 5814–5824.
37. Liao, W.H. Region description using extended local ternary patterns. In Proceedings of the 2010 20th International Conference on Pattern Recognition, Istanbul, Turkey, 23–26 August 2010; pp. 1003–1006.
38. Yokoyama, R.; Shlrasawa, M.; Pike, R.J. Visualizing topography by openness: A new application of image processing to digital elevation models. *Photogramm. Eng. Remote Sens.* **2002**, *68*, 257–265.
39. Ashley, G.M. Classification of large-scale subaqueous bedforms: A new look at an old problem. *J. Sediment. Petrol.* **1990**, *60*, 160–172.
40. Bolongaro-Crevenna, A.; Torres-Rodríguez, V.; Sorani, V.; Frame, D.; Ortiz, M.A. Geomorphometric analysis for characterizing landforms in Morelos State, Mexico. *Geomorphology* **2005**, *67*, 407–422.

41. Gruber, F.E.; Baruck, J.; Geitner, C. Algorithms vs. surveyors: A comparison of automated landform delineations and surveyed topographic positions from soil mapping in an Alpine environment. *Geoderma* **2017**, *308*, 9–25.
42. Jasiewicz, J.; Netzel, P.; Stepinski, T.F. Landscape similarity, retrieval, and machine mapping of physiographic units. *Geomorphology* **2014**, *221*, 104–112.
43. Pinto, L.C.; Mello, C.R.; Norton, L.D.; Owens, P.R.; Curi, N. Spatial prediction of soil -water transmissivity based on fuzzy logic in a Brazilian headwater watershed. *Catena* **2016**, *143*, 26–34.
44. Kramm, T.; Hoffmeister, D.; Curdt, C.; Maleki, S.; Khormali, F.; Kehl, M. Accuracy assessment of landform classification approaches on different spatial scales for the Iranian Loess Plateau. *ISPRS Int. Geo-Inf.* **2017**, *6*, 366.
45. Luo, W.; Liu, C.C. Innovative landslide susceptibility mapping supported by geomorphon and geographical detector methods. *Landslides* **2018**, *15*, 465–474.
46. Gallagher, E.L.; Elgar, S.; Guza, R.T.; Thornton, E.B. Estimating nearshore bedform amplitudes with altimeters. *Mar. Geol.* **2005**, *216*, 51–57.
47. Barnard, P.L.; Erikson, L.H.; Kvitek, R.G. Small-scale sediment transport patterns and bedform morphodynamics: New insights from high-resolution multibeam bathymetry. *Geo-Mar. Lett.* **2011**, *31*, 227–236.
48. MacMillan, R.A.; Jones, R.K.; McNabb, D.H. Defining a hierarchy of spatial entities for environmental analysis and modeling using digital elevation models (DEMs). *Comput. Environ. Urban. Syst.* **2004**, *28*, 175–200.
49. Minár, J.; Evans, I.S. Elementary forms for land surface segmentation: The theoretical basis of terrain analysis and geomorphological mapping. *Geomorphology* **2008**, *95*, 236–259.
50. Cheng, H.-Q.; Kostaschuk, R.; Shi, Z. Tidal currents, bed sediments, and bedforms at the South Branch and the South Channel of the Changjiang (Yangtze) estuary, China: Implications for the ripple-dune transition. *Estuaries* **2004**, *27*, 861–866.
51. Cheng, H.; Li, J.; Yin, D.; Li, M.; Wang, B. Nearshore bedform instability in the eastern entrance to the Qiongzhou Strait, South China Sea. *Front. Earth Sci. China* **2008**, *2*, 283–291.

applied sciences

MDPI

Article

Modeling Short-Term Landscape Modification and Sedimentary Budget Induced by Dam Removal: Insights from LEM Application

Dario Gioia [1,*] and Marcello Schiattarella [2]

[1] Istituto di Scienze del Patrimonio Culturale (ISPC), Consiglio Nazionale delle Ricerche, Tito Scalo, I-85050 Potenza, Italy

[2] Dipartimento delle Culture Europee e del Mediterraneo (DiCEM), Università degli Studi della Basilicata, I-75100 Matera, Italy; marcello.schiattarella@unibas.it

* Correspondence: dario.gioia@cnr.it; Tel.: +39-0971-427309

Received: 3 October 2020; Accepted: 27 October 2020; Published: 30 October 2020

Abstract: Simulation scenarios of sediment flux variation and topographic changes due to dam removal have been investigated in a reservoir catchment of the axial zone of southern Italy through the application of a landscape evolution model (i.e.,: the Caesar–Lisflood landscape evolution models, LEM). LEM simulation highlights that the abrupt change in base level due to dam removal induces a significant increase in erosion ability of main channels and a strong incision of the reservoir infill. Analysis of the sediment dynamics resulting from the dam removal highlights a significant increase of the total eroded volumes in the post dam scenario of a factor higher than 4. Model results also predict a strong modification of the longitudinal profile of main channels, which promoted fluvial incision upstream and downstream of the former reservoir area. Such a geomorphic response is in agreement with previous analysis of the fluvial system short-term response induced by base-level lowering, thus demonstrating the reliability of LEM-based analysis for solving open problems in applied geomorphology such as perturbations and short-term landscape modification natural processes or human impact.

Keywords: landscape evolution; soil erosion; DEM analysis; applied geomorphology; dam removal; base-level lowering; southern Italy

1. Introduction

Base-level variation has a significant impact on a geomorphological system with severe changes in channel incision rate, sediment flux, and spatial distribution of geomorphological processes [1–3]. A fast transition from endorheic (i.e.: centripetal drainage or closed basin) to exorheic drainage is one of the most relevant cases of disequilibrium of a landscape, because it promotes a non-linear response of the fluvial systems and a complex spatial and temporal response of river incision and sediment flux (see for example [4]). Several works have investigated the long-term response of the drainage network to a transition from endorheic to exorheic conditions due to complex climate- or tectonic-driven processes such as sediment overfilling, headward stream erosion, and threshold incision or fluvial capture [5–8]. This kind of analysis is largely based on morphotectonic studies and related qualitative reconstruction of past stages of landscape evolution [9–11]. Dam construction and/or removal is one of the human-induced perturbations of the fluvial net with a stronger impact on the geomorphic system [12–14]. Many works have been focused on the analysis of the effects of this kind of disturbance on the fluvial network and sediment flux, highlighting a typical response that is strongly controlled by the post-dam river longitudinal profile. In fact, upstream knickpoint retreat generally promoted incision of both upland areas and reservoir infill, but several works have

demonstrated that local factors such as rates of knickpoint migration [15,16], bedrock erodibility [17,18], grain-size and texture of reservoir sediment [19] and width of the reservoir [17,19] can drive a complex response of river processes and promote a high spatial and temporal variability of erosion and deposition. Most of these studies are based on field and remote sensing data at limited spatial and temporal scales [17,19,20] or on the application of 1-D models [21,22]. For example, extensive geomorphic analyses of dam removal scenarios have been conducted in the USA through: (i) the direct measurements of the post-dam modification of morpho-sedimentary features supported by one-dimensional hydrodynamic modeling [17]; or (ii) the application of channel evolution models such as CONCEPTS and DREAM [21,22]. Such models have a significant limitation that they are not able to fully capture the spatial (i.e., lateral) distribution of river processes, channel modification, and sediment flux.

In the last years, landscape evolution models (LEMs) have been extensively used to simulate short- and long-term geomorphic scenarios of sediment flux and topographic modification in different natural environments [23–27]. These studies have demonstrated that LEMs represent a powerful tool to predict morpho-sedimentary adjustments related to changes in land use, climate setting, and base levels [24,28–31]. Recently, the Caesar–Lisflood LEM was used to investigate the short-term (i.e., at a decadal scale) pattern and rates of geomorphic changes and associated sediment flux induced by removal of multiple dams in the middle reach of Kaja River, Austria [32]. The authors demonstrated the usefulness of the LEM to predict the 2-D geomorphological and sedimentary effect of the abrupt base-level fall related to dam removal. This kind of investigation overcomes the clear limitation of 1-D or empirical models and can provide a significant opportunity to modify different controlling factors such as climate setting, land use, vegetation growth, and sediment features. The main limitation of the application of such models is that a reliable calibration of a LEM is really complicated and several well-known reasons such as the difficulty of both the selection of model parameters and the absence of extensive validation of the prediction ability of the model results in natural environments could represent a significant limitation in its application in complex natural landscapes [25,33]. Thus, a test area where a LEM is already calibrated can provide a reliable opportunity to simulate the impact of dam removal on the morpho-sedimentary processes and rates. In this paper, we exploited this opportunity and investigated the geomorphic changes induced by dam removal in a small artificial reservoir of southern Italy (Figure 1), where the prediction ability of the Caesar–Lisflood LEM has been already tested [34]. More specifically, the calibration of the model has been recently carried out through the comparison between the simulation results and a direct estimation of sedimentation rates in the reservoir, demonstrating a good prediction ability of the model [34]. Application of the dam removal scenario in the catchment allowed us to investigate the short-term (i.e., at a decadal scale) response of the geomorphic system to the abrupt change in base level as well as the role of several local factors (i.e., infill thickness and geometry, the sediment and bedrock features) on the changes in sediment flux and channel pattern.

2. Study Area

The study area is located in an upland area of the Ofanto basin, a Pliocene-Quaternary tectonic depression of the southern Apennines, Italy (Figure 1). It includes the catchment of the Ficocchia Torrente stream, a dextral tributary of low hierarchical order of the Ofanto River. The Ficocchia stream is dammed in its lower reach by an earth dam (i.e., the Saetta dam), which was constructed by EIPLI (Agency for the Development of the Irrigation and Agricultural Transformation, Ministry of Agricultural, Food and Forestry Policies) between 1988 and 1989.

The Ofanto River cuts a large E-W-trending intermontane tectonic depression, Pliocene to Quaternary in age. The infill of the basin is intensively deformed by Pliocene-Pleistocene folding and faulting related to the younger stages of evolution of the southern Apennines chain [35] and covers a wide (i.e., about 350 kmq) and elongated area along the Ofanto River valley [36,37]. Pliocene-Pleistocene deposits of the Ofanto basin are composed of clay, sandstones and conglomerates, which unconformably

overlay poly-deformed units of limestone, shale and sandstone that belong to the Irpinian and Lagonegro tectonic units of Cretaceous to Miocene ages [36].

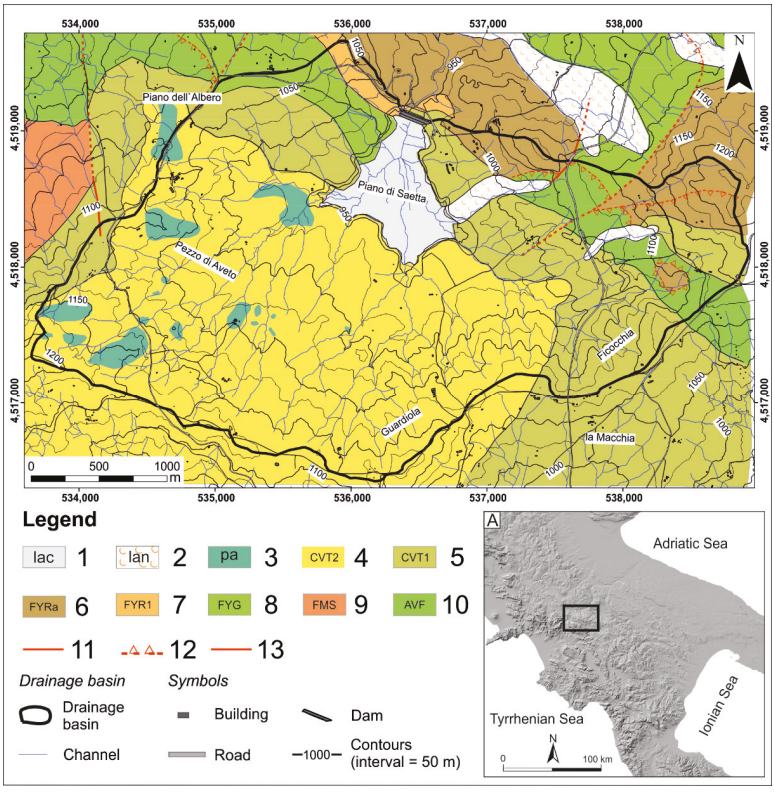

Figure 1. Geological map of the study area (modified from [36]). Legend: (**1**) Clay of lacustrine environment (lac, Holocene) (**2**) Landslide deposits (lan, Holocene) (**3**) Holistolits made by decametric blocks of limestone (pa, Upper Miocene); (**4**) Silt and marly clay (CVT2, Upper Miocene); (**5**) Coarse- to medium-grained sandstone with rare intercalation of lens of polygenic conglomerate (CVT1, Upper Miocene); (**6**) Calcareous breccia and grey shale (FYRa, Lower Cretaceous-Oligocene); (**7**) Alternance of chert, marly clay, calcarenites and calcareous breccia (FYR1, Lower Cretaceous-Oligocene); (**8**) Light-grey and greenish shale with intercalation of marls and limestone (FYG, Lower Cretaceous); (**9**) Alternance of calcarenite, calcilutite and varicoloured clay (FMS, Upper Cretaceous-Eocene); (**10**) Varicoloured clay (AVF, Lower Cretaceous); (**11**) High-angle fault (dashed if uncertain); (**12**) Thrust (dashed if uncertain); (**13**) Stratigraphic contact. (**A**) Geographical location of the study area.

The reservoir catchment is carved in a Cretaceous to Miocene bedrock made by tectonic domains belonging to Lagonegro units, Sicilide calcareous-clay succession and flysch deposits of Miocene syntectonic basins (Figure 1, see also [36]). The study area also features widespread outcroppings of upper Miocene deposits belonging to Castelvetere Formation. These deposits are composed of light brown sandstone with intercalation of conglomerate (CVT1, Figure 1) passing upward to silt and marly clay (CVT2, Figure 1) containing large blocks of olistoliths (pa, Figure 1). These deposits mainly crop out in the south-western sector of the study area and unconformably overlies the Lagonegro tectonic units, which form an elongated belt in the north-eastern sectors of the study area. The outcropping deposits of the Lagonegro units are mainly constituted by lower–middle Cretaceous marls and grey shales with calcarenites and calcirudites and calcareous breccia (Flysch Rosso Formation, FYRa and

FYR1 in Figure 1). Lower Cretaceous varicoloured clay (AVF) with thin intercalations of calcirudites and calcarenites (FMS) crops out in the northern sector of the studied area (Figure 1).

Heterogeneous landslide deposits and fine-grained reservoir sediments are the youngest lithological units of the study area.

The geomorphological pattern of the study area is strongly influenced by the Pliocene-Quaternary tectonic evolution and relief growth of this sector of the chain, which have also controlled the lithological features and spatial distribution of deposits. The landscape is located at an altitude ranging from 942 to 1242 m a.s.l. and is dominated by E–W trending ridges and thrust sheets, which are mainly carved in Cretaceous-to-Miocene pelagic deposits. These structural landforms are deeply cut by the drainage network of the Ficocchia stream (Figure 2).

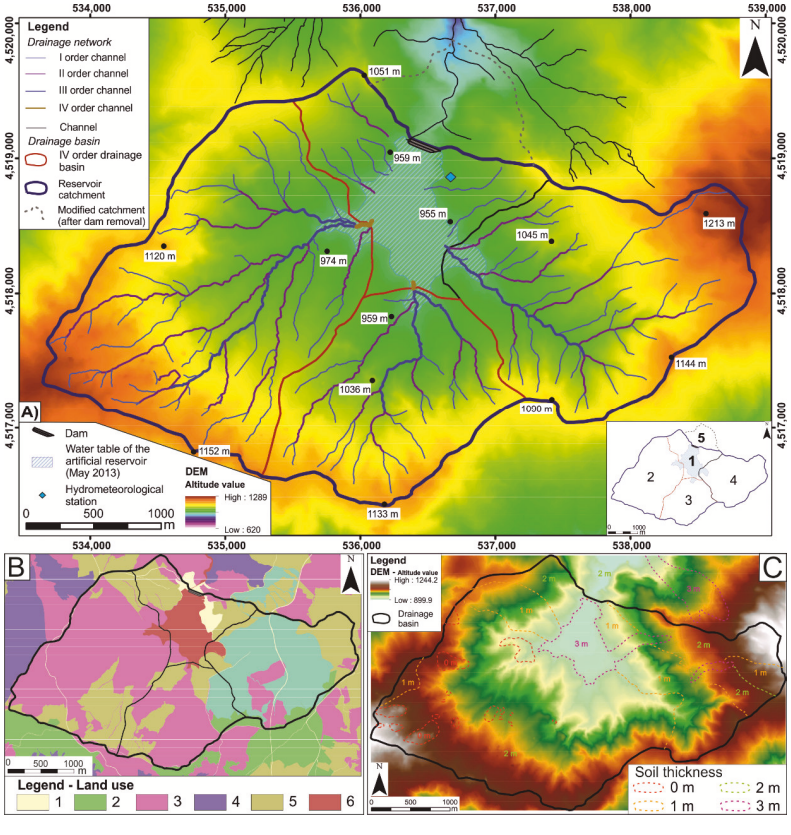

Figure 2. (**A**) DEM of the pre-dam removal landscape and drainage network of the study area. Hierarchization follows the Strahler's scheme. Numbering of the catchments is shown in the frame to the left. (**B**) Land-use map. Legend: (**1**) Anthropic surfaces and roads; (**2**) Arable lands; (**3**) Sclerophyllous vegetation; (**4**) Broad-leaved and mixed forests; (**5**) Natural grasslands; (**6**) Water courses and water bodies. (**C**) Isopachs of soil thickness derived by a GIS-based interpolation of the results of a field-survey analysis. Modified after [34].

The drainage basin of the artificial reservoir is formed by three small catchments of low hierarchical order showing a well-organized drainage network with a sub-dendritic pattern. The watershed of the southern sector of the reservoir catchment is featured by a sub-circular shape and runs on low-relief erosional land-surfaces [34,37]. In this sector, headwater channels exhibit a higher gradient than the

channels located in lower reaches (Figure 2). The main geomorphological processes of the study area are channel incision and fluvial erosion, which also represent the main influence factor of the sediment yield and flux. Slope processes and landsliding phenomena related to minor shallow mass movement processes and small earth-flows are located in the eastern sector of the studied catchment, where clay-rich deposits crop out.

Regional climate data of the study area was derived from the statistical analysis of a weather station located about 20 km to the west of the study area (daily rainfall record of the Pescopagano weather station, period: 1951–2015, [38]). Mean annual rainfall of the study area in the last half-century is slightly higher than 1000 mm year^{-1}. The climate setting is featured by dry summers and cold winters with a maximum of rainfall in autumn. In the last decades, a general trend of decrease in total annual rainfall was observed. This trend is associated with a decrease in rainy days and an increase of multi-day extreme rainfall events, mainly in autumn and spring. Shorter-term rainfall record (period: 1994–2016) of the hydro-meteorological station of the study area highlights a similar climate trend: mean annual precipitation is about 900 mm and rainfall peaks are mainly observed in the autumn and winter seasons, with rainfall maxima of 150–160 mm [34].

According to the classification of the III level of the Corine Land Cover project [39], a land-use map of the catchment was prepared from a revision of literature data and original investigation based on photointerpretation of aerial and satellite images. The landscape is dominated by semi-natural areas with natural grasslands and sclerophyllous vegetation that cover about 85% of the total area. Other sectors of the study area are classified as agricultural and urban areas.

3. Materials and Methods

3.1. Caesar–Lisflood LEM: Model Description and Calibration

Caesar–Lisflood is a second-generation LEM that can be used to model short- and long-term topographic changes and sediment flux of complex natural landscapes. In the last decade, the model was extensively used for the analysis at different temporal and spatial scales of issues of applied geomorphology and hydrology. As a matter of fact, there are at least 60 published papers dealing with model applications [40]. A rigorous and complete description is beyond the scope of this paper and is reported in [41].

The Caesar–Lisflood LEM uses a hydrological model to generate spatially distributed runoff, which is generated on a DEM to estimate flow depths and velocities [41]. Such data are used to model topographic changes and to assess topographic modification (i.e., erosion and deposition) within an active layer with a pre-defined grain-size of deposits. The modified DEM becomes the starting point for the next time step of the simulation. The user can select a catchment mode with no internal influxes other than rainfall or a reach mode, where the flow enters through the main river. Input data of the model are: DEM, grain-size features, rainfall, depth of bedrock and Manning coefficient values [24,41].

Rainfall precipitation represents the input to derivate catchment runoff, which in turn drives topographic changes (i.e., erosion and deposition) and controls fluvial and slope processes for the modeled time step [28]. Depths and velocities of the flow are estimated from flow discharges between raster cells using the Manning's equation and are then used to model both the sediment transport and erosion/deposition processes. Caesar–Lisflood estimates sediment transport in relation to nine grain-size fractions, which are selected by use. Sediment can be transported as bed load or as suspended load. Soil creep and landslide processes can be also included in the simulation [41,42] using a critical slope angle threshold. This condition allows the re-distribution of landslide and soil creep deposits from slopes to the fluvial system. Elevations and grain size features of the cells are updated according to the estimation of erosion/deposition and slope process. Model outputs are: (i) elevation changes; (ii) flow discharges; (iii) sediment fluxes at the outlet over time [24,28,41–43]. The model is able to reconstruct topographic changes at a sub-metric scale. Input data and model parameters represent the key to derive a robust predictive model, although a recent work by [44] demonstrated that results of

the Caesar–Lisflood LEM are influenced only by a limited number of parameters. More specifically, the authors suggest that spatial distribution of Manning coefficient and the selection of the sediment transport formula are the main sensitive parameters of the model results. For this reason, we have carefully selected these parameters: for example, Einstein's sediment transport formula [45] was reconstructed using laboratory tests on (predominantly) sand-based channels and we have here chosen this equation according to the prevalent grain-size deposits of the study area. A 5-m DEM was used for the simulation. Moreover, the other input parameters were accurately derived from lithological, climate, and land-use features of the study area. To introduce a representative framework of the study area, we have preliminarily reconstructed the bedrock depth through a field-based analysis of the lithological units. To this aim, a detailed lithological map has been drawn by review of previous works and new geological surveys. Moreover, field surveys of the soil depth have been performed for the different lithological units of the study area (Figure 2, [34]). This approach allowed us to infer the soil thickness and bedrock depth for each lithological. This kind of information was summarized in a map showing the isopachs of the mean soil thickness (Figure 2c). The map has been converted in a raster grid and was introduced in the model in order to set the depth of bedrock and grain-size distribution within the active layer where erosion and deposition processes are estimated by LEM. The layer of the bedrock has been derived in a GIS environment using a map algebra tool based on a subtraction between the soil thickness map and the DEM.

Hourly rainfall dataset was derived from a weather station located near the catchment outlet. Rainfall record covers a time interval of about 22 years, and it was used also for the dam-removal scenario.

Input data and model parameters are summarized in Table 1 (see also [34]). It is worthy of note that the estimation of the sedimentary budget base on the LEM simulation was already tested through a comparison between the total amount of eroded sediment volumes coming from the model results and direct measurement of the short-term (i.e., about 20 years) sediment storage within the artificial reservoir. The good accordance between the model results and direct measurements [34] suggests that the model can be used to simulate the dam removal scenario in a consistent way.

Table 1. Model parameters.

Number	Caesar–Lisflood Parameter	Value
1	Grain-size features (m)	0.0005, 0.001, 0.002, 0.004, 0.008, 0.016, 0.032, 0.064, 0.128
2	Grain-size distribution (total 1)	0.20, 0.18, 0.12, 0.06, 0.03, 0.03, 0.1, 0.25
3	Type of rainfall record	Hourly
4	Sediment transport equation	Einstein
5	Max erode limit (m)	0.01
6	Active layer thickness (m)	0.1
7	Lateral edge smoothing passes	40
8	Manning coefficient	0.015–0.1 (derived by land-use map)
9	Soil creep/diffusion value	0.0025
10	Slope failure threshold	40
11	Vegetation critical stress	100

Manning coefficient values were assigned (Table 2) according to a revision of the values proposed in previous works (see for example [46,47]) whereas the spatial distribution of the Manning coefficient follows the boundaries of the land use map of the study area (Figure 2b).

Table 2. Values of the Manning coefficient.

Number	Land-Use Cover	Manning Coefficient
1	Building and road	0.015
2	Agricultural areas	0.035
3	Sclerophyllous vegetation	0.05
4	Broad-leaved and mixed forests	0.1
5	Natural grasslands	0.03
6	Streams and water bodies	0.04

3.2. Dam-Removal Scenario

Two different scenarios were simulated in the study area (Table 3): the first one is the pre-dam removal scenario, where the modification of the initial topography (PreDR-T0, Table 3) has been simulated over a time interval of 20 years (Pre-DR-T20, Table 3). Such a scenario represents the present-day landscape and the simulation provided a reconstruction of the sediment flux in the reservoir and the short-term topographic changes of the fluvial and slope systems. Input parameters and boundary conditions are summarized in Table 1.

Table 3. Description of the simulation scenarios: the first scenario refers to the present-day geomorphological setting whereas scenario 2 infers the geomorphic changes induced by the dam removal.

Scenario	Period	Initial DEM	Final DEM	Description
1—Pre-dam removal	0–20 yr	Pre-DR-T0	Pre-Dr-T20	Present-day landscape, analysis of erosion and sedimentation in the closed drainage system
2—Post-dam removal	0–20 yr	Post-DR-T0	Post-Dr-T20	Removal of dam and related geomorphic response to base-level fall

The post-dam removal scenario has been developed removing the dam body to the initial DEM. More specifically, the DEM was created by subtracting to the original topography the dam height (PostDR-T0, Table 3). Post-dam removal simulation was run for a period of 20 years (PostDR-T20) using the same hourly rainfall data and input parameters of the Pre-DR scenario.

Output DEMs and raster of the topographic changes were analysed in a GIS environment to assess the pattern and rates of sediment flux and channel profile adjustments. Spatial distribution of the erosion/deposition processes, multi-temporal analysis of river longitudinal profiles, and valley topographic changes represent the key data to infer the geomorphic response of the study area to the simulated fall of the base-level.

4. Results

4.1. Scenario 1, Pre-Dam Removal

Outputs of the Caesar–Lisflood LEM are analysed in a GIS environment in order to investigate the geomorphic changes of the fluvial system and the spatial and temporal distribution of sediment erosion and deposition and their relationships with lithology, land use, and geomorphological processes. Figure 3 shows the hillshades representing the initial DEMs used for the modeling of the two simulation scenarios. Dam removal promoted an increase of the catchment area of about 0.6 kmq. The post-dam removal catchment includes the steeper reach of the Ficocchia stream, which flows in a deep V-shape valley.

As already described in the previous section, a recent work provided a comparison between LEM-based estimation of sediment flux of the Ficocchia catchment and direct measurements of reservoir sedimentation volumes [34]. This estimation covers a period (i.e., 18 years) similar to the simulation period of this work and highlights good accordance between model results and field-based data.

More specifically, LEM-based erosion volumes tend to underestimate the reservoir sedimentation of about 20%.

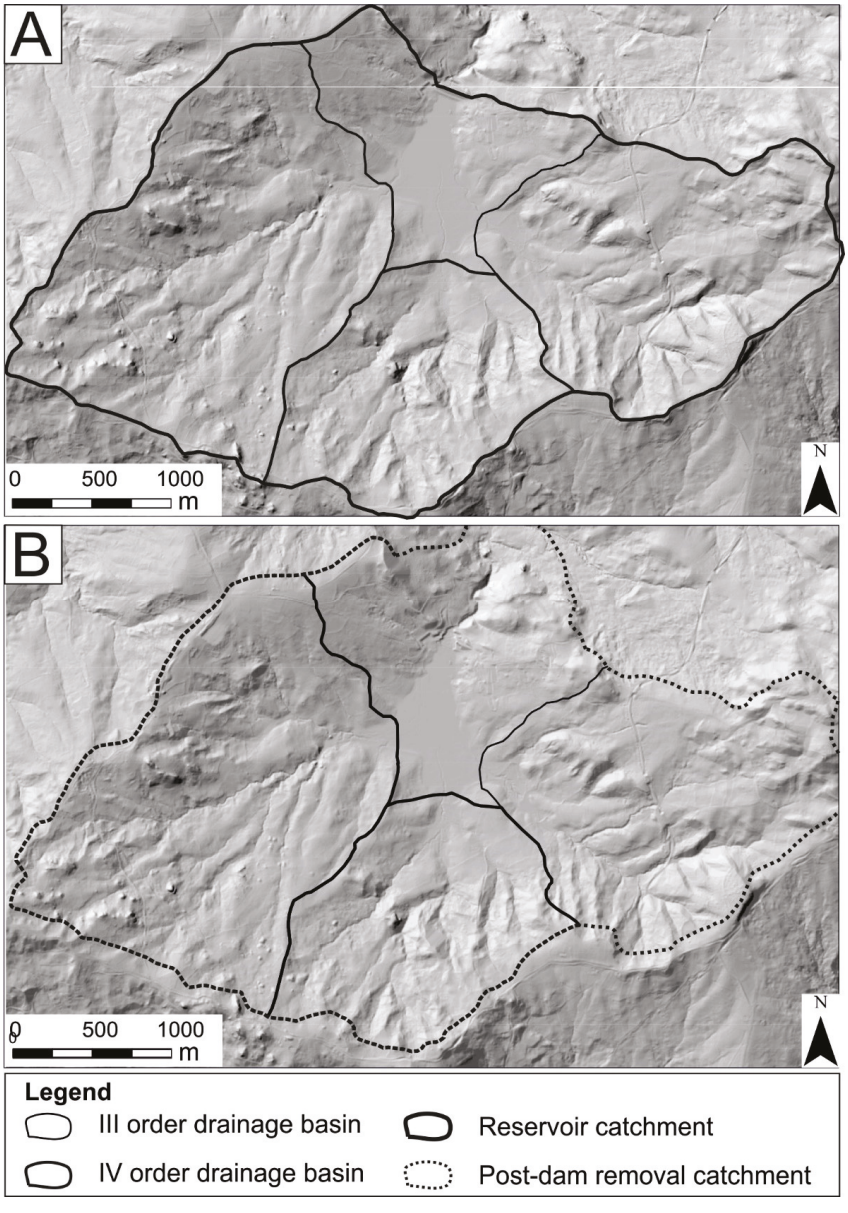

Figure 3. Hillshades representing the initial DEMs used for the modeling of the different simulation scenarios: (**A**) pre-dam removal, initial topography (PreDR-T0); (**B**) post-dam removal, simulation period: 1 year (PostDR-T0).

Simulation results of the pre-dam removal scenario are summarized in a DEM of difference (Figure 4), which shows the topographic changes at a sub-metric scale and sediment flux in the study area after 20 years. Visual inspection of the map allowed us to infer the short-term morpho-sedimentary evolution of mountain catchments and the influence of fluvial and hillslope processes on the geomorphological evolution and sediment delivery. The map highlights that erosion processes occurred along the main channels of the fluvial net whereas deposition is located in the artificial reservoir as a result of the flattening of longitudinal profiles in the lower reaches of the channels (Figure 4).

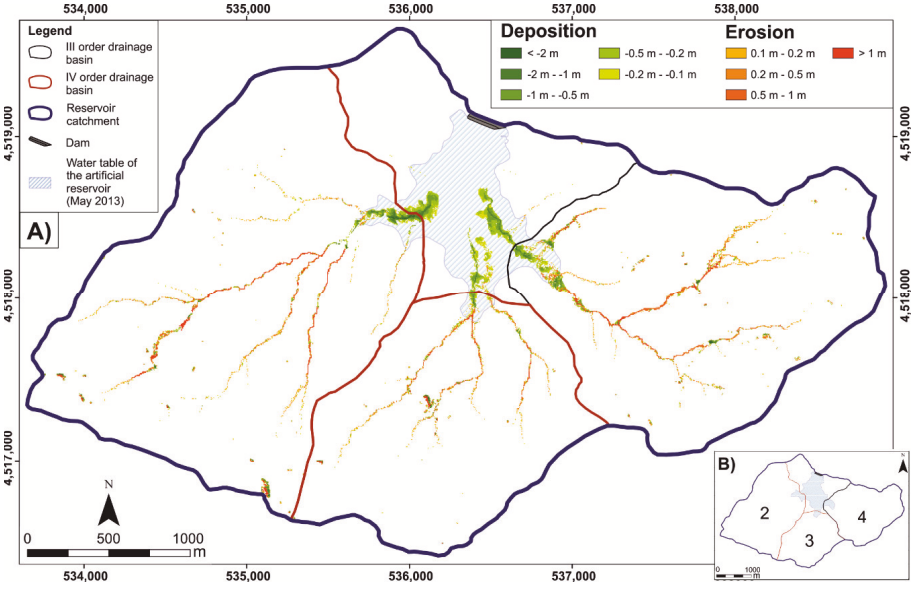

Figure 4. (**A**) Elevation difference map for the pre-dam removal scenario (simulation period: 20 years); (**B**) Numbering of the three sub-basins of the study area.

Model results seem to suggest a minor impact of slope processes on the sediment yield of the studied catchment, although landslide processes and high levels of the reservoir water table have been invoked as possible factors of slight differences between LEM-based erosion volumes and direct estimation of reservoir sedimentation [34]. In any case, modelling results fit well with the spatial distribution of landforms and deposits deriving by field-based geomorphological analysis. In fact, several geomorphological evidences such as V-shape valleys of the main channels and the absence of slope and alluvial deposits along the thalwegs is in accordance with the LEM results and suggest that channel incision upstream of the artificial reservoir is the main geomorphological processes controlling the morpho-sedimentary evolution of the Ficocchia catchment. As a matter of fact, sediment delivery ratio of the artificial reservoir is slightly higher than 0.9, testifying a high level of sediment connectivity of the study area.

Histogram of Figure 5 shows the results of the elevation changes caused by erosion and deposition after a time interval of 20 years. The total amount of erosion deriving by Caesar–Lisflood LEM simulation for the entire period is 84,070 m^3, which corresponds to a mean annual erosion volume of 4203 m^3/year (Figure 5). Stable areas represent 97.7% of the total area whereas the most representative erosion class has a value ranging from 0.1 to 0.5 m (Figure 5). Analysis of the contribution of each sub-basin to the sediment yield highlights that about 83% of the total amount of erosion volumes comes from catchment n.2 and n.4 (Figure 5).

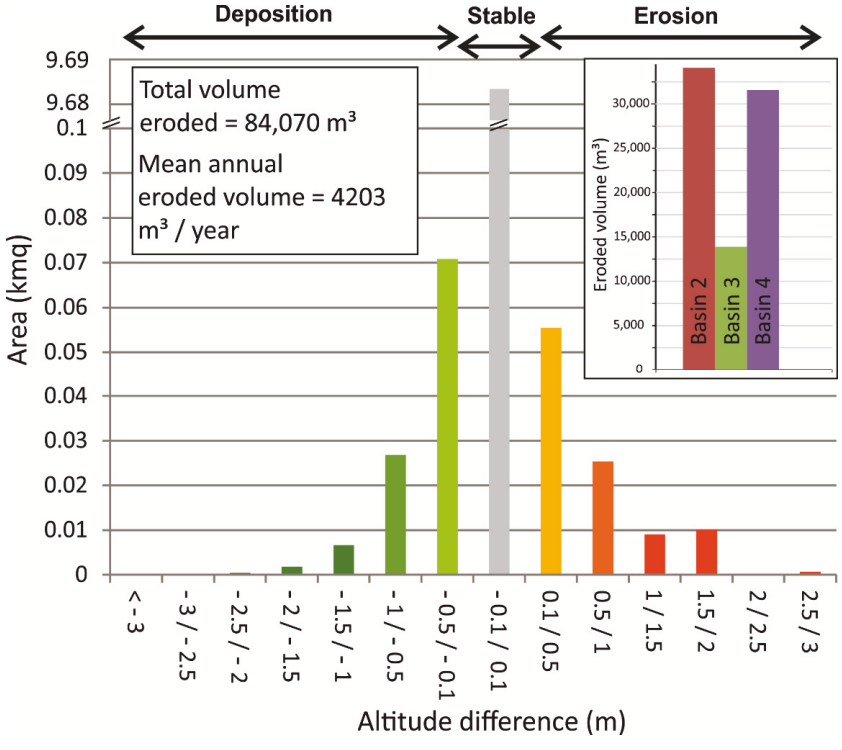

Figure 5. Erosion/deposition classes in the catchment deriving from the analysis of the altitude difference map of Figure 4. In the frame: distribution of the eroded volumes from the three sub-basins of the study area (numbering is shown in Figure 4).

4.2. Scenario 2–Dam Removal

Post-dam removal scenario (Post-DR, Table 3) was carried out over a 20-year period to perform a direct comparison with the sediment budget related to Scenario 1. Decadal-scale modelling of the geomorphic response to dam-removal predicts a strong modification of the fluvial system, with a general increase of topographic changes than the pre-dam removal scenario (Cfr. Figures 4 and 6). Altitude difference map (Figure 6) clearly highlights a significant increase of erosion processes in both the headwaters and mid sectors of the drainage net, which are mainly related to the higher incision ability of the main channels. In fact, a comparison between the results of the two simulations shows that lateral migration of channels appears to be limited (cf. Figures 4 and 6). LEM predicts the development of a wide floodplain in the flat area of the reservoir with a well-defined incision of the infill by the three main channels of the study area. In addition, analysis of the spatial pattern of erosion and deposition shows the occurrence of small sedimentation areas upstream to the reservoir infill (Figure 6), which contributed to a slight decrease of the sediment connectivity of the entire catchment.

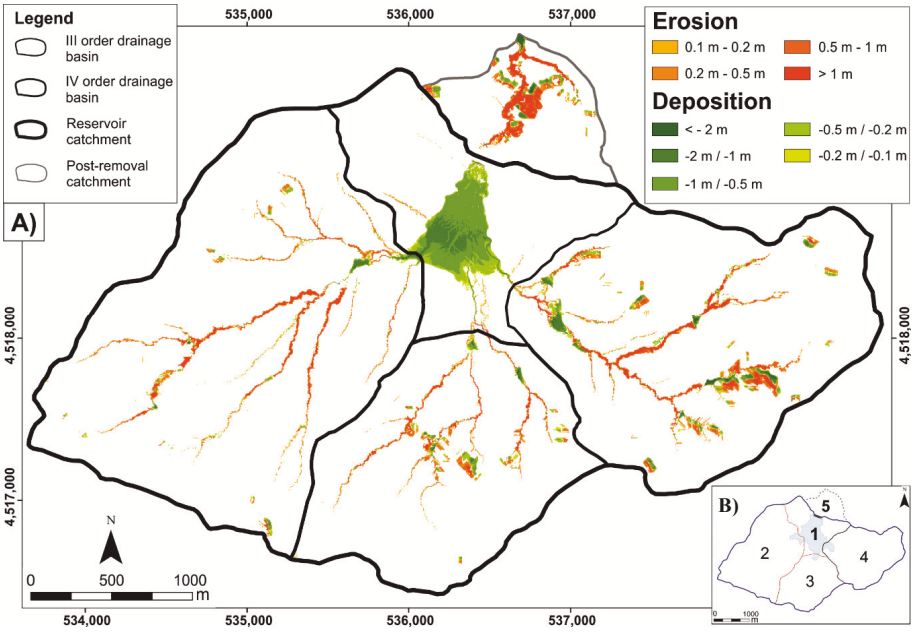

Figure 6. (**A**) Landscape evolution models (LEM)-based elevation difference map for the post-dam removal scenario (simulation period: 20 years). (**B**) Numbering of the post-dam removal catchments.

The frequency distribution of the altitude difference map (Figure 7) illustrates a higher erosional ability of the geomorphic system after the lowering of the base level.

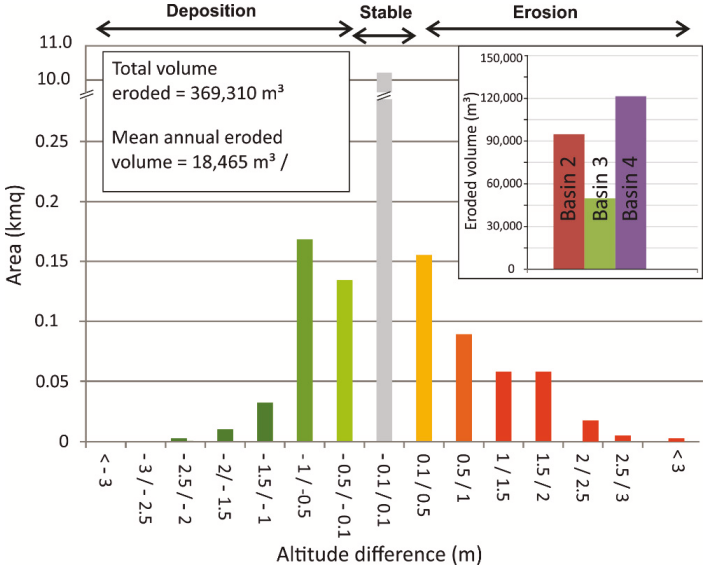

Figure 7. Statistical distribution of the altitude difference map of Figure 6 (Post-dam removal scenario). In the frame: distribution of the eroded volumes from the three sub-basins of the study area (numbering is shown in Figure 6).

In fact, the model predicts an increase of the total eroded volumes by a factor of 4.4 for the post-dam removal scenario whereas the mean annual erosion volumes increase from 4203 m^3/year to 18465 (Figure 7). Caesar–Lisflood simulation infers topographic modifications for a percentage of the total area of about 7.1% (corresponding to an area of 0.74 kmq). In this scenario, erosion classes with a value ranging from 0.1 to 0.5 m represent the maximum of the altitude difference map but the comparison with Scenario 1 shows a relative increase of the erosion classes with a higher value. Analysis of the spatial pattern of erosion for the different sectors of the study area shows that sub-basin 4 and 3 contribute to 45.7% and 18.7% of the total amount of eroded volumes yielded in the upland sectors.

Then, approximately 81.3% of the total amount of sediment eroded comes from sub-basin n.3 and n.4 (i.e., the easternmost and the central one), highlighting a higher erosion ability of these catchments for the dam removal scenario.

4.3. River Profile Analysis and Channel/Valley Modifications

Multitemporal analysis of longitudinal river profiles has been performed using the elevation data derived from the output DEMs for each scenario. The perturbation induced by the dam removal promoted a significant modification of the river profiles (Figure 8), with a complex spatial and temporal pattern of geomorphic adjustments. Moreover, our simulation also highlights the occurrence of 2-D channel modifications, which are mainly related to a lateral shift of the main channels in the higher altitude sectors surrounding the reservoir infill (Figure 8).

After the dam removal, the longitudinal profile evolution is mainly featured by a pronounced channel incision, which mainly occurred upward the flat area of the reservoir (Figure 8). In fact, the fast response of main channels to the base-level lowering is a lengthening of the longitudinal profiles, which promoted incision upstream of the former reservoir area (Figure 8, see the yellow curves and the black ones). Channel 2 adjusts its longitudinal profiles forming a major convex knickzone downstream of the removed dam, which retreats of about 180–200 m during the 20-year simulation period. A minor knickpoint can be observed in the three channels at an altitude of about 955–960 m, showing a lower rate of retreat (i.e., about 1 m/yr).

Cross profiles of Figure 9 furnished additional information about the landscape modification resulting from our simulation. Spatial and temporal evolution of valley/channel modification is complex, with alternating stages of incision and aggradation. Profiles located in the higher altitude sectors of the catchment are featured by meter-scale incision (see for example profile a-a', d-d' and e-e'); in this sector, the highest amount of deepening (i.e., about 3 m) can be observed at profile a-a'. Topographic profiles crossing the reservoir deposits shows a more complex response to dam removal due to a general tendency of channels to cut the infill in the southernmost sectors (Figure 9, see profile b-b' and f-f') and the occurrence of aggradation upward the removed dam (see for example the profile g-g', Figure 9). Pronounced incision phenomena occurred downstream of the dam, with a progressive deepening of the main channels of about 3 m over the 20-year simulation period (Figure 9, profile i-i' and l-l').

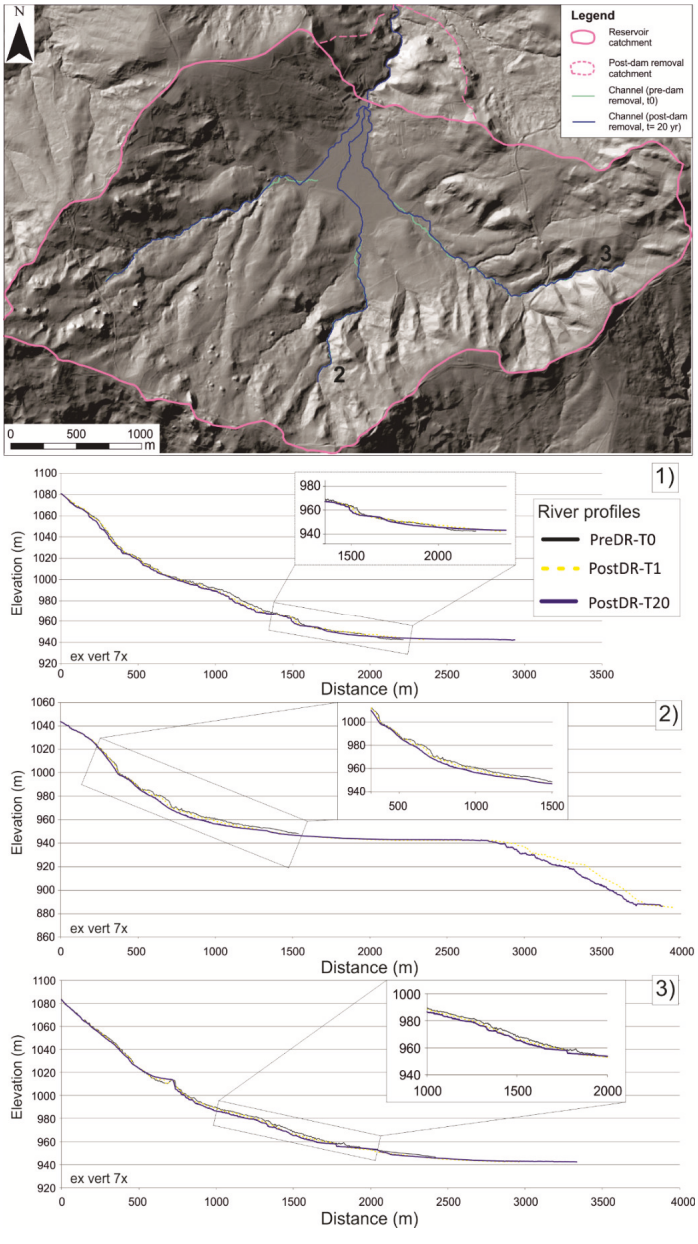

Figure 8. Map showing the planimetric changes of the main channels from the present-day landscape (initial DEM, Pre-DR-T0 in Table 3) to the final stage of the post-dam removal scenario. To the bottom: comparison of longitudinal river profiles of the three main channels (channel 1, 2 and 3 in the map) deriving from the simulation scenarios. River profile analysis highlights the amount of incision related to the base-level fall as well as the development of pronounced knickpoints in the upper and lower reaches of the main channels. Higher rates of knickpoint retreat are associated with the lower reach of the channel 2.

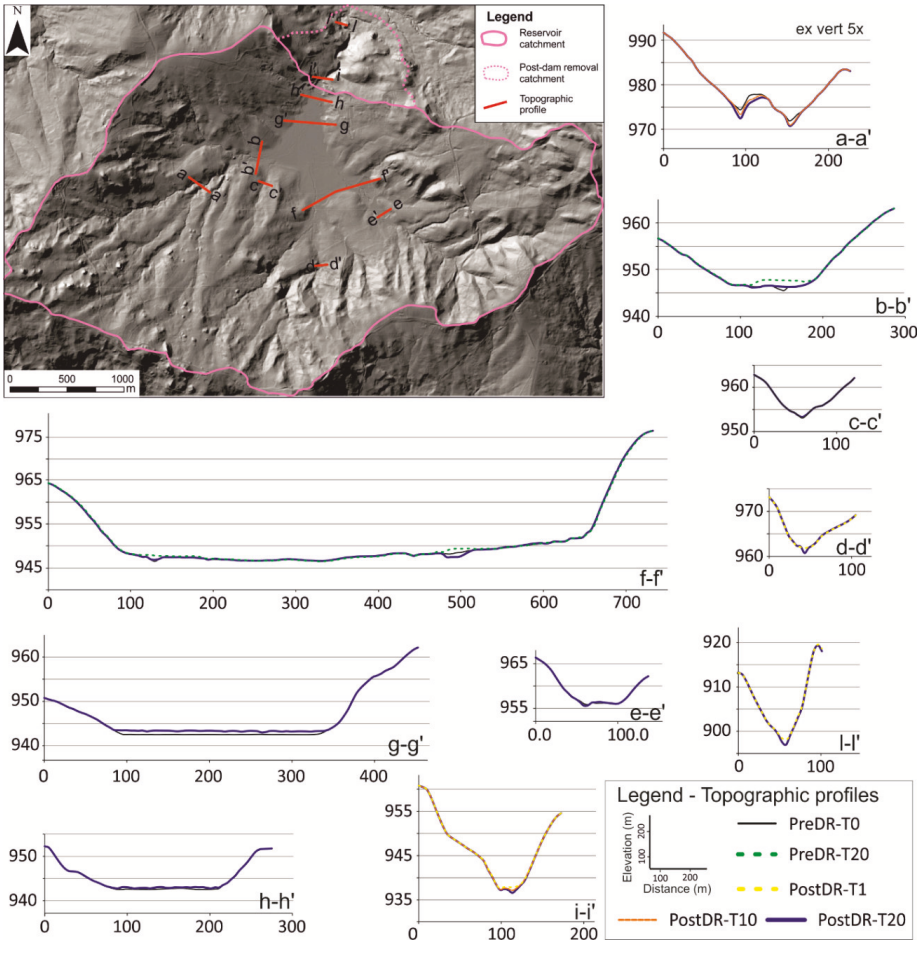

Figure 9. Topographic profiles for the different simulation scenarios (location of the profile is reported in the map) showing the landscape modification resulting from the simulation. Higher rates of fluvial incision occurred in the upper and lower reaches of the catchment (about 3 m over the 20-year simulation period, see for example profile a-a' and i-i'). A deep incision of the reservoir top can be also observed.

5. Discussion

LEM-based simulation of the geomorphic response of an upland catchment of southern Italian Apennine to dam removal suggests a complex spatial and temporal modification of channels and sediment flux. Model calibration and selection of the appropriate input parameters and boundary conditions are a critical issue for the LEM application in complex landscapes. (Skinner et al., 2018) [44] provided a detailed sensitivity analysis of the Caesar–Lisflood LEM, demonstrating that only some parameters such as sediment transport formula, Manning coefficient, and sediment grain sizes have a significant influence on model results.

Our approach based on a calibration of the model using direct measurements of sedimentation volumes in the artificial reservoir overcomes the issue of the complex selection of an excessive number of input and model parameters of the Caesar–Lisflood LEM, which are frequently ascribed as the main factor of its rare application [33,34,44].

In the study area, these parameters have been here derived by detailed field measurements and calibrated by the evaluation of an independent dataset. The preliminary validation of the short-term prediction ability of the Caesar–Lisflood LEM deriving from a direct comparison between model results and direct measurements of reservoir sedimentation volumes is a strong point of the proposed approach, which suggests the robustness of the model settings and parameterization. In fact, the limited difference between source-sink data confirms the robustness of the model and allowed us to consider our simulation as a robust estimation of topographic changes, geomorphological processes, and sediment flux at a short-term scale (i.e., 20 years) induced by base-level lowering. Such an approach can be effectively integrated with short-term analysis of geomorphic processes based on multitemporal comparison of high-resolution DEMs [48,49] and/or quantitative geomorphological analyses [8,50–52].

Our investigation demonstrated that Caesar–Lisflood LEM has a high potential to explore scenarios of morpho-sedimentary changes in response to different perturbing factors such as base-level fall or climate/land-use changes. The main advantage of the use of the LEM is its ability to reconstruct 2-D topographic modification and sediment flux, which can be investigated through advanced GIS-tools of map algebra and spatial statistics.

The geomorphic response to dam-removal scenario of the Ficocchia catchment mainly consists of a higher erosion ability of the channels in the upper reaches of the fluvial systems and a deep incision in the lowermost sectors of the post-dam removal catchment. As a matter of fact, quantitative analysis of the sediment dynamics resulting from the dam-removal scenario highlights a significant increase of the total eroded volumes in the post dam scenario of a factor higher than four. This significant increase of sediment yield is a common response of the fluvial system to base-level lowering, although our predicted erosion rates of the study area after the dam removal are significantly higher than the estimation coming from previous works (see for example [32]). For example, a recent analysis of the impact of multiple dam removal using Caesar–Lisflood LEM [32] reported a lower amount of sediment delivery induced by such a dam removal scenario.

This kind of response of the fluvial system to base-level lowering is in accordance with reconstruction made by other studies since it is mainly represented by upstream widespread incision associated to knickpoint retreat [17,19,21,32].

Predicted rates of knickpoint retreat reached values lower than those predicted by other researchers [32,53]. For example, a recent LEM-based analysis of multiple removals of narrow dams in Austria predicted annual knickpoint retreat rates ranging from 150 to 300 m [32], which is an order of magnitude higher than our results. As a matter of fact, our analysis highlights a peak of knickpoint retreat for the main channels of about 10 m/yr, see Figure 9).

The presence of a wide flat landscape coinciding with the former reservoir could represent the external factor that drives the complex and peculiar response of the study area. This sector can promote the dysconnectivity between the two steeper segments of the longitudinal profiles located upward and downward the removed dam, which could inhibit a faster retreat of the major knickpoint related to dam removal and promoted the formation of a wide floodplain in the mid sectors of the catchment. This observation confirms the relevant role of local parameters and physiographic setting (i.e., geometry and sedimentary features of the reservoir infill, bedrock and sediment erodibility, channel profile slope, etc.) in controlling the spatial distribution of erosion/deposition processes and the response of the fluvial system to severe perturbations induced by a fast base-level lowering, thus emphasizing the crucial role of landscape evolution models in the reconstruction of complex spatial and temporal changes of erosion and deposition induced by human disturbances.

6. Concluding Remarks

Simulation scenarios of sediment flux variation and topographic changes due to dam removal have been investigated in a reservoir catchment of southern Italy through the application of a landscape evolution model (i.e.: the Caesar–Lisflood LEM). LEM simulation highlights that the abrupt change in base-level due to dam removal induces a significant increase in erosion ability of main channels

and a strong incision of the reservoir infill. Analysis of the sediment dynamics resulting from the dam-removal highlights a significant increase of the total eroded volumes in the post dam scenario of a factor higher than four. Model results also predict a strong modification of the longitudinal profile of main channels induced by dam removal, which promoted deep fluvial incision in their upper and lower reaches.

Results are in agreement with previous analysis of the short-term response of the fluvial system, thus demonstrating the reliability of LEM-based analysis for solving open problems of short-term topographic changes and sedimentary budget induced by natural or human perturbations. The general good accordance between the model results and independent analysis based on field data ([34], see also paragraph 4.1) demonstrated both the general usefulness of the approach for the investigation of human-induced geomorphic disturbance of a landscape and the usefulness of the proposed approach than the application of 1-D simplified models. The main advantage of the use of the Caesar–Lisflood LEM in reconstructing the 2-D spatial and temporal pattern of topographic changes and related geomorphological processes is that the simulation scenarios can be easily compared with field data and historical maps, which can be also useful to explore the source of uncertainties, simplifications, and assumptions of the model.

Author Contributions: Conceptualization, D.G. and M.S.; methodology, D.G. and M.S.; software, D.G.; validation, D.G. and M.S.; formal analysis, D.G.; investigation, D.G. and M.S.; resources, D.G. and M.S.; data curation, D.G.; writing—original draft preparation, D.G.: writing—review and editing, D.G. and M.S.; visualization, D.G. and M.S.; supervision, D.G. and M.S.; project administration, D.G. and M.S.; funding acquisition, D.G. and M.S. All authors have read and agreed to the published version of the manuscript.

Funding: This research received no external funding.

Acknowledgments: We would like to thank the three anonymous referees for their helpful suggestions and constructive reviews. The first author would also like to thank Maurizio Lazzari (ISPC-CNR) for support in fieldwork and interesting discussions.

Conflicts of Interest: The authors declare no conflict of interest.

References

1. Dente, E.; Lensky, N.G.; Morin, E.; Grodek, T.; Sheffer, N.A.; Enzel, Y. Geomorphic Response of a Low-Gradient Channel to Modern, Progressive Base-Level Lowering: Nahal HaArava, the Dead Sea. *J. Geophys. Res. Earth Surf.* **2017**, *122*, 2468–2487. [CrossRef]
2. Neave, M.; Rayburg, S.; Swan, A. River channel change following dam removal in an ephemeral stream. *Aust. Geogr.* **2009**, *40*, 235–246. [CrossRef]
3. Joeckel, R.M.; Diffendal, R.F., Jr. Geomorphic and environmental change around a large, aging reservoir: Lake C. W. McConaughy, Western Nebraska, USA. *Environ. Eng. Geosci.* **2004**, *10*, 69–90. [CrossRef]
4. Struth, L.; Garcia-Castellanos, D.; Viaplana-Muzas, M.; Vergés, J. Drainage network dynamics and knickpoint evolution in the Ebro and Duero basins: From endorheism to exorheism. *Geomorphol* **2019**, *327*, 554–571. [CrossRef]
5. Rodríguez-Rodríguez, L.; Antón, L.; Pallàs, R.; García-Castellanos, D.; Jiménez-Munt, I.; Pastor-Martín, C. A GIS method to identify flat surfaces and restore relict fluvial long-profiles from terrace remnants gives new clues on how large basins respond to endorheic–exorheic transitions (Duero basin, Iberian Peninsula). *Earth Surf. Process. Landf.* **2020**, *45*, 1013–1027. [CrossRef]
6. Bilmes, A.; Veiga, G.D.; Ariztegui, D.; Castelltort, S.; D'Elia, L.; Franzese, J.R. Quaternary base-level drops and trigger mechanisms in a closed basin: Geomorphic and sedimentological studies of the Gastre Basin, Argentina. *Geomorphology* **2017**, *283*, 102–113. [CrossRef]
7. Cunha, P.P.; Martins, A.A.; Gomes, A.; Stokes, M.; Cabral, J.; Lopes, F.C.; Antón, L. Mechanisms and age estimates of continental-scale endorheic to exorheic drainage transition: Douro River, Western Iberia. *Glob. Planet. Chang.* **2019**, *181*, 102985. [CrossRef]
8. Buccolini, M.; Materazzi, M.; Aringoli, D.; Gentili, B.; Pambianchi, G.; Scarciglia, F. Late Quaternary catchment evolution and erosion rates in the Tyrrhenian side of central Italy. *Geomorphology* **2014**, *204*, 21–30. [CrossRef]

9. Giano, S.I.; Gioia, D.; Schiattarella, M. Morphotectonic evolution of connected intermontane basins from the southern Apennines, Italy: The legacy of the pre-existing structurally controlled landscape. *Rend. Lincei* **2014**, *25*, 241–252. [CrossRef]
10. Gioia, D.; Gallicchio, S.; Moretti, M.; Schiattarella, M. Landscape response to tectonic and climatic forcing in the foredeep of the southern Apennines, Italy: Insights from Quaternary stratigraphy, quantitative geomorphic analysis, and denudation rate proxies. *Earth Surf. Process. Landf.* **2014**, *39*, 814–835. [CrossRef]
11. Amato, A.; Aucelli, P.P.C.; Cinque, A. The long-term denudation rate in the Southern Apennines Chain (Italy): A GIS-aided estimation of the rock volumes eroded since middle Pleistocene time. *Quat. Int.* **2003**, *101*, 3–11. [CrossRef]
12. Capolongo, D.; Refice, A.; Bocchiola, D.; D'Addabbo, A.; Vouvalidis, K.; Soncini, A.; Stamatopoulos, L. Coupling multitemporal remote sensing with geomorphology and hydrological modeling for post flood recovery in the Strymonas dammed river basin (Greece). *Sci. Total Environ.* **2019**, *651*, 1958–1968. [CrossRef] [PubMed]
13. Burroughs, B.A.; Hayes, D.B.; Klomp, K.D.; Hansen, J.F.; Mistak, J. Effects of Stronach Dam removal on fluvial geomorphology in the Pine River, Michigan, United States. *Geomorphology* **2009**, *110*, 96–107. [CrossRef]
14. Major, J.J.; East, A.E.; O'Connor, J.E.; Grant, G.E.; Wilcox, A.C.; Magirl, C.S.; Tullos, D.D. Geomorphic responses to dam removal in the United States—*A* two-decade perspective. *Gravel Bed Rivers Process Disasters* **2017**, 355–383. [CrossRef]
15. Wang, H.-W.; Kuo, W.C. Geomorphic Responses to a Large Check-Dam Removal on a Mountain River in Taiwan. *River Res. Appl.* **2015**, *32*, 1094–1105. [CrossRef]
16. Randle, T.J.; Bountry, J.A.; Ritchie, A.; Wille, K. Large-scale dam removal on the Elwha River, Washington, USA: Erosion of reservoir sediment. *Geomorphology* **2015**, *246*, 709–728. [CrossRef]
17. Gartner, J.D.; Magilligan, F.J.; Renshaw, C.E. Predicting the type, location and magnitude of geomorphic responses to dam removal: Role of hydrologic and geomorphic constraints. *Geomorphology* **2015**, *251*, 20–30. [CrossRef]
18. Pearson, A.J.; Snyder, N.P.; Collins, M.J. Rates and processes of channel response to dam removal with a sand-filled impoundment. *Water Resour. Res.* **2011**, *47*, W08504. [CrossRef]
19. Sawaske, S.R.; Freyberg, D.L. A comparison of past small dam removals in highly sediment-impacted systems in the U.S. *Geomorphology* **2012**, *151*, 50–58. [CrossRef]
20. Walter, C.; Tullos, D.D. Downstream channel changes after a small dam removal: Using aerial photos and measurement error for context; Calapooia River, Oregon. *River Res. Appl.* **2010**, *26*, 1220–1245. [CrossRef]
21. Wells, R.R.; Langendoen, E.J.; Simon, A. Modeling Pre- and Post-Dam Removal Sediment Dynamics: The Kalamazoo River, Michigan1. *Jawra J. Am. Water Resour. Assoc.* **2007**, *43*, 773–785. [CrossRef]
22. Cui, Y.; Parker, G.; Braudrick, C.; Dietrich, W.E.; Cluer, B. Dam Removal Express Assessment Models (DREAM). *J. Hydraul. Res.* **2006**, *44*, 308–323. [CrossRef]
23. Benaïchouche, A.; Stab, O.; Tessier, B.; Cojan, I. Evaluation of a landscape evolution model to simulate stream piracies: Insights from multivariable numerical tests using the example of the Meuse basin, France. *Geomorphology* **2016**, *253*, 168–180. [CrossRef]
24. Coulthard, T.J.; Hancock, G.R.; Lowry, J.B.C. Modelling soil erosion with a downscaled landscape evolution model. *Earth Surf. Process. Landf.* **2012**, *37*, 1046–1055. [CrossRef]
25. Temme, A.J.A.M.; Peeters, I.; Buis, E.; Veldkamp, A.; Govers, G. Comparing landscape evolution models with quantitative field data at the millennial time scale in the Belgian loess belt. *Earth Surf. Process. Landf.* **2011**, *36*, 1300–1312. [CrossRef]
26. Van Gorp, W.; Temme, A.J.; Baartman, J.E.; Schoorl, J.M. Landscape Evolution Modelling of naturally dammed rivers. *Earth Surf. Process. Landf.* **2014**, *39*, 1587–1600. [CrossRef]
27. Refice, A.; Giachetta, E.; Capolongo, D. SIGNUM: A Matlab, TIN-based landscape evolution model. *Comput. Geosci.* **2012**, *45*, 293–303. [CrossRef]
28. Coulthard, T.J.; van de Wiel, M.J. Modelling long term basin scale sediment connectivity, driven by spatial land use changes. *Geomorphology* **2017**, *277*, 265–281. [CrossRef]
29. Hancock, G.R.; Coulthard, T.J.; Martinez, C.; Kalma, J.D. An evaluation of landscape evolution models to simulate decadal and centennial scale soil erosion in grassland catchments. *J. Hydrol.* **2011**, *398*, 171–183. [CrossRef]

30. Tucker, G.E.; Hancock, G.R. Modelling landscape evolution. *Earth Surf. Process. Landf.* **2010**, *35*, 28–50. [CrossRef]
31. Lowry, J.B.C.; Narayan, M.; Hancock, G.R.; Evans, K.G. Understanding post-mining landforms: Utilising pre-mine geomorphology to improve rehabilitation outcomes. *Geomorphology* **2019**, *328*, 93–107. [CrossRef]
32. Poeppl, R.E.; Coulthard, T.; Keesstra, S.D.; Keiler, M. Modeling the impact of dam removal on channel evolution and sediment delivery in a multiple dam setting. *Int. J. Sediment Res.* **2019**, *34*, 537–549. [CrossRef]
33. Temme AJ, A.M.; Claessens, L.; Veldkamp, A.; Schoorl, J.M. Evaluating choices in multi-process landscape evolution models. *Geomorphology* **2011**, *125*, 271–281. [CrossRef]
34. Gioia, D.; Lazzari, M. Testing the Prediction Ability of LEM-Derived Sedimentary Budget in an Upland Catchment of the Southern Apennines, Italy: A Source to Sink Approach. *Water* **2019**, *11*, 911. [CrossRef]
35. Schiattarella, M.; Giano, S.I.; Gioia, D. Long-term geomorphological evolution of the axial zone of the Campania-Lucania Apennine, southern Italy: A review. *Geol. Carpathica* **2017**, *68*, 57–67. [CrossRef]
36. Giannandrea, P.; Marino, M.; Romeo, M.; Schiattarella, M. Pliocene to Quaternary evolution of the Ofanto Basin in southern Italy: An approach based on the unconformity-bounded stratigraphic units. *Ital. J. Geosci.* **2013**, *133*, 27–44. [CrossRef]
37. Labella, R.; Capolongo, D.; Giannandrea, P.; Giano, S.I.; Schiattarella, M. Morphometric analysis of fluvial network and age constraints of terraced surfaces of the Ofanto basin, Southern Italy. *Rend. Lincei* **2014**, *25*, 253–263. [CrossRef]
38. Piccarreta, M.; Pasini, A.; Capolongo, D.; Lazzari, M. Changes in daily precipitation extremes in the Mediterranean from 1951 to 2010: The Basilicata region, southern Italy. *Int. J. Climatol.* **2013**, *33*, 3229–3248. [CrossRef]
39. Büttner, G. CORINE land cover and land cover change products. In *Remote Sensing and Digital Image Processing*; Manakos, I., Braun, M., Eds.; Springer: Dordrecht, The Netherlands, 2014.
40. Ramirez, J.A.; Zischg, A.P.; Schürmann, S.; Zimmermann, M.; Weingartner, R.; Coulthard, T.; Keiler, M. Modeling the geomorphic response to early river engineering works using CAESAR-Lisflood. *Anthropocene* **2020**, *32*, 100266. [CrossRef]
41. Coulthard, T.J.; Neal, J.C.; Bates, P.D.; Ramirez, J.; de Almeida, G.A.; Hancock, G.R. Integrating the LISFLOOD-FP 2D hydrodynamic model with the CAESAR model: Implications for modelling landscape evolution. *Earth Surf. Process. Landf.* **2013**, *38*, 1897–1906. [CrossRef]
42. Coulthard, T.J.; van de Wiel, M.J. Climate, tectonics or morphology: What signals can we see in drainage basin sediment yields? *Earth Surf. Dyn.* **2013**, *1*, 13–27. [CrossRef]
43. Hancock, G.R.; Lowry, J.B.C.; Coulthard, T.J.; Evans, K.G.; Moliere, D.R. A catchment scale evaluation of the SIBERIA and CAESAR landscape evolution models. *Earth Surf. Process. Landf.* **2010**, *35*, 863–875. [CrossRef]
44. Skinner, C.J.; Coulthard, T.J.; Schwanghart, W.; Wiel, M.J.; Hancock, G. Global sensitivity analysis of parameter uncertainty in landscape evolution models. *Geosci. Model Dev.* **2018**, *11*, 4873–4888. [CrossRef]
45. Einstein, H.A. The Bed-Load Function for Sediment Transportation in Open Channel Flows. *Soil Conserv. Serv.* **1950**, *1026*, 1–31.
46. Ding, Y.; Jia, Y.; Sam, S.Y.W. Identification of Manning's Roughness Coefficients in Shallow Water Flows. *J. Hydraul. Eng.* **2004**, *130*, 501–510. [CrossRef]
47. Phillips, J.V.; Tadayon, S. *Selection of Manning's Roughness Coefficient for Natural and Constructed Vegetated and Non-Vegetated Channels, and Vegetation Maintenance Plan Guidelines for Vegetated Channels in Central Arizona*; Report 2006-5108; USGS: Washington, DC, USA, 2006.
48. Aucelli, P.P.; Conforti, M.; Della Seta, M.; Del Monte, M.; D'uva, L.; Rosskopf, C.M.; Vergari, F. Multi-temporal Digital Photogrammetric Analysis for Quantitative Assessment of Soil Erosion Rates in the Landola Catchment of the Upper Orcia Valley (Tuscany, Italy). *Land Degrad. Dev.* **2016**, *27*, 1075–1092. [CrossRef]
49. Llena, M.; Vericat, D.; Smith, M.W.; Wheaton, J.M. Geomorphic process signatures reshaping sub-humid Mediterranean badlands: 1. Methodological development based on high-resolution topography. *Earth Surf. Process. Landf.* **2020**, *45*, 1335–1346. [CrossRef]
50. Del Monte, M.; Vergari, F.; Brandolini, P.; Capolongo, D.; Cevasco, A.; Ciccacci, S.; Zucca, F. Multi-method evaluation of denudation rates in small mediterranean catchments. In *Engineering Geology for Society and Territory—Volume 1: Climate Change and Engineering Geology*; Springer: Cham, Switzerland, 2015; pp. 563–567.
51. Gioia, D.; Martino, C.; Schiattarella, M. Long- to short-term denudation rates in the southern Apennines: Geomorphological markers and chronological constraints. *Geol. Carpathica* **2011**, *62*, 27–41. [CrossRef]

52. Piccarreta, M.; Capolongo, D.; Boenzi, F.; Bentivenga, M. Implications of decadal changes in precipitation and land use policy to soil erosion in Basilicata, Italy. *Catena* **2006**, *65*, 138–151. [CrossRef]
53. Doyle, M.W.; Stanley, E.H.; Harbor, J.M. Channel adjustments following two dam removals in Wisconsin. *Water Resour. Res.* **2003**, *39*, 1011. [CrossRef]

applied sciences

MDPI

Article

Comparison of Satellite and Drone-Based Images at Two Spatial Scales to Evaluate Vegetation Regeneration after Post-Fire Treatments in a Mediterranean Forest

Jose Luis Martinez [1], Manuel Esteban Lucas-Borja [1], Pedro Antonio Plaza-Alvarez [1], Pietro Denisi [2], Miguel Angel Moreno [3], David Hernández [3], Javier González-Romero [1] and Demetrio Antonio Zema [2,*]

[1] Escuela Técnica Superior Ingenieros Agrónomos y Montes, Campus Universitario, Universidad de Castilla-La Mancha, E-02071 Albacete, Spain; joseluis.martinez6@alu.uclm.es (J.L.M.); ManuelEsteban.Lucas@uclm.es (M.E.L.-B.); Pedro.Plaza@uclm.es (P.A.P.-A.); Javier.Gromero@uclm.es (J.G.-R.)
[2] Department AGRARIA, Mediterranean University of Reggio Calabria, Loc. Feo di Vito, I-89122 Reggio Calabria, Italy; pietro.denisi@unirc.it
[3] Institute of Regional Development, University of Castilla-La Mancha, E-02071 Albacete, Spain; MiguelAngel.Moreno@uclm.es (M.A.M.); David.Hernandez@uclm.es (D.H.)
* Correspondence: dzema@unirc.it

Abstract: The evaluation of vegetation cover after post-fire treatments of burned lands is important for forest managers to restore soil quality and plant biodiversity in burned ecosystems. Unfortunately, this evaluation may be time consuming and expensive, requiring much fieldwork for surveys. The use of remote sensing, which makes these evaluation activities quicker and easier, have rarely been carried out in the Mediterranean forests, subjected to wildfire and post-fire stabilization techniques. To fill this gap, this study evaluates the feasibility of satellite (using LANDSAT8 images) and drone surveys to evaluate changes in vegetation cover and composition after wildfire and two hillslope stabilization treatments (log erosion barriers, LEBs, and contour-felled log debris, CFDs) in a forest of Central Eastern Spain. Surveys by drone were able to detect the variability of vegetation cover among burned and unburned areas through the Visible Atmospherically Resistant Index (VARI), but gave unrealistic results when the effectiveness of a post-fire treatment must be evaluated. LANDSAT8 images may be instead misleading to evaluate the changes in land cover after wildfire and post-fire treatments, due to the lack of correlation between VARI and vegetation cover. The spatial analysis has shown that: (i) the post-fire restoration strategy of landscape managers that have prioritized steeper slopes for treatments was successful; (ii) vegetation growth, at least in the experimental conditions, played a limited influence on soil surface conditions, since no significant increases in terrain roughness were detected in treated areas.

Keywords: VARI; log erosion barrier; contour-felled log debris; land restoration; vegetation cover

Citation: Martinez, J.L.; Lucas-Borja, M.E.; Plaza-Alvarez, P.A.; Denisi, P.; Moreno, M.A.; Hernández, D.; González-Romero, J.; Zema, D.A. Comparison of Satellite and Drone-Based Images at Two Spatial Scales to Evaluate Vegetation Regeneration after Post-Fire Treatments in a Mediterranean Forest. *Appl. Sci.* **2021**, *11*, 5423. https://doi.org/10.3390/app11125423

Academic Editors: Dario Gioia and Maria Danese

Received: 16 March 2021
Accepted: 8 June 2021
Published: 10 June 2021

1. Introduction

Wildfires can negatively affect soil fertility, biodiversity, land resources, global warming, and human assets; however, positive environmental effects are also recognized, such as increased forest regeneration and nutrient recycling [1]. The Mediterranean ecosystems are adapted to fire disturbance, but the increasing recurrence and high severity of wildfires generate high soil loss and reduce the ability of vegetation to recover [2].

In the Mediterranean Basin, wildfires burn large forest areas not only during summer, but also in mid seasons, when heavy rainstorms may occur [3,4]. For instance, in Spain, even though the number of wildfires has followed a decreasing trend in the last decades [5], wildland is still severely affected by forest wildfires in summer. In the last 10 years, more than 3000 km^2 of forests have burned. Only in 2018, over 7000 wildfires burned about 300 km^2 of forests [5].

The hydrological and ecological effects of large wildfires (floods, landslides and mudslides, erosion, loss of biodiversity, destruction of fauna, etc.) can be devastating [6]. Among these effects, soil erosion is presumably the most severe consequence of forest fires, since it threatens water resources, infrastructures, and populations inside and out of burned areas [7]. For burned soils, erosion after wildfire is much higher compared to unburned, since fire changes several physical and chemical properties of soil [1,7]. For instance, erosion in burned forest areas increases by even 30 times compared to the natural values recorder in unburned zones [8]. To reduce, under tolerable limits, soil erosion, urgent restoration actions are implemented immediately after the wildfire to prevent secondary post-fire damage, whereas long-term restoration can be used for regenerating plants and promoting the evolution of forest structure [9].

Management actions in fire-affected forests have typically focused on soil structure and plant recovery. The increase in vegetal cover through plant regeneration has been identified by some studies in Mediterranean regions as the main driver in post-fire management of forests [10]. Among the post-fire restoration actions, log erosion barriers (hereinafter indicated as "LEB") or contour-felled log debris (CFD) are widespread measures to control the erosive processes (mainly due to runoff and sediment flows) in forest ecosystems [11]. More specifically, LEBs are built by felling burned trees, while CFDs consist of branch and small-felling burned trees, and both are laid on the ground along the slope contour. Many studies have assessed the effectiveness of hillslope stabilization treatments on soil hydrological response (namely runoff and erosion) (e.g., [12–15] as well as reductions in CO_2 emissions and carbon sequestration [16]. In some cases, the impact of these actions in reducing runoff and trapping sediments is limited to the less intense rainfall events (e.g., [11]). In other cases, their effects are scarce or negligible, due to inadequate constructions or deficient design [13]. Some studies have even shown a negative impact, in terms of a higher percentage of bare and stony soil, especially in sunny areas subjected to different forest treatments, with subsequent increase in soil erosion [17]. It is evident that the effects of post-fire hillslope treatments are still uncertain, and the most suitable technique has not been completely identified [18].

A monitoring activity of post-fire management actions in burned forests in the Mediterranean environment may give forest managers and landscape planners insight about their effectiveness in reducing soil loss and accelerating the vegetation recovery. This activity is essential, since public administrations make large efforts and spend many resources in restoration actions that usually include economic, cultural and even landscape components [19,20]. However, the techniques of field monitoring are generally expensive and time-consuming [21]. The remote sensing techniques (using satellites and drones) are new tools to make land surveys quicker and cheaper [22]. Remote sensing is usually applied in fire-affected areas for fire risk and fuel mapping, active fire detection, burned area estimates, burn severity assessment, and post-fire monitoring vegetation recovery [23]. The remote sensing techniques using satellite images are able to evaluate post-fire regeneration with increasingly improved spatial, temporal and radiometric resolutions [24]. In the last decade, the appearance of unmanned aerial vehicles has increased the use of remote sensing application to agro-forestry [25,26]. UAV technology is promising for monitoring vegetation regrowth, since the spatial resolution and temporal intervals of surveys are not dependent on satellite orbits [23]. Despite their versatility and low cost, UAVs are not widely used to survey wide areas due to legal and technical limitations (e.g., autonomy, payload capacity) [27]. The assessment of wildfire effects and post-fire regeneration using remote sensing has been done through the calculation of spectral vegetation indices [28]. These indices are calculated using the electromagnetic wave reflectance data of vegetation using passive sensors [29]. Several studies have successfully developed and applied vegetation indices (e.g., the Normalized Difference Vegetation Index, NDVI; the Composite Burn Index, CBI; the Differenced Normalized Burn Ratio, DNBR, and the Visible Atmospherically Resistant Index, VARI [24]. In this regard, Gitas et al. [25] published a comprehensive review about remote sensing of post-fire vegetation recovery and highlighted the impor-

tant role of remote sensing in the future as well as the need to perform more studies in Mediterranean areas. Bhagat et al. [26] reported that UAVs provide data at fine resolution with the desired temporal resolution, which make them cost-effective and efficient data collectors. Regarding satellite images, Sirin et al. [29] was able to compare different multispectral satellite data to assess vegetation cover in abandoned lands and rewetted peatlands. Bright et al. [30] analyzed post-wildfire recovery in different coniferous forest types in North America using the Normalized Burn Ratio (NBR) derived from LandTrendr images. The same index was used in the same environment by Lentile et al. [31] to monitor post-fire burn severity and vegetation response following eight large wildfires. In the Mediterranean Basin, post-fire vegetation recovery was assessed by Bastos et al. [32] in Portugal (using the VEGETATION sensor), Lasaponara et al. [33] in Italy (using satellite MODIS data), and Polycronaki et al. [34] in Greece (using optical and SAR data [35].

Regarding VARI, several applications have been carried out in different research fields. For example, Schneider et al. [36] showed that VARI outperforms other indexes in distinguishing historical wildfire data in southern California. In the same environment, Stow et al. [37] demonstrated better performances of VARI compared to another normalized index (Normalized Difference Water Index, NDWI) in monitoring chaparral moisture content. Munoz et al. [38] found that VARI was more effective in estimating the fraction of vegetation cover and recognizing the different land use compared to NDVI index, observing a standard error lower than 8%. From these studies, the feasibility of VARI to estimate variable levels of land cover emerges. However, applications of this index for evaluation of vegetation regeneration in fire-affected areas are very scarce. Only Larrinaga and Brotons [39] calculated four greenness indices (among them VARI) to analyze post-fire regeneration of Mediterranean forests. Christakopoulos et al. [40] proposed a comparative evaluation of restoration practices using remote sensing and GIS in naturally-regenerating and reforested areas of Greece. No research is available about the estimation of vegetation recovery after hillslope stabilization techniques using VARI applied to satellite or UAV surveys. This leaves the usability of these methods in post-fire management of forests not well understood, to date.

To fill this gap, the current study evaluates the ability of VARI, estimated by both satellite and UAV images, to quantify the vegetation recovery after post-fire treatments (LEBs and CFDs) in a Mediterranean forest of Central Eastern Spain. Possible correlations between the vegetation cover measured in field plots and VARI values estimated from satellite (LANDSAT8) or UAV images, are identified. Processing of this information at two spatial scales (catchment and hillslope) allows validation of one or both methods.

2. Materials and Methods

2.1. Study Area

The investigation was carried out in the Sierra de los Donceles (municipality of Hellín, Castilla-La Mancha region, southeast Spain) (Figure 1a,b). This mountain forest lies in the most northeastern part of the Penibetic system with a southeast-northwest aspect. The landscape is patchy with steep slopes (sometimes over 25–30%), predominantly exposed to south-southeast, and ranges between 304 and 808 m above sea level with an average altitude of 506 m.

In this forest, one catchment (hereinafter "catchment area" or "catchment scale") and one hillslope ("hillslope area" or "hillslope scale") were selected, both subject to burning and post-fire restoration actions (Figure 1c,d). In these areas, plots for survey of vegetation were installed, as detailed in Section 2.2, and remote sensing-based analysis (using satellite or drone for the catchment and hillslope scale, respectively).

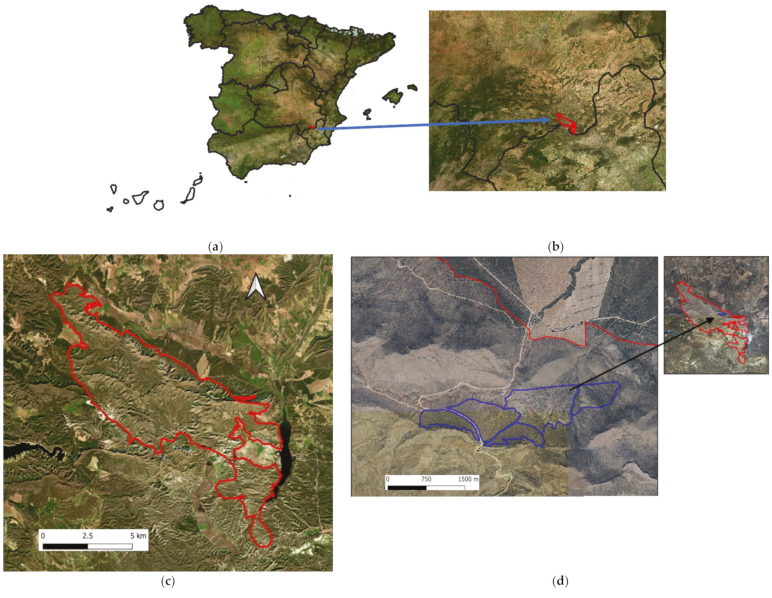

Figure 1. Location (**a**) and aerial map (**b**) of the study area, catchment area (**c**) and hillslope area (**d**) in Sierra de los Donceles forest (Castilla La Mancha, Spain).

The climate of the region is semi-arid Mediterranean. The study area is located in the Mesomediterranean bioclimatic belt [41], which is characterized by a dry climate with scarce rainfalls and a large variability of temperature. The mean annual precipitation is 321 mm and the mean temperature is 16.6 °C (minimum and maximum mean temperatures of −2 and 40 °C, respectively, in February and July (Spanish Agency for Meteorology, AEMET, period of 1981–2010) [42]. According to the Spanish soil map [43], soils belong to the Aridisol order and Calcic suborder, according to the classification established by the Soil Taxonomy System [44].

A large part of the study area is covered by a sclerophyllous vegetation dominated by *Pinus halepensis* Mill forests and with understory mainly consisting of *Quercus coccifera, Rhamnus lycioides, Halimium hatriplicifolium, Rosmarinus officinalis, Cistus clusii, Rhamnus alaternis, Phamnus alaternis, Genista spartioides* subsp. *Retamoid*; south-facing areas are dominated by *Stipa spartans* and natural therophytic grasslands. Before the wildfire, tree height and density of *Pinus halepensis* M. were 5 to 12 m and 450 to 775 individuals per hectare, respectively [45]. The wildfire occurred on July 2012, and burned a total area of 6500 ha of forest. The fire propagation was very fast, and most of the land was affected by moderate to high fire severity. After the fire, the Forest Service of Castilla-La Mancha region carried out post-fire restoration works, stabilization treatments on hillslopes (both log erosion barriers and contour-felled log debris) in autumn 2012, and checked dams in the catchment reaches in 2013 (Figure 2b,d and Figure 3).

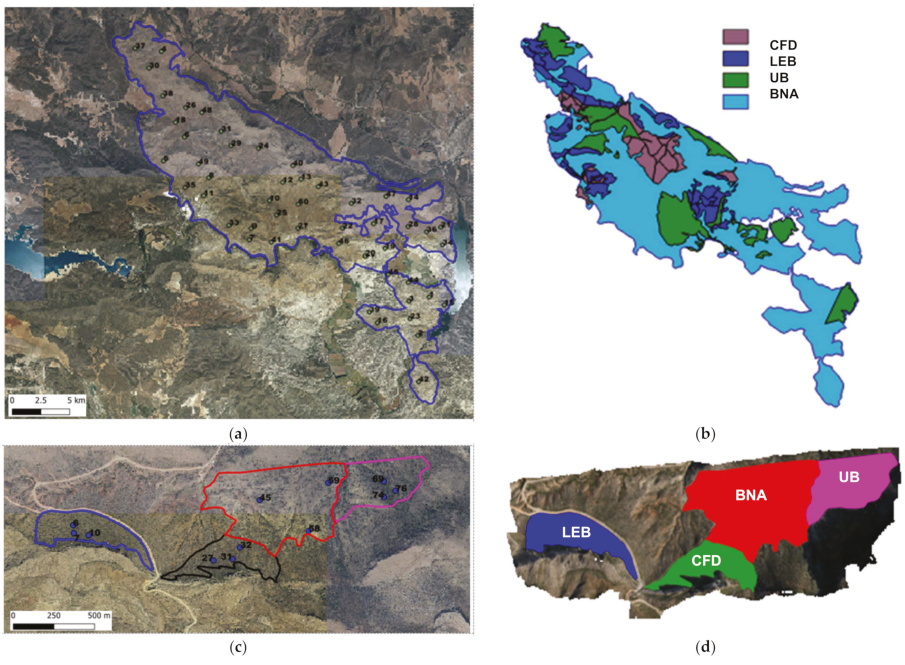

Figure 2. Plot location and distribution of soil conditions in the catchment (**a**,**b**) and hillslope (**c**,**d**) areas in Sierra de los Donceles forest (Castilla La Mancha, Spain). Log erosion barriers ("LEB"), contour-felled log debris ("CFD"), burned and no action ("BNA"), unburned ("UB").

Figure 3. Photos of the construction of contour-felled log debris (**a**) and log erosion barriers (**b**) in Sierra de los Donceles forest (Castilla La Mancha, Spain).

2.2. Experimental Design

The catchment selected in the studied area was subject to a wildfire and treated with the two hillslope stabilization treatments, consisting of log erosion barriers ("LEB") and contour-felled log debris ("CFD") (Figure 3). LEBs were built by felling burned trees that are laid on the ground along the slope contour [46]. Each log was anchored in-place and the space between the log and soil surface was filled with soil to create a storage basin upstream of the LEB, where the water and sediment flows are trapped. Earthen berms were sometimes installed to reduce the share of water circumventing the log sides. In the studied catchment, the stabilization treatment was operated at a mean density of 30 LEBs per hectare with a mean length of 10 m (for a linear density of 300 m of logs per ha). These

densities were limited by the scarce availability of wood material, due to the unsuitable type of vegetation in the area (small-diameter and low-density trees). The CFD treatment consisted of branch and small-felling burned trees, which were laid on the ground along the slope contour, as for LEB. In this case, logs were not anchored. The mean treatment density was 17 CFD per ha with a mean length of 50 m (corresponding to 850 m per ha), given the lower compaction and concentration of the material for building the CFD.

Moreover, a burned area was left without any treatment (henceforth "burned and no action", BNA) (Figure 2). Another area that was located very close to the burned forest and not affected by fire was considered ("unburned", UB); the vegetation and soil of this area was extremely similar as those of the burned zone and it was therefore representative of the actual pre-fire conditions. Table 1 reports the vegetation cover in the plots under four land conditions at the two spatial scales.

Table 1. Pre-fire forest cover in plots under four land conditions before the wildfire of 2012 in Sierra de los Donceles forest (Castilla-La Mancha, Spain).

Plot Scale	Land Condition	Forest Cover (%)
Hillslope	LEB	78–84
	CFD	77–81
	BNA	69–75
	UB	77–91
Catchment	LEB	73–84
	CFD	71–79
	BNA	81–87
	UB	78–83

Notes: UB = unburned; BNA = burned and no action; CFD = contour-felled log debris; LEB = log erosion barriers; data source: surveys of the Forest Service of Castilla-La Mancha region.

The vegetation cover was characterized in all plots under the four soil conditions. More specifically, in the UB plots, the vegetation cover is mainly characterized by woody and herbaceous species (specifically, *Pinus halepensis, Rosmarinus officinalis, Brachypodium retusum* and *Cistus albidus*). *Pinus halepensis, Cistus albidus* and *Rosmarinus officinalis* can largely be disseminated; their seeds, after fire, are stimulated to germinate. Conversely, *Brachypodium retusum* is a herbaceous species (hemicryptophyte), which is a facultative disseminator, with the ability to reproduce both from sprouts and seed and to adapt to frequent fires. In the BNA plots, *Brachypodium retusum, Cistus albidus, Halimium halimifolium, Quercus coccifera, Klasea flavescens* subsp *cichoracea flubensces* ssp. *leucanta* and *Pinus halepensis* are the main species identified after the wildfire. *Quercus coccifera* is a woody phanerophytic species with vegetative propagation. Most of the area in the CFD plots was covered after the wildfire by species with different strategies of fire response, mainly seeding trees (*Cistus albidus, Fumana ericoides, Pinus halepensis*), but also sprouting (*Rhamnus lycioides, Pistacia lentiscus*) and facultative sprouting (*Anthillys cytisoides*) trees as well as facultative sprouting herbaceous species (*Brachypodium retusum*). Finally, also in LEB plots, we surveyed, after the wildfire, a variety of species with different response strategies to the fire. Woody seeding species prevail (*Fumana helicoide, Cistus albidus, Rosmariuns officinalis, Pinus halepensis, Atriplex halimus*), but also woody sprouting trees (*Rhamnus lycioides, Juniperus oxycedrus*), woody facultative sprouting (*Retama sphaerocarpa*), herbaceous facultative sprouting (*Brachypodium retusum, Macrochloa tenacissima* (L.) *Kunth*), and herbaceous seeding (*Asphodelus fistulosus*) species.

2.3. Data Collection and Processing

2.3.1. Field Survey of Vegetation Cover

Four years after the fire (in the summer of 2016), fifty 30 m × 30 m plots were established in the catchment area (Figure 2a,b) and installed in each of the four land conditions (7 plots in LEB, 7 in CFD, 25 in BNA, and 11 in UB). An additional twelve

10 m × 10 m plots were installed in the hillslope area (Figure 2c,d) for the same land conditions (3 plots in LEB, 3 in CFD, 3 in BNA, and 3 in UB), totaling 62 sample plots (Figure 2c,d). All the plots were separated 100 m from each other, to be considered as independent; moreover, the burned plots were exposed to similar fire severity. In each plot, three strips were selected (10 m long and 0.5 m wide for the 10 m × 10 m plots, and 30 m long and 0.5 m wide for the 30 m × 30 m plots), where the vegetation cover was measured in percentage. Along each strip, we identified the different species, and calculated the percent canopy cover by the line intercept method [46] as the sum of canopy distances by the strip length. The data were averaged in plot as the mean of the three strips [47,48].

2.3.2. Remote Sensing Surveys of Vegetation Cover

On the plots at the hillslope scale, in 2016, a scheduled drone flight was carried out. The UAV used was a quadcopter md4-1000 (Microdrones Inc., Kreuztal, Germany) with a RGB SONY ILCE-5100 digital camera (Sony Corporation, Tokyo, Japan) on board. The sensor of the SONY ILCE-5100 camera was a complementary metal oxide semiconductor (CMOS) Exmor® type APS-C (23.5 × 15.6 mm) with pixel size of 4 × 4 µm. The image size was 6000 × 4000 (columns and rows) and its focal length was 20 mm. Flight planning was performed for a flight altitude of 120 m obtaining a ground sample distance (GSD) of 0.015 m (Figure 4). LANDSAT8 images of the same date were collected over the plots at the catchment scale (Figure 4). *VARI* values were calculated using UAV and LANDSAT8 images, both from 2016. LANDSAT image was subjected to atmospheric correction and radiometric calibration [49] without using LEDAPS approach. *VARI* was calculated for each pixel, which identifies the vegetation in the part of the visible spectrum (ideal for RGB images). *VARI* is calculated as follows [24]:

$$VARI = \frac{Green - Red}{Green + Red - Blue} \quad (1)$$

Once calculated, *VARI* was then classified, splitting the entire range of data into five classes, to which a "rank" was given for both image sources (satellite and UAV) (Table 2). Then, possible correlations between the *VARI* values and the vegetation cover measured in the plots in 2016 at the two spatial scales were found. Using the *VARI* values, the effects of the land restoration measures on the vegetation cover in comparison with the burned and not treated, as well as to the unburned land, were evaluated.

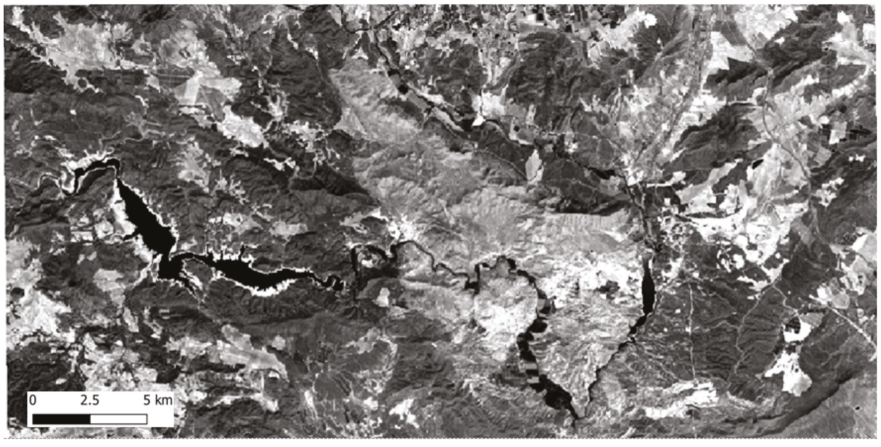

(**a**)

(**b**)

Figure 4. Examples of satellite (**a**) and drone (**b**) images caught in Serra de Los Donceles forest (Castilla-La Mancha, Spain).

Table 2. Calculation of the class width for the VARI classification in ranks in Sierra de Los Donceles forest (Castilla-La Mancha, Spain) (Source: our processing).

VARI	LANDSAT8	UAV
Minimum	−0.215	−0.599
Maximum	0.058	0.173
Range	0.273	0.771
Class width (range/5)	0.055	0.154

2.4. Spatial Analysis

Using QGIS software applied to a digital terrain model (DTM) prepared by the Spanish Center of Geographic Information in 2016 (resolution of 5 × 5 m), a spatial analysis was carried out to calculate the values of land slope and terrain roughness at the hillslope scale. As exposed by Wu et al. [50], terrain roughness is defined as the unevenness of the terrain surface (including rocks and low vegetation) at scales of several meters. This analysis was targeted to identify possible relationships between vegetation regeneration and land characteristics (that is, land slope and terrain roughness) for the different soil conditions. In order to analyze VARI index and its relationships with land slope and terrain roughness at the hillslope scale, a total of 100 plots were randomly selected on the DTM prepared by the Spanish Center of Geographic Information in 2016 (40 plots in LEB, 20 in CFD, 20 in BNA, 20 in UB.

2.5. Statistical Analysis

For both field measurements and remote sensing estimations, General Linear Models (GLM, using treatment as fixed factor and plot as random factor) was applied to evaluate the statistical significance of the differences in the vegetation cover or VARI among the treatments and the control areas. This statistical approach allows us to deal with pseudo-replication [51]. The homogeneity of the variance and the normality of the samples were checked using the Levene and Kolmogorov-Smirnov tests, respectively. All plots were considered spatially independent. The independent Fisher's least significant difference (LSD) test was used for post hoc comparisons. An α-level <0.05 was adopted. Finally, linear correlations were calculated between VARI and vegetation cover measured in field surveys on one side, as well as land slope and terrain roughness on the other side.

3. Results and Discussion

3.1. Field Measurements of Vegetation Cover in Different Land Conditions

All surveyed plant species of this study were typical of post-fire vegetation succession in the Mediterranean forest. These species are commonly found in open areas receiving high solar radiation and adapted to fire through different vegetative and reproductive mechanisms. In more detail, the floristic composition of the shrub and herbal layer in the surveyed area was not significantly altered by fire. In fact, the species that have repopulated the forest areas after fire belonged to the pre-existing populations. The number of species did not change, since after the fire, the species progressively regenerates, thanks to the adaption to new conditions of light, water and nutrients.

The vegetation cover measured in the plots under the four land conditions was more extensive in the areas treated with LEB (vegetal cover of $84.5 \pm 4.5\%$) compared to CFD plots ($76.9 \pm 5.6\%$). As expected, the extreme values were surveyed in UB (100%) and BNA ($65.5 \pm 4.2\%$) (Figure 5). These differences were significant after one-way ANOVA ($p < 0.05$), except for LEB treatment (not significantly different from UB and CFD). According to fieldwork and forest regional managers, this change is mainly due to shrub regeneration and growth. The Mediterranean vegetation is highly adapted to wildfires and these ecosystems are able to respond to fire using resprout or seeding mechanisms. That change is attributed to the higher biomass of the scrub and herbal layer. As recently stated by Keeley and Pausas [52], fire does not threaten ecosystem health, since it is a necessary process and a natural disturbance that is beneficial for the functionality of a fire-adapted ecosystem in Mediterranean forests. As demonstrated by our results, following fire disturbance, Mediterranean forests can regenerate from seed banks stored in soils and basal resprouts.

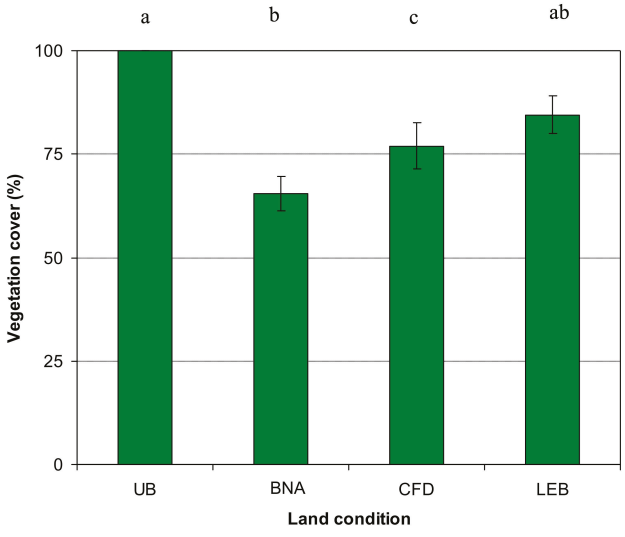

Figure 5. Vegetation cover (mean ± standard deviation of 62 plots) in plots under four land conditions (UB = unburned; BNA = burned and no action; CFD = contour-felled log debris; LEB = log erosion barriers) after the wildfire of 2012 in Sierra de Los Donceles forest (Castilla-La Mancha, Spain). Mean values that do not share a lower case letter (top of graph) are significantly different from each other (HSD, $p < 0.05$).

This means that, four years after the wildfire, the vegetation regeneration is far from covering the entire area, such as in the unburned zone. The implementation of post-fire treatments allows for a significantly faster recovery process, and LEBs are particularly effective. This higher regeneration compared to CFD-treated areas is somewhat expected, since the dead and burned material of which CFDs consist of is degrading, as well as incorporated more easily compared to the burned wood of LEBs [53]. Both post-fire management techniques are recognized to reduce runoff and erosion (by slowing flows of water and sediments) [14] and improve the physico-chemical properties of soils (increasing infiltration and water retention, and organic matter and nutrients), thus enhancing establishment and development of vegetation [12]. Some LEBs can trap up to 40% of sediments; moreover, this treatment is cheaper compared to other hillslope stabilization techniques [54]. CFDs are effective to reduce water and sediment flows in burned forest subject to machinery salvage logging [55]. Moreover, according to Badía et al. [13], hillslope stabilization after wildfire is a physical barrier that avoids losses or reductions in soil organic matter and nutrients. At the same time, logs of CFDs and canopy residues of LEBs can change the microclimate and land conditions, as well as represent organic matter source after decomposition. This enhances the biological activity of soils [18]. Moreover, decreased evaporation, higher soil moisture, and soil organic matter accumulation upslope of LEB and CFD might lead to an increase in soil respiration and microbial activity, also enhancing nutrient availability after a burn at 5 years from the wildfire). Regarding other studies evaluating post-fire regeneration of vegetation, Christakopoulos et al. [40] found that reforestation was, in some cases, comparable, and in other areas, higher, compared to natural regeneration of pines in burned forests of Greece.

3.2. Correlations of VARI with Vegetation Cover Using Remote Sensing Techniques

Figure 6a,b reports the maps of VARI distribution in the experimental areas at both catchment and hillslope scales. In particular, Figure 6b highlights that VARI is higher in the areas subjected to post-fire treatments and lower in burned and untreated land.

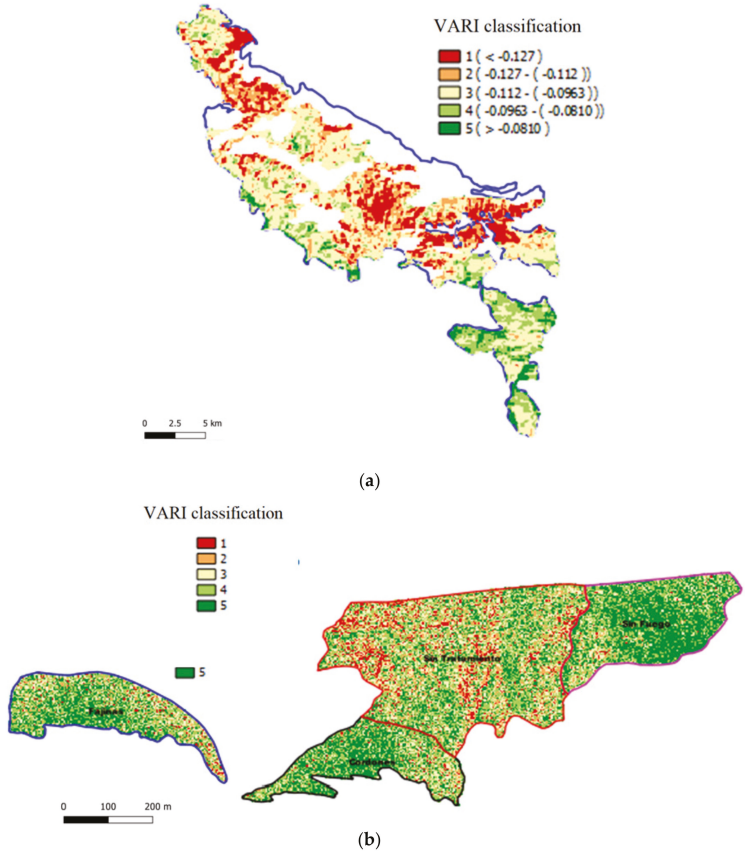

Figure 6. Spatial distribution of VARI surveyed by satellite (**a**) and UAV (**b**) images of 2016 among four land conditions after the wildfire of 2012 in Sierra de Los Donceles forest (Castilla-La Mancha, Spain). Legend: Fajinas = log erosion barriers; cordones = contour-felled log debris; sin tratamiento = burned and no Action; sin fuego = unburned.

A low and not significant R^2 (0.03, $p > 0.05$) was found regressing the LANDSAT8-derived VARI with the vegetation cover measured in field (Figure 7a, catchment scale), while the regression of UAV-derived VARI versus vegetation cover was significant ($R^2 = 0.84$, $p < 0.05$) (Figure 7b, hillslope scale). This difference is clearly due to the lower spatial resolution of satellite data compared to surveys by UAV.

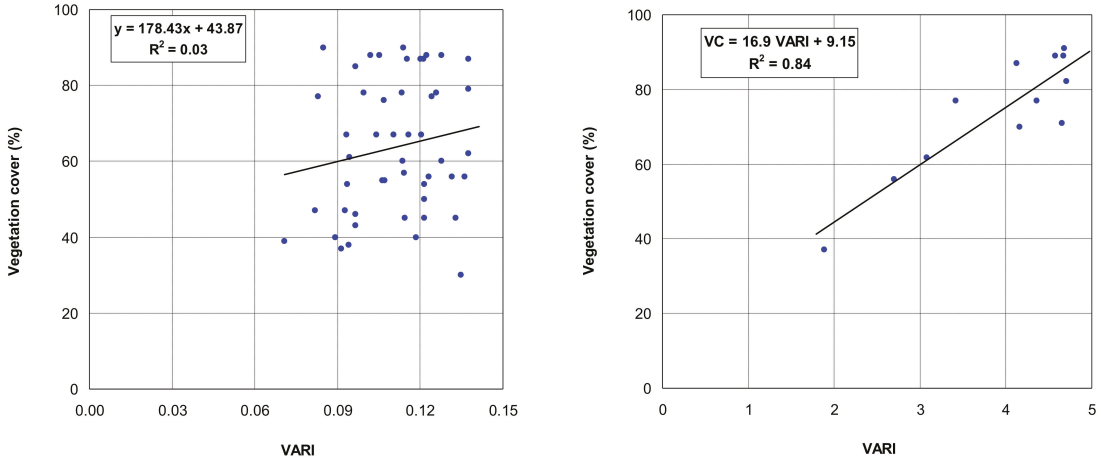

Figure 7. Correlations between VARI and vegetation cover at catchment (**a**), and hillslope (**b**) scales surveyed by LANDSAT8 and UAV images (2016) in Sierra de Los Donceles forest (Castilla-La Mancha, Spain).

The regression equations for the correlation VARI versus vegetal cover (VC) measured in field was the following:

$$VC = 16.90\ VARI + 9.15 \quad (2)$$

The vegetation cover distribution in classes according to the VARI classification by UAV is reported in Table 2 and confirms the spatial differences among the land conditions. By visually comparing the vegetation cover distribution according to the two VARI classifications (satellite and UAV, Table 2), no overlay among the same class was detected. This lack of correspondence further confirms the higher reliability of VARI estimated from UAVs to reproduce land cover compared to estimations by satellite, due to unsuitability of image resolution.

The use of VARI to evaluate vegetation regeneration from UAVs has been widely studied in literature. To cite the most recent studies, VARI was used to analyze vegetation on different land uses (e.g., [36–39,56]), monitoring vegetation into water bodies (e.g., [57], and preparation of the Digital Elevation Model (DEM) [58]). This index shows significant correlation with crop height and yield [59,60]. In burned lands, Larrinaga and Brotons [39] calculated VARI for analysis of post fire regeneration of Mediterranean forests. However, these authors reported that this index underperformed compared to other greenness indexes, such as the Excess green index (ExGI) and green chromatic coordinate (GCC) index, and the same was found for the green red vegetation index (GRVI). Despite this, these authors have demonstrated that low-cost UAVs may improve forest monitoring after disturbance, even in those habitats and situations where resource limitation is an issue. In general, VARI shows a minimal sensitivity to atmospheric effects [26,61,62].

3.3. Evaluation of the Vegetation Regeneration in Fire-Affected and Treated Areas Using VARI

The comparison of the mean VARI values under the four studied land conditions between the two remote images shows that, at the catchment scale, VARI was higher (0.009 ± 0.046) under CFDs and lower (-0.034 ± 0.035) in UB areas. This appears again unrealistic, further confirming the misleading meaning of land cover images captured by UAV. Moreover, the differences among the four land conditions were not significant ($p = 0.724$) (Figure 8a).

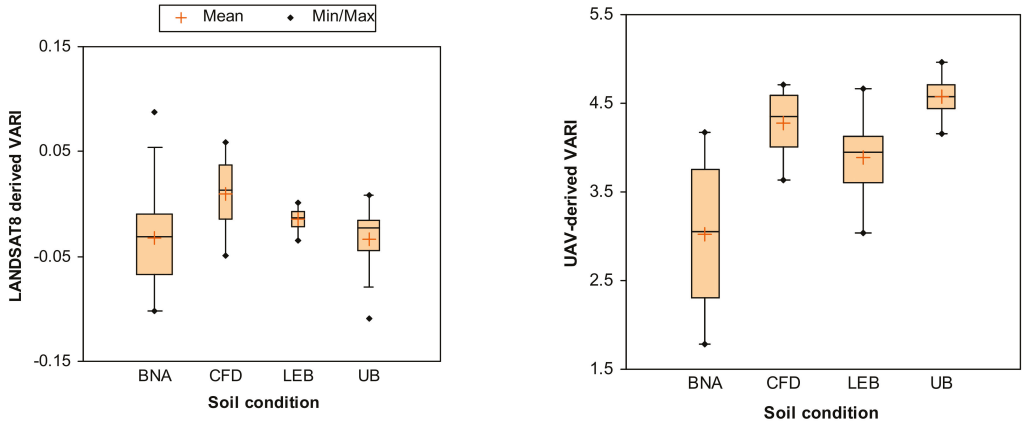

(**a**) (**b**)

Figure 8. Mean values of VARI surveyed by LANDSAT8 (**a**) and UAV (**b**) images (2016) among four land conditions after the wildfire of 2012 in Sierra de Los Donceles forest (Castilla-La Mancha, Spain).

In contrast, when analyzing the images by UAV, the highest VARI (4.578 ± 0.230) was found in the UB areas (indicating the most extensive vegetation cover), while the lowest value was detected in the areas burned but not treated (VARI of 3.024 ± 0.853). However, in contrast with field surveys, vegetation regeneration was higher in the land treated with CFDs (mean VARI of 4.270 ± 0.350) compared to the areas with LEBs (3.889 ± 0.416) (Figure 8b). As for field surveys, the differences in VARI were significant ($p < 0.05$) at this smaller scale using the UAV. Lack of correspondence between the post-fire land treatments suggests that UAV is a viable technique in detecting the variability of vegetation cover only when the difference in VARI mean values is noticeable (e.g., between burned and unburned areas); conversely, the contrasts between areas with similar VARIs may be quite misleading, for instance, when the effectiveness of a treatment has to be evaluated. This result is in close accordance with the indications by Corona et al. [63], who suggested the use of aerial and satellite imagery characterized by high or, better, very high spatial resolution for an effective support to post-fire management (burned area mapping, fire severity assessment, post-fire vegetation monitoring).

Comparisons to other published data about evaluations of post-fire vegetation recovery using remote sensing and greenness indices reveal that SAR images perform better compared to optical images in estimating forest regeneration, particularly when object-based classification procedure is applied (nearly 90% of accuracy) [34]. Moreover, Lasaponara et al. [33] found a better reliability of NDVI (Normalized Difference Vegetation Index) in capturing the diverse vegetation regeneration in both natural and managed areas as well as before and after fire occurrence compared to NBR index, thanks to the data processing using detrended fluctuation analysis (DFA). LANDSAT time series analysis with NBR application was a useful means of describing and analyzing post-fire vegetation recovery across mixed-severity wildfire extents [30], while, in contrast, Lentile et al. [31] reported that dNBR is an imperfect indicator of post-fire effects on vegetation and soil, when the burned areas are affected by different burn severities and are of a highly variable patch size. Regarding the use of drone images, Fernández-Guisuraga et al. [64] highlighted the more detailed spatial information provided by the drone orthomosaic compared to WorldView-2 satellite imagery in vegetation regeneration of heterogeneous burned areas.

Overall, the use of UAV systems for vegetation recovery monitoring is still under development, since these systems have a great potential not yet fully valorized; however,

this use is still limited by some constraints, such as battery life and availability of cameras with suitable spectral range, as well as cost [22].

3.4. Spatial Distribution of Land Slope and Roughness, and Correlations with VARI

The spatial analysis carried out in the experimental areas showed that the slope of land subjected to post-fire treatments was significantly different (32.2 ± 5.26% for LEB and 36.2 ± 2.61% for CFD) compared to the BNA (23.1 ± 6.22%), but similar to the UB land (36.6 ± 3.71%) (Table 3 and Figure 9a). This may be due to the fact that landscape managers prioritized steeper areas when post-fire treatments were planned, since the zones with higher slopes are more prone to erosion and hydrogeological risks compared to flat areas.

Table 3. Values (mean ± standard deviation) of land slope and terrain roughness in the small-scale areas under four land conditions in Sierra de los Donceles forest (Castilla-La Mancha, Spain).

Treatment	Land Slope (%)	Terrain Roughness (μm)
LEB	32.2 ± 5.26 a	0.08 ± 0.03 a
CFD	36.2 ± 2.61 a	0.09 ± 0.01 a
BNA	23.1 ± 6.22 b	0.06 ± 0.03 a
UB	36.6 ± 3.71 a	0.28 ± 0.21 b

Notes: UB = unburned; BNA = burned and no action; CFD = contour-felled log debris; LEB = log erosion barriers; different lower case letters indicate significant differences (HSD, $p < 0.05$).

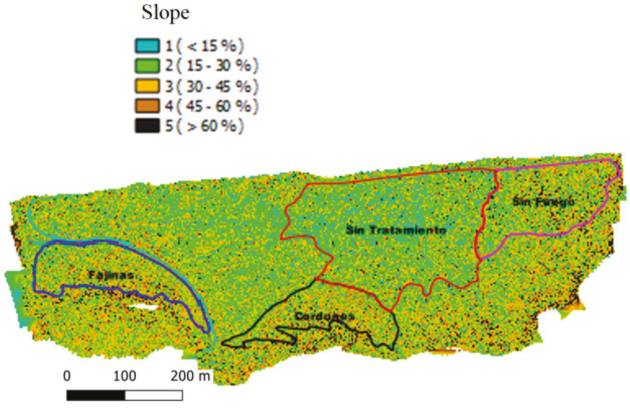

(**a**)

Figure 9. *Cont.*

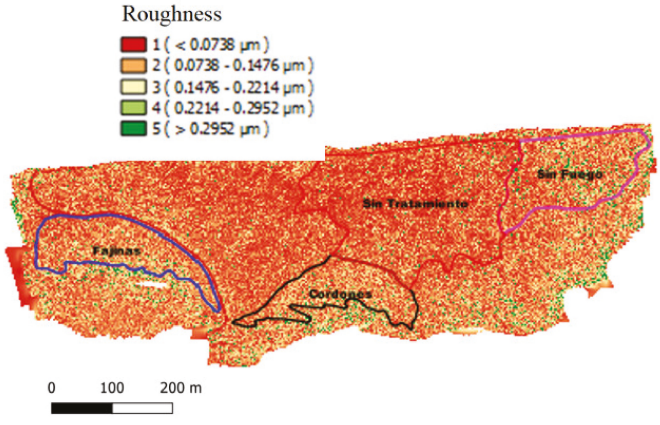

(**b**)

Figure 9. Spatial distribution of land slope (**a**) and terrain roughness (**b**) surveyed by UAV images of 2016 among four land conditions after the wildfire of 2012 in Sierra de Los Donceles forest (Castilla-La Mancha, Spain). Legend: Fajinas = log erosion barriers; cordones = contour-felled log debris; sin tratamiento = burned and no action; sin fuego = unburned.

According to the land map of Figure 9b prepared using spatial analysis, the terrain roughness of the burned areas was significantly different (0.08 ± 0.03 µm for LEB, 0.09 ± 0.01 µm for CFD, and 0.06 ± 0.03 µm for BNA) compared to UB zone (0.28 ± 0.21 µm) (Table 2). This means that the vegetation growing in the burned and treated zone do not have a significant effect on the terrain roughness compared to the area without treatment, and that these values are well below the roughness of the unburned soil. A high terrain roughness is beneficial to reduce surface runoff and thus, sediment transport downstream [65–67]. Soil preparation (e.g., by tillage, conditioning, and terracing) after wildfire may be suggested, in order to enhance vegetation growth and improve the soil's resistance to erosion [68–71].

A fair and significant linear correlation was found regressing VARI on land slope under all soil conditions ($r^2 = 0.52$, $p < 0.05$) (Figure 10a), while the linear regression between VARI and terrain roughness was much lower ($r^2 = 0.15$) and not significant ($p = 0.49$) (Figure 10b). This correlation becomes significant ($p < 0.05$) although, again, low ($r^2 = 0.35$ to 0.38), adopting exponential or logarithmic equations, whose physical meaning is, however, difficult to be justified (data not shown).

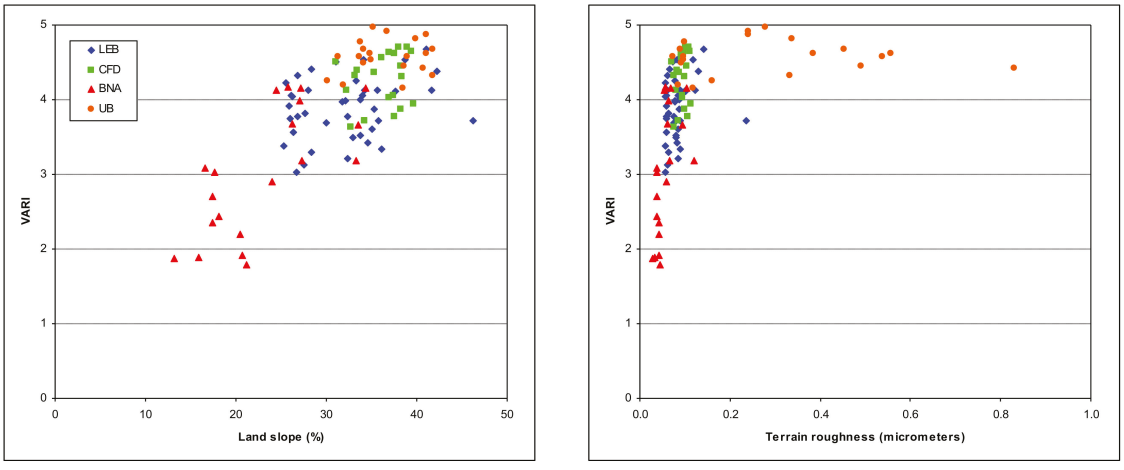

(**a**) (**b**)

Figure 10. Scatterplots of vegetation regeneration (measured by VARI by UAV images of 2016) versus land slope (**a**) and terrain roughness (**b**) among four land conditions after the wildfire of 2012 in Sierra de Los Donceles forest (Castilla-La Mancha, Spain).

The first correlation suggests that the effectiveness of post-fire treatments on vegetation regeneration (measured using VARI) increased with slope, and thus, the strategy of landscape managers that have prioritized steeper slopes for treatments was successful. By contrast, the lower, or absence of, significance of correlations between VARI and terrain roughness implies that vegetation growth, at least in the experimental conditions, played a limited influence on soil surface conditions. However, vegetation regeneration remains a key factor to reduce soil exposure to erosion in wildfire-affected areas.

4. Conclusions

The surveys of vegetation cover using fieldwork and remote sensing in lands burned by wildfire in a Mediterranean forest showed that:

- Post-fire treatments improve the vegetation regeneration compared to the burned and not treated areas (by about 20% for CFDs and 30% for LEBs); in this sense, the post-fire treatment using LEBs appears to be more promising compared to the CFD technique;
- Surveys by UAV are useful to detect the variability of vegetation cover among burned and unburned areas through VARI, but may be unrealistic when the effectiveness of a post-fire treatment must be evaluated;
- LANDSAT8 images are less reliable to evaluate the land cover post-fire treatments, due to the lack of correlation between VARI and vegetation cover, and may be because of the resolution that is not suitable for small plants.

The spatial analysis of distribution of VARI and land characteristics at the hillslope scale proved that:

- The post-fire restoration strategy of landscape managers that have prioritized steeper slopes for treatments was successful;
- Vegetation growth, at least in the experimental conditions, played a limited influence on soil surface conditions, since no significant increases in terrain roughness were detected in treated areas.

However, the validity of these preliminary results must be confirmed in other experimental conditions, such as in areas with different climate and soil conditions, as well as in soils subjected to other post-fire management techniques. The effects of patch vegetation should be also explored, since a high spatial variability of vegetation may not be fully cap-

tured by aerial or satellite images. Additionally, the implementation of UAV-based surveys throughout the different stages of vegetation regeneration after wildfire can be suggested, in order to develop a viable tool for monitoring the effectiveness of post-fire techniques over time. A wider validation activity should ensure a practical use of UAV images to support the activity of land managers in planning and implementing efficient measures to restore wildfire-affected areas using vegetation cover. The research question about the viability of higher-resolution satellite images to detect contrasts in vegetation cover among different land conditions remains open. Presumably, the integration of several techniques, combining advantages and limiting constraints, can be suggested for estimation of post-fire vegetation recovery in forest ecosystems with dynamically variable characteristics.

Author Contributions: Conceptualization, M.E.L.-B. and P.A.P.-A.; methodology, M.E.L.-B., M.A.M., D.H., J.G.-R., D.A.Z., and P.A.P.-A.; formal analysis, J.L.M. and P.D.; writing—original draft preparation, J.L.M., M.E.L.-B., P.A.P.-A., P.D., M.A.M., D.H., J.G.-R., and D.A.Z. All authors have read and agreed to the published version of the manuscript.

Funding: This research received no external funding.

Data Availability Statement: The data presented in this study are available on request from the corresponding author.

Conflicts of Interest: The authors declare no conflict of interest.

References

1. Stephens, S.L.; Boerner, R.E.; Moghaddas, J.J.; Moghaddas, E.E.; Collins, B.M.; Dow, C.B.; Youngblood, A. Fuel treatment impacts on estimated wildfire carbon loss from forests in Montana, Oregon, California, and Arizona. *Ecosphere* **2012**, *3*, 1–17. [CrossRef]
2. Pereira, P.; Francos, M.; Brevik, E.C.; Ubeda, X.; Bogunovic, I. Post-fire soil management. *Curr. Opin. Environ. Sci. Health* **2018**, *5*, 26–32. [CrossRef]
3. Girardin, M.P.; Ali, A.A.; Carcaillet, C.; Gautgier, S.; Hély, C.; Le Goff, H.; Terrier, A.; Bergeron, Y. Fire in managed forest of eastern Canada: Risk and options. *For. Ecol. Manag.* **2013**, *294*, 238–249. [CrossRef]
4. Versini, P.A.; Velasco, M.; Cabello, A.; Sempere-Torres, D. Hydrological impact of forest fires and climate change in Mediterranean basin. *Nat. Hazards* **2013**, *66*, 609–628. [CrossRef]
5. MAPA. *Spain Los Incendios Forestales en España. 1 Enero–31 Diciembre 2018*; Avance Informativo Ministerio de Agricultura, Pesca y Alimentación, Gobierno de España: Madrid, Spain, 2019.
6. Lachowski, H.; Hardwick, P.; Griffith, R.; Parsons, A.; Warbington, R. Faster, better data for burned watersheds needing emergency rehab. *J. For.* **1997**, *95*, 4–8.
7. Moody, J.A.; Shakesby, R.A.; Robichaud, P.R.; Cannon, S.H.; Martin, D.A. Current research issues related to post-wildfire runoff and erosion processes. *Earth Sci. Rev.* **2013**, *122*, 10–37. [CrossRef]
8. Zema, D.A.; Nunes, J.P.; Lucas-Borja, M.E. Improvement of seasonal runoff and soil loss predictions by the MMF (Morgan-Morgan-Finney) model after wildfire and soil treatment in Mediterranean forest ecosystems. *Catena* **2020**, *188*, 104415. [CrossRef]
9. Ryu, S.R.; Choi, H.T.; Lim, J.H.; Lee, I.K.; Ahn, Y.S. Post-fire restoration plan for sustainable forest management in South Korea. *Forests* **2017**, *8*, 188. [CrossRef]
10. Viana-Soto, A.; Aguado, I.; Martínez, S. Assessment of post-fire vegetation recovery using fire severity and geographical data in the mediterranean region (Spain). *Environments* **2017**, *4*, 90. [CrossRef]
11. Robichaud, P.R.; Wagenbrenner, J.W.; Brown, R.E.; Wohlgemuth, P.M.; Beyers, J.L. Evaluating the effectiveness of contour-felled log erosion barriers as a post-fire runoff and erosion mitigation treatment in the western United States. *Int. J. Wildland Fire* **2008**, *17*, 255–273. [CrossRef]
12. Fernández, C.; Fontúrbel, T.; Vega, J.A. Effects of pre-fire site preparation and post-fire erosion barriers on soil erosion after a wildfire in NW Spain. *Catena* **2019**, *172*, 691–698. [CrossRef]
13. Badía, D.; Sánchez, C.; Aznar, J.M.; Martí, C. Post-fire hillslope log debris dams for runoff and erosion mitigation in the semiarid Ebro Basin. *Geoderma* **2015**, *237*, 298–307. [CrossRef]
14. Wittenberg, L.; van der Wal, H.; Keesstra, S.; Tessler, N. Post-fire management treatment effects on soil properties and burned area restoration in a wildland-urban interface, Haifa Fire case study. *Sci. Total. Environ.* **2020**, *716*, 135190. [CrossRef]
15. Niemeyer, R.J.; Bladon, K.D.; Woodsmith, R.D. Long-term hydrologic recovery after wildfire and post-fire forest management in the interior Pacific Northwest. *Hydrol. Process.* **2020**, *34*, 1182–1197. [CrossRef]
16. Keith, H.; Lindenmayer, D.; Mackey, B.; Blair, D.; Carter, L.; McBurney, L.; Konishi-Nagano, T. Managing temperate forests for carbon storage: Impacts of logging versus forest protection on carbon stocks. *Ecosphere* **2014**, *5*, 1–34. [CrossRef]
17. Raftoyannis, Y.; Spanos, I. Evaluation of log and branch barriers as post-fire rehabilitation treatments in a Mediterranean pine forest in Greece. *Int. J. Wildland Fire* **2005**, *14*, 183–188.

18. Robichaud, P.R. Fire effects on infiltration rates after prescribed fire in Northern Rocky Mountain forests, USA. *J. Hydrol.* **2000**, *231*, 220–229. [CrossRef]
19. Leverkus, A.B.; Rey Benayas, J.M.; Castro, J.; Boucher, D.; Brewer, S.; Collins, B.M.; Lee, E.-J. Salvage logging effects on regulating and supporting ecosystem services—A systematic map. *Can. J. For. Res.* **2018**, *48*, 983–1000. [CrossRef]
20. Lindenmayer, D.B.; Noss, R.F. Salvage logging, ecosystem processes, and biodiversity conservation. *Conserv. Biol.* **2006**, *20*, 949–958. [CrossRef] [PubMed]
21. Fox, D.M.; Maselli, F.; Carrega, P. Using SPOT images and field sampling for mapping burn severity and vegetation factors affecting post fire erosion risk. *Catena* **2008**, *75*, 326–335. [CrossRef]
22. Szpakowski, D.M.; Jensen, J.L. A review of the applications of remote sensing in fire ecology. *Remote. Sens.* **2019**, *11*, 2638. [CrossRef]
23. Alfonso-Torreño, A.; Gómez-Gutiérrez, Á.; Schnabel, S.; Contador, J.F.L.; de Sanjosé Blasco, J.J.; Fernández, M.S. sUAS, SfM-MVS photogrammetry and a topographic algorithm method to quantify the volume of sediments retained in check-dams. *Sci. Total. Environ.* **2019**, *678*, 369–382. [CrossRef] [PubMed]
24. Gitelson, A.A.; Stark, R.; Grits, U.; Rundquist, D.; Kaufman, Y.; Derry, D. Vegetation and soil lines in visible spectral space: A concept and technique for remote estimation of vegetation fraction. *Int. J. Remote. Sens.* **2002**, *23*, 2537–2562. [CrossRef]
25. Gitas, I.; Mitri, G.; Veraverbeke, S.; Polychronaki, A. Advances in remote sensing of post-fire vegetation recovery monitoring—A review. *Remote Sens. Biomass Princ. Appl.* **2012**, *1*, 334.
26. Bhagat, V.S.; Kadam, A.; Kumar, S. Analysis of Remote Sensing based Vegetation Indices (VIs) for Unmanned Aerial System (UAS): A Review. *Remote Sens. Land* **2019**, *3*, 58–73. [CrossRef]
27. Evangelides, C.; Nobajas, A. Red-Edge Normalised Difference Vegetation Index (NDVI705) from Sentinel-2 imagery to assess post-fire regeneration. *Remote Sens. Appl. Soc. Environ.* **2020**, *17*, 100283. [CrossRef]
28. Xue, J.; Su, B. Significant remote sensing vegetation indices: A review of developments and applications. *J. Sens.* **2017**, 1353691. [CrossRef]
29. Sirin, A.; Medvedeva, M.; Maslov, A.; Vozbrannaya, A. Assessing the Land and Vegetation Cover of Abandoned Fire Hazardous and Rewetted Peatlands: Comparing Different Multispectral Satellite Data. *Land* **2018**, *7*, 71. [CrossRef]
30. Bright, B.C.; Hudak, A.T.; Kennedy, R.E.; Braaten, J.D.; Khalyani, A.H. Examining post-fire vegetation recovery with Landsat time series analysis in three western North American forest types. *Fire Ecol.* **2019**, *15*, 1–14. [CrossRef]
31. Lentile, L.B.; Morgan, P.; Hudak, A.T.; Bobbitt, M.J.; Lewis, S.A.; Smith, A.M.; Robichaud, P.R. Post-fire burn severity and vegetation response following eight large wildfires across the western United States. *Fire Ecol.* **2007**, *3*, 91–108. [CrossRef]
32. Bastos, A.; Gouveia, C.; DaCamara, C.; Trigo, R. Landscape, fire distribution and vegetation recovery in Portugal: 2003 and 2005 fire seasons. In *Advances in Remote Sensing and GIS Applications in Forest Fire Management: From Local to Global Assessments*; EUR 24941 EN; Miguel-Ayanz, J., Camia, A., Gitas, I., Santos De Oliveira, S., Eds.; Publications Office of the European Union: Luxembourg, 2011; JRC66634.
33. Lasaponara, R.; Montesano, T.; Desantis, F.; Lanorte, A. Evaluating post fire vegetation recovery using satellite MODIS data. In *Advances in Remote Sensing and GIS Applications in Forest Fire Management: From Local to Global Assessments*; EUR 24941 EN; Miguel-Ayanz, J., Camia, A., Gitas, I., Santos De Oliveira, S., Eds.; Publications Office of the European Union: Luxembourg, 2011; JRC66634.
34. Polychronaki, A.I.; Gitas, I.Z.; Minchella, A. Monitoring post-fire vegetation recovery using optical and sar data. In *Advances in Remote Sensing and GIS Applications in Forest Fire Management: From Local to Global Assessments*; EUR 24941 EN; Miguel-Ayanz, J., Camia, A., Gitas, I., Santos De Oliveira, S., Eds.; Publications Office of the European Union: Luxembourg, 2011; JRC66634.
35. San-Miguel-Ayanz, J.; Camia, A.; Gitas, I.; Santos De Oliveira, S. (Eds.) *Advances in Remote Sensing and GIS Applications in Forest Fire Management: From Local to Global Assessments*; EUR 24941 EN; Publications Office of the European Union: Luxembourg, 2011; JRC66634.
36. Schneider, P.; Roberts, D.A.; Kyriakidis, P.C. A VARI-based relative greenness from MODIS data for computing the Fire Potential Index. *Remote. Sens. Environ.* **2008**, *112*, 1151–1167. [CrossRef]
37. Stow, D.; Niphadkar, M.; Kaiser, J. MODIS-derived visible atmospherically resistant index for monitoring chaparral moisture content. *Int. J. Remote. Sens.* **2005**, *26*, 3867–3873. [CrossRef]
38. Jiménez-Muñoz, J.C.; Sobrino, J.A.; Plaza, A.; Guanter, L.; Moreno, J.; Martínez, P. Comparison between fractional vegetation cover retrievals from vegetation indices and spectral mixture analysis: Case study of PROBA/CHRIS data over an agricultural area. *Sensors* **2009**, *9*, 768–793. [CrossRef]
39. Larrinaga, A.R.; Brotons, L. Greenness indices from a low-cost UAV Imagery as tools for monitoring post-fire forest recovery. *Drones* **2019**, *3*, 6. [CrossRef]
40. Christakopoulos, P.; Paronis, D.; Scarvelis, M.; Kalabokides, K.; Hatzopoulos, I. Comparative evaluation of restoration practices applied to mediterranean forest ecosystems using remote sensing and GIS: Natural regeneration versus reforestation. In *Advances in Remote Sensing and GIS Applications in Forest Fire Management: From Local to Global Assessments*; EUR 24941 EN; Miguel-Ayanz, J., Camia, A., Gitas, I., Santos De Oliveira, S., Eds.; Publications Office of the European Union: Luxembourg, 2011; JRC66634.
41. Rivas-Martínez, S.; Rivas-Saenz, S.; Penas, A. *Worldwide Bioclimatic Classification System*; Backhuys Pub: Leiden, The Netherlands, 2002.

42. State Meteorological Agency-AEMET-Spanish Government. Available online: http://www.aemet.es/es/portada (accessed on 12 January 2021).
43. IGN. *Mapa de Suelos de España*; Instituto Geográfico Nacional: Madrid, Spain, 2006.
44. Soil Survey Staff. *Keys to Soil Taxonomy*; Natural Resources Conservation Service—Department of Agriculture: Washington, DC, USA, 2014.
45. Napper, C. *Burned Area Emergency Response Treatments Catalog*; National Technology & Development Program, Watershed, Soil Air Management 0625 1801-SDTDC; USDA Forest Service: San Dimas, CA, USA, 2006.
46. Canfield, R. Application of Line Interception Method in Sampling Range Vegetation. *J. For.* **1941**, *39*, 388–394.
47. Zema, D.A.; Plaza-Alvarez, P.A.; Xu, X.; Carra, B.G.; Lucas-Borja, M.E. Influence of forest stand age on soil water repellency and hydraulic conductivity in the Mediterranean environment. *Sci. Total. Environ.* **2020**, *753*, 142006. [CrossRef]
48. Zema, D.A.; Van Stan, J.T.; Plaza-Alvarez, P.A.; Xu, X.; Carra, B.G.; Lucas-Borja, M.E. Effects of stand composition and soil properties on water repellency and hydraulic conductivity in Mediterranean forests. *Ecohydrology* **2021**, *14*, e2276. [CrossRef]
49. Millar, R.B.; Anderson, M.J. Remedies for pseudoreplication. *Fish. Res.* **2004**, *70*, 397–407. [CrossRef]
50. Wu, J.; Yang, Q.; Li, Y. Partitioning of Terrain Features Based on Roughness. *Remote Sens.* **2018**, *10*, 1985. [CrossRef]
51. Halthore, R.N.; Markham, B.L. Overview of atmospheric correction and radiometric calibration efforts during FIFE. *J. Geophys. Res. Atmos.* **1992**, *97*, 18731–18742. [CrossRef]
52. Keeley, J.E.; Pausas, J.G. Distinguishing disturbance from perturbations in fire-prone ecosystems. *Int. J. Wildland Fire* **2019**, *28*, 282–287. [CrossRef]
53. Gómez-Sanchez, E.; Lucas-Borja, M.E.; Plaza-Alvarez, P.A.; González-Romero, J.; Sagra, J.; Moya, D.; De las Heras, J. Effects of postfire hillslope stabilisation techniques on chemical, physico-chemical and microbiological soil properties in Mediterranean forest ecosystems. *J. Environ. Manag.* **2019**, *246*, 229–238. [CrossRef] [PubMed]
54. Albert-Belda, E.; Bermejo-Fernández, A.; Cerdà, A.; Taguas, E.V. The use of Easy-Barriers to control soil and water losses in fire-affected land in Quesada, Andalusia, Spain. *Sci. Total. Environ.* **2019**, *690*, 480–491. [CrossRef] [PubMed]
55. Jourgholami, M.; Ahmadi, M.; Tavankar, F.; Picchio, R. Effectiveness of Three Post-Harvest Rehabilitation Treatments for Runoff and Sediment Reduction on Skid Trails in the Hyrcanian Forests. *Croat. J. For. Eng. J. Theory Appl. For. Eng.* **2020**, *41*, 1–16. [CrossRef]
56. Eng, L.S.; Ismai, R.; Hashim, W.; Mohamed, R.R.; Baharum, A. Vegetation monitoring using UAV: A preliminary Study. *Int. J. Eng. Technol.* **2018**, *7*, 223–227. [CrossRef]
57. Cermakova, I.; Komarkova, J.; Sedlak, P. Calculation of visible spectral indices from UAV-based data: Small water bodies monitoring. In Proceedings of the 14th Iberian Conference on Information Systems and Technologies (CISTI), Coimbra, Portugal, 19–22 June 2019; pp. 1–5.
58. Themistocleous, K. DEM Modeling using RGB-based vegetation indices from UAV images. *Proc. SPIE* **2019**, 11174. [CrossRef]
59. Fathipoor, H.; Arefi, H.; Shah-Hosseini, R.; Moghadam, H. Corn forage yield prediction using unmanned aerial vehicle images at mid-season growth stage. *J. Appl. Remote Sens.* **2019**, *13*, 034503. [CrossRef]
60. Wan, L.; Li, Y.; Cen, H.; Zhu, J.; Yin, W.; Wu, W.; Zhu, H.; Sun, D.; Zhou, W.; He, Y. Combining UAV-based vegetation indices and image classification to estimate flower number in oilseed rape. *Remote Sens.* **2018**, *10*, 1484. [CrossRef]
61. Mokarram, M.; Boloorani, A.D.; Hojati, M. Relationship between Land Cover and Vegetation Indices. Case Study: Eghlid Plain, Fars Province, Iran. *Eur. J. Geogr.* **2016**, *7*, 48–60.
62. Mokarram, M.; Hojjati, M.; Roshan, G.; Negahban, S. Modeling the Behavior of Vegetation Indices in the Salt Dome of Korsia in North-East of Darab, Fars, Iran. *Modeling Earth Syst. Environ.* **2015**, *1*, 1–9. [CrossRef]
63. Corona, P.; Lamonaca, A.; Chirici, G. Remote sensing support for post fire forest management. *Ifor. Biogeosci. For.* **2008**, *1*, 6. [CrossRef]
64. Fernández-Guisuraga, J.M.; Sanz-Ablanedo, E.; Suárez-Seoane, S.; Calvo, L. Using unmanned aerial vehicles in postfire vegetation survey campaigns through large and heterogeneous areas: Opportunities and challenges. *Sensors* **2018**, *18*, 586. [CrossRef] [PubMed]
65. Hou, T.; Filley, T.R.; Tong, Y.; Abban, B.; Singh, S.; Papanicolaou, A.T.; Wacha, K.M.; Wilson, C.G.; Chaubey, I. Tillage-induced surface soil roughness controls the chemistry and physics of eroded particles at early erosion stage. *Soil Tillage Res.* **2021**, *207*, 104807. [CrossRef]
66. Römkens, M.J.; Helming, K.; Prasad, S.N. Soil erosion under different rainfall intensities, surface roughness, and soil water regimes. *Catena* **2002**, *46*, 103–123. [CrossRef]
67. Govers, G.; Takken, I.; Helming, K. Soil roughness and overland flow. *Agronomie* **2000**, *20*, 131–146. [CrossRef]
68. De Almeida, W.S.; Panachuki, E.; de Oliveira, P.T.S.; da Silva Menezes, R.; Sobrinho, T.A.; de Carvalho, D.F. Effect of soil tillage and vegetal cover on soil water infiltration. *Soil Tillage Res.* **2018**, *175*, 130–138. [CrossRef]
69. Nunes, J.P.; Bernard-Jannin, L.; Rodriguez Blanco, M.L.; Santos, J.M.; Coelho, C.D.O.A.; Keizer, J.J. Hydrological and erosion processes in terraced fields: Observations from a humid Mediterranean region in northern Portugal. *Land Degrad. Dev.* **2018**, *29*, 596–606. [CrossRef]
70. Meena, R.S.; Lal, R.; Yadav, G.S. Long-term impacts of topsoil depth and amendments on soil physical and hydrological properties of an Alfisol in central Ohio, USA. *Geoderma* **2020**, *363*, 114164. [CrossRef]
71. Zema, D.A. Post-fire management impacts on soil hydrology. *Curr. Opin. Environ. Sci. Health* **2021**, *21*, 100252. [CrossRef]

applied sciences

MDPI

Article

Superpixel-Based Singular Spectrum Analysis for Effective Spatial-Spectral Feature Extraction

Subhashree Subudhi [1], Ramnarayan Patro [1], Pradyut Kumar Biswal [1,*] and Fabio Dell'Acqua [2]

[1] Department of Electronics and Communication Engineering, IIIT, Bhubaneswar 751003, India; C116013@iiit-bh.ac.in (S.S.); C116009@iiit-bh.ac.in (R.P.)
[2] Department of Electrical, Computer and Biomedical Engineering, University of Pavia, 27100 Pavia, Italy; fabio.dellacqua@unipv.it
* Correspondence: pradyut@iiit-bh.ac.in

Abstract: In the processing of remotely sensed data, classification may be preceded by feature extraction, which helps in making the most informative parts of the data emerge. Effective feature extraction may boost the efficiency and accuracy of the following classification, and hence various methods have been proposed to perform it. Recently, Singular Spectrum Analysis (SSA) and its 2-D variation (2D-SSA) have emerged as popular, cutting-edge technologies for effective feature extraction in Hyperspectral Images (HSI). Using 2D-SSA, each band image of an HSI is initially decomposed into various components, and then the image is reconstructed using the most significant eigen-tuples relative to their eigen-values, which represent strong spatial features for the classification task. However, instead of performing reconstruction on the whole image, it may be more effective to apply reconstruction to object-specific spatial regions, which is the proposed objective of this research. As an HSI may cover a large area, multiple objects are generally present within a single scene. Hence, spatial information can be highlighted accurately by specializing the reconstruction based on the local context. The local context may be defined by the so-called superpixels, i.e., finite sets of pixels that constitute a homogeneous set. Each superpixel may undergo tailored reconstruction, with a process expected to perform better than non-spatially-adaptive approaches. In this paper, a Superpixel-based SSA (SP-SSA) method is proposed where the image is first segmented into multiple regions using a superpixel segmentation approach. Next, each segment is individually reconstructed using 2D-SSA. In doing so, the spatial contextual information is preserved, leading to better classifier performance. The performance of the reconstructed features is evaluated using an SVM classifier. Experiments on four popular benchmark datasets reveal that, in terms of the classification accuracy, the proposed approach overperforms the standard SSA technique and various common spatio-spectral classification methods.

Keywords: hyperspectral image; superpixel segmentation; evaluation; 2D-singular spectrum analysis (2D-SSA); feature extraction

Citation: Subudhi, S.; Patro, R.N.; Biswal, P.K.; Dell'Acqua, F. Superpixel-Based Singular Spectrum Analysis for Effective Spatial-Spectral Feature Extraction. *Appl. Sci.* **2021**, *11*, 10876. https://doi.org/10.3390/app112210876

Academic Editors: Dario Gioia and Maria Danese

Received: 29 September 2021
Accepted: 2 November 2021
Published: 17 November 2021

1. Introduction

Recent advancements in hyperspectral sensors resulted in the increased availability of Hyperspectral Images (HSI) and a boost in their circulation among the remote sensing community. HSI data enables the discrimination of objects even with minor differences as it contains several contiguous spectral bands acquired from the visible to the infrared region [1] so that every small spectral difference can, in principle, be captured. The information is available in the form of a 3-D structure that contains a 2-D spatial scene along with a 1-D spectral signature. These unique characteristics of HSI have made them popular in several application areas, such as agriculture [2], mineralogy [3], land cover classification [4], target detection [5], and others. However, effective classification of HSI is still an open challenge.

Several classification techniques, such as K-nearest neighbor (KNN) [6], support vector machine (SVM) [7], multinomial logistic regression (MLR) [8], Extreme Learning Machine (ELM) [9], and Sparse Representation Classifier (SRC) [10] have been proposed in the past decades. The richness in spectral information attracted research efforts on pixel-based processing and classification. SVM is the most popular and widespread classifier due to its lower generalization error rate that makes it capable of identifying even minor changes in spectral signatures. Due to the high spectral dimensionality compared to a generally limited number of class-specific training samples, it is quite difficult to properly estimate the model parameters. Hence, there is a need to adopt effective spatial-spectral feature extraction approaches to overcome the aforementioned challenges.

To deal with the issue of higher spectral dimensionality, several linear (e.g., Principal Component Analysis (PCA) [11], Independent Component Analysis (ICA) [12], and Linear Discriminant Analysis (LDA) [13]) and non-linear (manifold learning [14]) dimensionality reduction (DR) methods have been introduced. Band selection approaches may also be utilized to select the most informative bands out of several available bands [15,16]. Spectral features alone, however, may not be sufficient to score very high accuracy values. To improve performance, it is necessary to incorporate spatio-spectral features that help increasing the separability of classes.

Recently, various spatial feature extraction techniques have been proposed. Mathematical Morphology is one of the most popular approaches that is extensively utilized by researchers. The concept of Extended Morphological Profiles (EMP) for FE in HSI was first proposed by Benediktsson et al. [17]. This technique utilizes morphological opening and closing transformations to extract spatial geometrical information. Later, Dalla Mura et al. [18] proposed Morphological Attribute Filters (MAP) for the spatial FE. From that point onwards, several variations of Attribute Profiles (AP) were created. Ghamisi et al. [19] conducted a comprehensive survey on the evolution in Attribute Profiles.

Texture Descriptors, including Wavelet transform [20], Gray-Level Co-occurrence Matrix (GLCM) [21], Local Binary Patterns (LBP) [22], and Gabor filters [23], have also been used in the literature for spatial FE. Filtering, i.e., moving-window-based processing, is another approach to extract spatial-spectral features. Various edge-preserving filters, such as Bilateral Filters [24], Trilateral Filters [25], Guidance filters [26], and Domain Transform Recursive Filters [27] have been introduced for spatial FE in the literature. The texture and noise variations are minimized by performing smoothing operations; however, important details, such as edges and lines, are well preserved by these filters [28].

In addition to these techniques, 2D-SSA is another interesting approach for spatial feature extraction. Using this approach, each band image of HSI is initially decomposed into varying trends, oscillations, and noise. Later, HSI is reconstructed using the selected oscillations and trends [29,30]. In 2D-SSA, the spatial structural information is extracted by utilizing the characteristics of the surrounding pixels in a specific embedding window. It can withstand high levels of noise and generally achieves good data classification results.

2D-SSA suffers, however, from several limitations, such as reduced utilization of the abundant spectral information available in data, and over-smoothing or under-smoothing of classification results because of the fixed embedding window size. To overcome the challenge of selecting the optimal embedding window size, recently, multi-scale 2D-SSA has been proposed for the effective extraction of discriminative spatial features under different noise conditions [31,32].

Superpixel segmentation techniques have gained popularity in recent years due to their capability of exploiting spatial structural information adaptively in an image. In [33], a survey on superpixel segmentation as a preprocessing step in HSI analysis was presented. A superpixel-based classification via multiple kernels (SCMK) approach was proposed in [34]. In [35], a region-based relaxed multiple kernel (R2MK) method was proposed that combines the multiscale spectral and spatial features using a kernel collaborative representation classification technique.

To obtain superior classification performance and solve the problem of optimal superpixel number selection, an adjacent superpixel-based multiscale spatial-spectral kernel (ASMGSSK) was proposed in [36]. In [37], a multiscale segmentation-based SuperPCA model (MSuperPCA) was developed, which can effectively integrate multiscale spatial information to obtain the optimal classification result by decision fusion.

Recently, deep learning techniques have become quite popular in the classification of HSI data due to their ability to extract discriminant and abstract features by using a series of hierarchical layers. The initial layers usually extract texture and edge information, whereas deeper layers highlight more complicated features. Some of the most popular deep learning frameworks include stacked autoencoders (SAE) [38], Deep Belief Networks (DBN) [39], Convolution Neural Networks (CNN) [40], Recurrent Neural Networks (RNN) [41], Generative Adversarial Networks (GAN) [42], etc.

Although deep learning approaches have several advantages, they also pose significant challenges in HSI applications. First of all, to achieve better classification result, often deep learning techniques demand large volumes of training samples. Moreover, a large number of hyper-parameters (like the kernel sizes, learning rate, etc.) are involved in training complex deep learning networks mainly designed for feature extraction and classification. Hence, the process becomes computationally expensive.

The disadvantages of combining SSA with structured approaches to incorporating spatial information may be overcome by using more flexible ways to spatially partition the dataset. In line with this consideration, in this work, a superpixel-based SSA (SP-SSA) algorithm was proposed as a means to increase the classifier performance. Instead of performing direct reconstruction, an object-specific reconstruction is performed to accurately preserve the local contextual information. Superpixel segmentation is first applied on the input HSI to generate a segmented HSI where each sub-region carries similar characteristic features, and its shape and size is adjusted according to the local image structure information. Next, 2D-SSA is individually applied on each segmented region to produce the reconstructed HSI. Lastly, the final classification map is generated by using the popular SVM classifier. The major novel contributions of this work are highlighted in the following list:

1. Direct reconstruction is usually performed in standard 2D-SSA algorithms, where the full image is reconstructed. In HSIs, however, object-specific reconstruction is always better than direct reconstruction, as, in this way, local contextual information can be captured accurately. In this work, a novel SP-SSA approach is proposed that performs object-specific reconstruction.
2. Superpixel segmentation and 2D-SSA are combined together for the first time for accurate spatial-spectral feature extraction. Using SP-SSA, each superpixel, i.e., object-specific spatial region is reconstructed.
3. Superior classifier performance is achieved with the proposed method in comparison to other state-of-the-art methods, even with a comparatively small number of training samples.

The remainder of this paper is organized as follows. A detailed description of the proposed method is presented in Section 2. The experimental setup, results, and analysis are described in Section 3. Finally, some conclusions and future work are discussed in Section 4.

2. The Proposed Methodology

The proposed SP-SSA method includes three stages as described in Figure 1. In stage 1, superpixel segmentation is applied on the input HSI to obtain the segmented HSI. In stage 2, each segmented region is reconstructed using 2D-SSA to obtain the reconstructed HSI. In the final stage, an SVM classifier is applied on the reconstructed HSI to build the final classification map. A detailed description of each of these stages is presented in the subsections below.

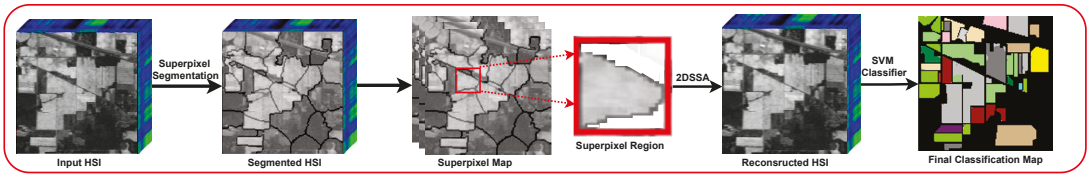

Figure 1. Flowchart of the proposed method.

2.1. Superpixel Segmentation

Superpixel segmentation approaches have gained popularity in recent years as these approaches have several benefits. Using superpixels, the computational complexity can be drastically reduced by computing features on more meaningful regions rather than acting on each individual pixel in HSI [43]. Simple Linear Iterative Clustering (SLIC) [44] is one of the most popular gradient-ascent-based superpixel segmentation approaches, where an initially defined tentative set of cluster points are iteratively refined using a gradient-ascent method until some convergence criteria are met. This algorithm has lower computational complexity as it applies the *k*-means method locally. The algorithm includes four key steps that can be summarized as follows.

The first step is cluster center initialization. Let the input HSI be denoted as $H^b \equiv \{h_1^b, h_2^b, \ldots, h_N^b\}$ with N pixels, where $\{h_i^b\}$ represents the value at the ith pixel for the bth spectral band and $i = 1, 2, \ldots N; b = 1, 2, \ldots B$. B is the total number of spectral bands. Each pixel can be labeled as $A_i = [h_i, r_i, u_i]$, where $h_i^T = [h_1, h_2, \ldots, h_B]^T$ is the spectral vector and $[r_i, u_i]^T$ is the position vector. The K number of initial cluster centers $\mathcal{C}_j = [h_j, r_j, u_j]^T$ are sampled on a regular $Q \times Q$ ($Q = \sqrt{\frac{N}{K}}$) grid and are, thus, equally spaced apart [45].

The next step is the cluster assignment step, where each pixel is assigned to the nearby cluster center based on the computed distance measure D. Distance is computed within a $2Q \times 2Q$ window around the cluster center. The distance between the cluster center $\mathcal{C}_j$ and pixel A_i is calculated as follows (Equation (1)):

$$D = D_{spectral} + \frac{w}{Q} D_{spatial} \tag{1}$$

where w is the weighting factor between spectral and spatial features. The spectral and spatial distance between pixel i and j are represented as in Equations (2) and (3) below.

$$D_{spectral} = \sqrt{\sum_{b=1}^{B} \left(h_i^b - h_j^b\right)^2} \tag{2}$$

where $D_{spectral}$ is the measure of homogeneity within the superpixels.

$$D_{spatial} = \sqrt{(r_i - r_j)^2 + (u_i - u_j)^2} \tag{3}$$

where (r_i, u_i) denotes the location of pixel i in the superpixels. The spatial distance $D_{spatial}$ ensures regularity and compactness in the generated superpixels.

In the third step, the cluster centers are updated with the mean value of all pixels belonging to the same cluster. The second and third steps are iteratively repeated until convergence is achieved.

In the final step, post-processing is performed to enforce connectivity by reassigning disjoint pixels to nearby superpixels.

2.2. 2D-SSA

SSA is capable of decomposing a series into multiple independent components or subseries, where each extracted eigenvalue represents an individual component of the

original series. The SSA can be applied to the respective spectral bands of the hypercube, thereby, decomposing the 2-D scene, and then reconstructing it using the respective main components while removing the noise contribution. As a data cube is decomposed in this way, the local structure and main spatial trends are typically found in the first component. Hence, when all images within the hyperspectral cube are decomposed and only the first components are selected to individually reconstruct each of them, a resulting cube with minimum noise is generated. The SSA can be implemented using the following four steps:

2.2.1. Embedding

Imagine a HSI dataset H, with a size of $N_x \times N_y \times B$, where N_x, N_y indicates the band image size and B represents the total number of available bands. Each band image H^b ($b \in B$) can be expressed as follows:

$$H^b = \begin{bmatrix} H^b_{1,1} & H^b_{1,2} & \cdots & H^b_{1,N_y} \\ H^b_{2,1} & H^b_{2,2} & \cdots & H^b_{2,N_y} \\ \vdots & \vdots & \ddots & \vdots \\ H^b_{N_x,1} & H^b_{N_x,2} & \cdots & H^b_{N_x,N_y} \end{bmatrix}_{N_x \times N_y} \tag{4}$$

Next, a 2D window Q^b is defined, whose dimensions are $M_x \times M_y$.

$$Q^b = \begin{bmatrix} H^b_{i,j} & H^b_{i,j+1} & \cdots & H^b_{i,j+M_y-1} \\ H^b_{i+1,j} & H^b_{i+1,j+1} & \cdots & H^b_{i+1,j+M_y-1} \\ \vdots & \vdots & \ddots & \vdots \\ H^b_{i+M_x-1,j} & H^b_{i+M_x-1,j+1} & \cdots & H^b_{i+M_x-1,j+M_y-1} \end{bmatrix}_{M_x \times M_y} \tag{5}$$

where $1 \leq M_x \leq N_x$, $1 \leq M_y \leq N_y$, and $1 < M_x M_y < N_x N_y$. Each pixel is spatially positioned by (i, j) within the image H^b. The pixels in a window Q^b can be rearranged into a column vector $C^b_{i,j} \in \mathbb{R}^{M_x M_y}$ according to the reference position (i, j) as follows:

$$C^b_{i,j} = [H^b_{i,j}, H^b_{i,j+1}, \ldots, H^b_{i,j+M_y-1}, H^b_{i+1,j}, H^b_{i+1,j+1}, \ldots, H^b_{i+M_x-1,j+M_y-1}]^T \tag{6}$$

To scan the whole image H^b, this 2-D window is slid across it from top left to bottom right until it has visited every position on the entire image (see also Figure 2 for a graphical explanation).

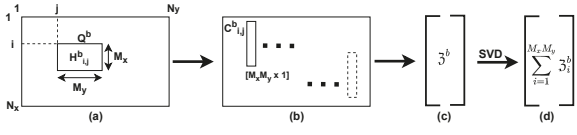

Figure 2. Moving window across the image H^b to create the trajectory matrix $\mathfrak{Z}^b$.

As a result, the trajectory matrix $\mathfrak{Z}^b$ of all feasible 2-D windows of image H^b of size $M_x M_y \times (N_x - M_x + 1)(N_y - M_y + 1)$ can be obtained as follows:

$$\mathfrak{Z}^b = \left[(C^b_{1,1})^T, (C^b_{1,2})^T, \ldots, (C^b_{1,N_y-M_y+1})^T, (C^b_{2,1})^T, \ldots, (C^b_{N_x-M_x+1,N_y-M_y+1})^T \right]_{M_x M_y \times (N_x-M_x+1)(N_y-M_y+1)} \tag{7}$$

Note that the trajectory matrix $\mathfrak{Z}^b$ has a structure of Hankel–block–Hankel (HbH). $\mathfrak{Z}^b$ can be expressed as follows:

$$\mathfrak{Z}^b = \begin{bmatrix} P_1^b & P_2^b & \cdots & P_{N_x-M_x+1}^b \\ P_2^b & P_3^b & \cdots & P_{N_x-M_x+2}^b \\ \vdots & \vdots & \ddots & \vdots \\ P_{M_x}^b & P_{M_x+1}^b & \cdots & P_{N_x}^b \end{bmatrix}_{M_x \times (N_x - M_x + 1)} \tag{8}$$

Each of the submatrices P_i^b corresponds to a Hankel structure as follows:

$$P_i^b = \begin{bmatrix} H_{i,1}^b & H_{i,2}^b & \cdots & H_{i,N_y-M_y+1}^b \\ H_{i,2}^b & H_{i,3}^b & \cdots & H_{i,N_y-M_y+1}^b \\ \cdot & \cdot & \cdot & \cdot \\ \cdot & \cdot & \cdot & \cdot \\ \cdot & \cdot & \cdot & \cdot \\ H_{i,M_y}^b & H_{i,M_y+1}^b & \cdots & H_{i,N_y}^b \end{bmatrix}_{M_y \times (N_y - M_y + 1)} \tag{9}$$

2.2.2. Singular Value Decomposition (SVD)

After obtaining the trajectory matrix $\mathfrak{Z}^b$, SVD is applied to determine the eigenvalues $\left(\lambda_1 \geq \lambda_2 \geq \cdots \geq \lambda_{M_x M_y}\right)$, and the corresponding eigenvectors $\left(U_1, U_2, \cdots, U_{M_x M_y}\right)$ of $\left(\mathfrak{Z}^b \left(\mathfrak{Z}^b\right)^T\right)$. It is possible to rewrite $\mathfrak{Z}^b$ as follows:

$$\mathfrak{Z}^b = \mathfrak{Z}_1^b + \mathfrak{Z}_2^b + \cdots + \mathfrak{Z}_{M_x M_y}^b \tag{10}$$

where the ith elementary matrix is $\mathfrak{Z}_i^b = \sqrt{\lambda_i} U_i V_i^T$ and its Principal Components (PCs) are defined as $V_i = \frac{(\mathfrak{Z}^b)^T U_i}{\sqrt{\lambda_i}}$

2.2.3. Grouping

A subsequent operation is eigenvalue grouping, during which the total set of $M_x M_y$ individual components in (10) are divided into m subsets, designated as $S = [S_1, S_2, \ldots, S_m]$. By selecting one or more elementary matrices $\mathfrak{Z}_i^b$ from each subset, it is possible to derive the main information contained in an image without being disturbed by high noise levels. As a result, the trajectory matrix $\mathfrak{Z}^b$ can be represented as follows:

$$\mathfrak{Z}^b = \mathfrak{Z}_{S_1}^b + \mathfrak{Z}_{S_2}^b + \cdots + \mathfrak{Z}_{S_m}^b \tag{11}$$

The reconstruction of a single band scene of HSI using various numbers of components ($\mathfrak{Z}_i^b$) is compared in Figure 3. In general, the component with the highest eigenvalue is the most informative one, containing key features with the lowest noise contribution. With the inclusion of additional components, the reconstructed scene begins to resemble the actual scene. The reconstructed image obtained by grouping the 1st–5th components and 1st–10th components are very similar with marginal differences (Figure 3c,d). Hence, a small number of key components are sufficient to reconstruct the scene satisfactorily.

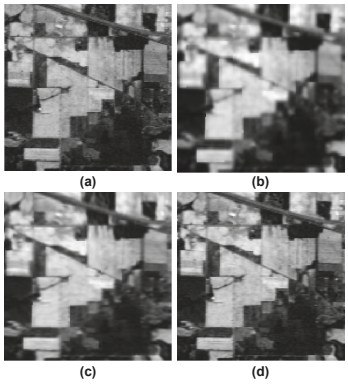

Figure 3. Implementation of 2D-SSA on a HSI scene (**a**) Original scene at 667 nm. (**b**) 1st component grouping. (**c**) 1–5th component grouping. (**d**) 1–10th component grouping, where $M_x = 5$, and $M_y = 5$.

2.2.4. Diagonal Averaging

3^b, in this case, does not necessarily belong to the HbH matrix type. It is projected into a 2D-signal by applying the Hankelization process in two steps; first inside every block (9) and next block-to-block (8) by averaging the anti-diagonal elements in the matrix. Thus, it is possible to obtain a reconstructed image that contains the distinctive spatial features based on the local contextual information present in a 2D window defined by the user.

2.3. Novelty of the Proposed SP-SSA Method

The proposed approach integrates SSA and superpixel segmentation for the first time to extract improved the spatio-spectral features from HSI. Reconstruction of object-specific spatial sections, rather than the entire image, may be more effective. Hence, in the proposed work, 2D-SSA is applied individually to each superpixel segmented region to extract the local contextual information accurately. The pseudo-code for the proposed SP-SSA algorithm is outlined in Algorithm 1.

Algorithm 1: Proposed SP-SSA algorithm for HSI classification.

Input: HS image, $H \in \mathbb{R}^{n \times b}$
Ground Truth GT
number of superpixels: K
Embedding Window Size:$M_x \times M_y$
Eigen Value Grouping: EV
Output: Classification Map $clsmap$ generated by SVM.

1: **for** $b = 1$ to B **do**
2: Perform SLIC superpixel segmentation to obtain segmentation map L from h^b containing K superpixel segments
L = SLIC (h^b,K) (as outlined in Section 2.1)
3: **for** $k = 1$ to K **do**
4: $h_k^{b'} = reconstruct2DSSA(L, M_x, M_y, EV)$ (as outlined in Section 2.2)
5: **end for**
6: **end for**
7: Obtained Reconstructed HSI $H' \in \mathbb{R}^{n \times b}$
8: $clsmap$ = SVM (H', GT)

For each superpixel, the reconstruction ($reconstruct2DSSA$ (Algorithm 1)) is applied to the rectangular Region of Interest (ROI) surrounding the superpixel (Figure 4). The ROI is created based on the location information of the pixels available in that particular segment. Only the reconstructed pixels specific to those pixels in the selected superpixel are

stored as spatial features, while the remaining reconstructed pixels in the ROI are discarded as they do not belong to the superpixel under test. The same procedure is applied to all other superpixels, and the HS image is reconstructed using the proposed SP-SSA approach. This procedure collects local object-specific superpixel-based spatial features for each band in the image.

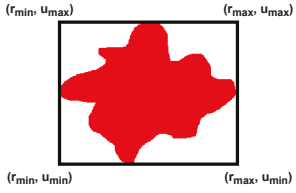

Figure 4. Possible Region of Interest (ROI) around the superpixel segment. (r, u) denotes the location of pixel i in superpixels. r_{min}, r_{max} represents the minimum and maximum row index, and u_{min}, u_{max} are the corresponding *min* and *max* column indices.

2.4. Classification

The selection of an appropriate classifier is critical in assessing the performance of the above-mentioned features, especially in hyperspectral images with a limited number of training samples. SVM is the most widely used supervised statistical learning framework among pixel-wise classifiers. With the help of a kernel function, data can be mapped to a higher-dimensional space via a nonlinear transformation, aiming to determine the best hyperplane for separating samples belonging to different classes. The performance of SVM in HSI classification is outstanding despite the variation of the data dimensions [46,47]. Hence, in this work, the SVM classifier is utilized to evaluate the performance of the reconstructed features.

3. Results and Discussion

This section reports the outcome of testing the proposed approach on some of the most popular benchmark datasets and compares it with other, state-of-art classification approaches.

3.1. Dataset Description

In this subsection, the datasets used for testing the proposed approach are presented and described.

3.1.1. Indian Pines

The first dataset, named "Indian Pines" (IP), was collected over Northwestern Indiana, USA, with the airborne AVIRIS sensor; it includes a total of 220 bands covering wavelengths from 0.4 to 2.5 µm. About 70% of the imaged area is agricultural land, while the remaining portions are forests. Due to the comparatively low spatial resolution (20 m/pixel) of the sensor, this dataset is challenging as it contains highly mixed pixels. The number of samples obtained per class is also unbalanced, which further complicates classification. The size of the scene is 145 × 145 pixels, and its Ground Truth (GT) data defines 16 different classes. The pseudo-color image, the GT map, and the class names for the dataset are all included in Figure 5.

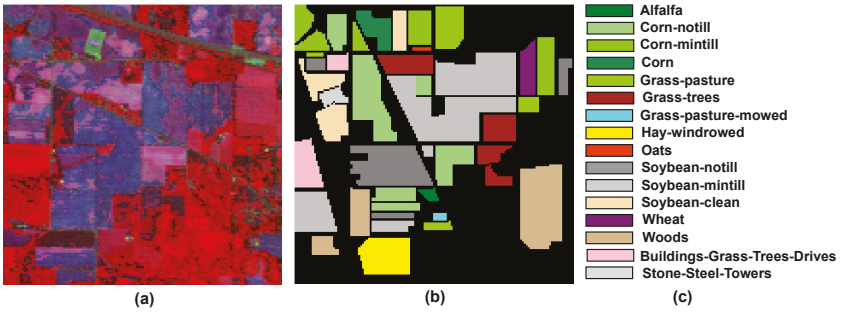

Figure 5. (**a**) False Color Composite Image, (**b**) Ground Truth Image and (**c**) Class names for the Indian Pines Dataset.

3.1.2. Pavia University

The ROSIS sensor was instrumental to the collection of this dataset over the University of Pavia, Italy. The dataset is called "Pavia University" (PU). It has a spatial resolution of 1.3 m and originally comprises 115 spectral bands covering wavelength ranges from 0.43 to 0.86 µm. In the final analysis, 103 bands are used after the elimination of noisy channels. The image has a size of 610 × 340 pixels, and it has nine challenging classes with nearly similar spectral reflectances. Detailed information about the false-color image, Ground Truth, and class names is displayed in Figure 6.

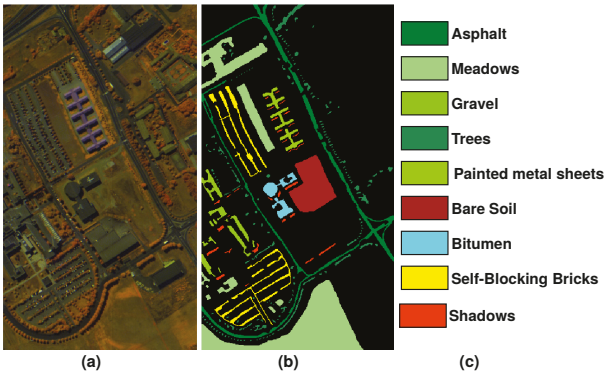

Figure 6. (**a**) False Color Composite Image, (**b**) Ground Truth Image and (**c**) Class names for the Pavia University Dataset.

3.1.3. Salinas Dataset

The "Salinas" (SAL) dataset was captured over the Salinas Valley, California, USA, using the AVIRIS Sensor. The sensor has 224 channels with spectral range varying from 0.43 µm to 2.5 µm. This scene has a size of 512 ×217 pixels and spatial resolution of 3.7 m per pixel. The number of bands reduces to 204 after discarding 20 water absorption bands: [108–112], [154–167], 224. The scene is mainly an agricultural area, with 16 classes in its Ground Truth. A false color representation, the Ground Truth, and the class names for the Salinas dataset are shown in Figure 7.

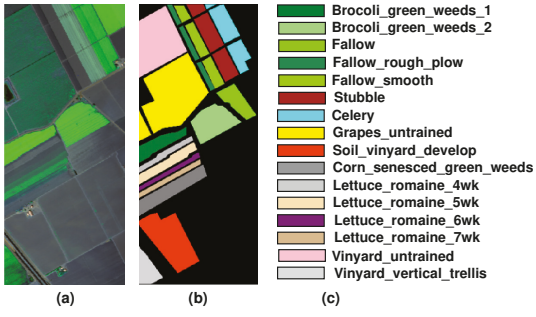

Figure 7. (**a**) False Color Composite Image, (**b**) Ground Truth Image, and (**c**) Class names for the Salinas Dataset.

3.1.4. Houston 2018

The 2018 IEEE GRSS Data Fusion Contest (DFC) triggered public dissemination of this rich dataset, which was included in our tests to increase their statistical significance. The image of the Houston campus and its surrounding area was captured by the IRTES CASI-1500 sensor at a GSD of 1 m over Houston, Texas, USA. It has 601 $\times$ 2384 pixels and 50 spectral bands with wavelengths ranging from 380 to 1050 nm sampled at 10 nm intervals. The scene contains 20 urban landcover classes. The false-color composite image, ground truth image, and class names for the Houston 2018 dataset are provided in Figure 8.

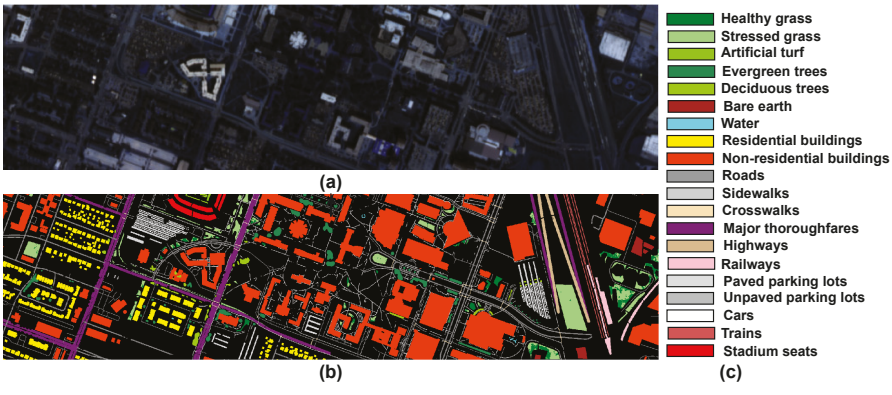

Figure 8. (**a**) False-Color Composite Image, (**b**) Ground Truth Image, and (**c**) Class names for the Houston-2018 Dataset.

3.2. Experimental Setup

Our proposed approach was evaluated by comparing its performance with eight state-of-the-art approaches for HSI feature extraction (Algorithm 2, see Section 3.4.5). These include SVM [7], Edge Preserving Filter (EPF) [26], superpixel-based classification via multiple kernels (SCMK) [34], region-based relaxed multiple kernel (R2MK) [35], adjacent superpixel-based multiscale generalized spatial-spectral kernel (ASMGSSK) [36], Multiscale superpixel-based PCA (MsuperPCA) [37], 2D Singular Spectrum Analysis (2D-SSA) [29], and 2D Multiscale Singular Spectrum Analysis (2D-MSSA) [31]. A common way to measure the efficiency of feature extraction is through the accuracy of the classifier scored by the experiments. As a result, the classification setup must be appropriate with the current state-of-the-art. In light of this, SVMs have demonstrated themselves to be robust and efficient in multi-class classification applications.

The LIBSVM toolbox [48] is used to implement SVM as the default classifier for all of the involved methods. A Gaussian RBF kernel is utilized for SVM implementation,

and a grid search is applied to tune both key parameters of RBF-SVM; the penalty c and the gamma γ. The SVM parameters are kept constant across all competitive experiments for a fair comparison. To avoid systematic errors and reduce random discrepancies, all experiments were independently carried out ten times each with different training and testing subsets, with no overlap between each training and the corresponding testing subset. This was intended to ensure good statistical significance for our experiments.

Stratified sampling was used to randomly obtain the training and testing subsets. For training, 3%, 2%, 1%, and 0.2% samples per class were selected for the IP, PU, SAL, and Houston 2018 datasets, respectively. Additionally, four objective quality indices are utilized to evaluate image classification results: namely the OA, the average accuracy (AA), the kappa coefficient, and class-by-class accuracy. All experiments were conducted using MATLAB R2018b software, installed on a personal computer with an Intel core i5-6200 CPU clocked at 2.30 GHz, and 16 GB RAM.

3.3. Parameter Sensitivity Analysis

Table 1 displays the best parameter settings for the competing algorithms, found by experimentation. For the proposed SP-SSA algorithm, the size of the 2-D embedding window was set to 5×5 pixels for the IP and Salinas dataset; whereas, for the PU and Houston 2018 dataset, the window size was set at 3×3 pixels. For the IP and SAL datasets, superpixels were set at 100. However, the amount of superpixels in the PU and Houston 2018 datasets were set to 150 and 500, respectively. The effect of window size variation for different number of superpixels on the classification performance for the experimental datasets is provided in Figure 9.

As each superpixel is reconstructed individually, smaller window sizes are preferred since they lead to better image reconstructions. Using a large window may smooth the results too much and result in mixing errors. A 2D-SSA algorithm was presented in [29] for feature extraction in HSI, where various window sizes, such as 5×5, 10×10, 20×20, 40×40, and 60×60, were examined. The IP and SAL datasets produced the best classification accuracy when the window size was set at 10×10. When analyzing the PU and Houston dataset, the window sizes of 5×5 showed the best classification results. Since the optimal window size may vary depending on the dataset, ref. [31] adopts a multiscale strategy to improve the generalization ability.

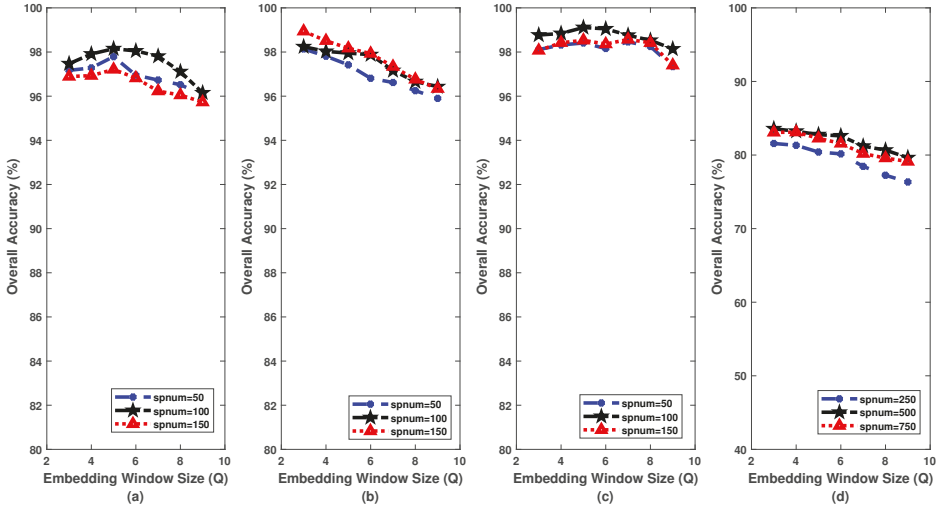

Figure 9. Effect of window size variation for different number of superpixels on the classification performance for the (**a**) Indian Pines (**b**) Pavia University, and (**c**) Salinas, and (**d**) Houston 2018 datasets.

Table 1. Parameter settings for different algorithms in the Indian Pines, Pavia University, Salinas, and Houston 2018 Datasets.

Method	Indian Pines, Salinas	Pavia University	Houston 2018
SVM	NA	NA	NA
EPF	δ_s = 3, δ_r = 0.2, r = 3, and ϵ = 0.01	δ_s = 3, δ_r = 0.2, r = 3, and ϵ = 0.01	δ_s = 5, δ_r = 0.1, r = 3, and ϵ = 0.02
SCMK	$\sigma = 2^{-6}$; spnum = 600; μ_1 = 0.2, μ_2 = 0.2	$\sigma = 2^{-4}$; spnum = 900; μ_1 = 0.2, μ_2 = 0.4	$\sigma = 2^{-5}$; spnum = 1600; μ_1 = 0.1, μ_2 = 0.3
R2MK	$\sigma = 2^{-6}$; spnum = [20,50,100,200,400,800]; μ = 0.2	$\sigma = 2^{-5}$; spnum = [50,100,200,400,800,1600]; μ = 0.3	$\sigma = 2^{-4}$; spnum = [50,100,200,400,800,1600,3200]; μ = 0.1
ASMGSSK	r_0 = 0.1; $\sigma = 2^{-7}$; spnum = [100,200,400,800,1600,3200]	r_0 = 0.1; $\sigma = 2^{-5}$; spnum = [200,400,800,1600,3200,6400]	r_0=0.2; $\sigma = 2^{-4}$; spnum = [200,400,800,1600,3200,6400]
MsuperPCA	Fundamental spnum = 100; scale no = 4	Fundamental spnum = 20; scale no = 6	Fundamental spnum = 100; scale no = 8
2DSSA	Window Size: 10 × 10; EVG = 1st	Window Size: 5 × 5; EVG = 1 − 2nd	Window Size: 5 × 5; EVG = 1 − 2nd
2DMSSA	Window Size: 5 × 5, 10 × 10, 20 × 20, 40 × 40, 60 × 60	Window Size: 5 × 5, 10 × 10, 20 × 20, 40 × 40, 60 × 60	Window Size: 5 × 5, 10 × 10, 20 × 20, 40 × 40, 60 × 60
SP-SSA	spnum: 100; Window Size: 5 × 5; EVG = 1	spnum: 150; Window Size: 3 × 3; EVG = 1 − 2nd	spnum: 500; Window Size: 3 × 3; EVG = 1 − 2nd

3.4. Experimental Result and Analysis

In this section, the four HSI data sets outlined in Section 3.1 are utilized, and several experiments are performed to examine the efficacy of the proposed SP-SSA method. Figure 10 compares the classification results obtained with varying numbers of training samples on four datasets. It can be noted that better classification performance is evident when larger numbers of labeled samples are utilized for training; after passing the percentages used in this work; however, the accuracy level mostly plateaus, and no further significant improvement is observed. Our proposed approach attains the best classification accuracy in almost all cases, regardless of the number of samples, proving its robustness. Classification results from all four data sets are provided in Tables 2–5 and quantitatively support the dominance of the proposed method. Individual classification maps generated by the proposed SP-SSA method and all the compared approaches are displayed in Figures 11–14.

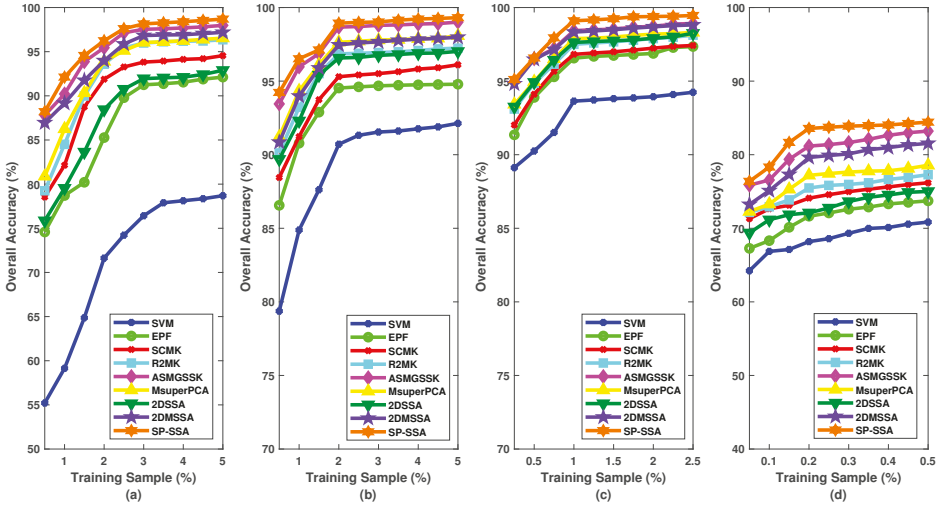

Figure 10. Effect of training sample variation on the classification performance for the (**a**) Indian Pines (**b**) Pavia University, (**c**) Salinas, and (**d**) Houston 2018 datasets.

3.4.1. Results from the Indian Pines Dataset

Based on the results shown in Table 2, the proposed method achieves the best values across three metrics, and its accuracy exceeded 89% on almost all classes. In the tables, the best results in each row are highlighted in bold font. When comparing SP-SSA with raw HSI data, the OA improved substantially from 76.42% to 98.15%. In addition, comparisons between SVM and other methods indicated that the incorporation of spatial features can enhance the classification performance compared to considering spectral features alone.

Superpixel-based methods, such as SCMK, R2MK, ASMGSSK, and MsuperPCA techniques, yield higher classification accuracy as compared to non-superpixel based techniques (EPF, 2D-SSA, and 2D-MSSA); by grouping spectrally identical regions, superpixels offer a powerful way to exploiting spatial/contextual information. It can also be noted that methods considering multi-scale windows (ASMGSSK, MsuperPCA, and 2D-MSSA) perform better with respect to fixed-window methods. Due to the different window sizes, unique local spatial features can be exploited, which allows better covering of different sizes of land cover classes and different scales of spatial features. On the downside, the use of multiscale approaches involves heavier processing burdens. As the proposed method reconstructs each superpixel individually, better classification results are obtained.

Table 2. Classification results for the Indian Pines Dataset with 3% training for SVM, EPF, SCMK, R2MK, ASMGSSK, MsuperPCA, 2D-SSA, 2D-MSSA, and SP-SSA algorithms.

Class	Samples	SVM	EPF	SCMK	R2MK	ASMGSSK	MsuperPCA	2DSSA	2DMSSA	SP-SSA
Alfalfa	46	12.65	22.22	62.79	92.86	**95**	87.8	54.55	87.8	92.11
Corn-notill	1428	75.18	92.85	92.55	94.06	94.85	97.09	91.81	95.25	**98.25**
Corn-mintill	830	82.46	83.44	90	93.32	97.37	90.11	88.96	96.65	**97.99**
Corn	237	47.86	79.39	85.59	95.41	96.14	**99.53**	80.89	89.2	96.98
Grass-pasture	483	69.25	68.04	89.67	97.3	**99.05**	95.81	90.61	92.41	97.04
Grass-trees	730	80.19	96.72	**99.56**	98.36	99.21	98.61	93.23	99.54	99.51
Grass-pasture-mowed	28	88.89	88.46	69.23	80	**100**	96	92.59	92	**100**
Hay-windrowed	478	93.46	**100**	98	98.18	98.32	95.07	98.46	99.54	99
Oats	20	36.12	47.37	**100**	52.63	47.06	94.12	42.11	83.33	**100**
Soybean-notill	972	76.74	82.96	88.29	90.16	96.57	95.27	87.12	**96.91**	93.63
Soybean-mintill	2455	79.51	97.03	95.54	97.48	98.5	96.66	93.1	97.19	**99.03**
Soybean-clean	593	50	86.99	93.18	95.79	97.29	95.27	90.96	96.07	**98.6**
Wheat	205	99.01	96.94	92.23	**100**	97.21	98.9	99.48	98.91	**100**
Woods	1265	88.74	99.26	98.91	99.48	99.27	99.02	96.42	**99.82**	99.62
Buildings-Grass-Trees-Drives	386	65.18	87.87	**99.45**	94.37	96.73	88.95	90.16	94.24	98.46
Stone-Steel-Towers	93	41.32	97.75	72.73	92.94	97.5	93.9	97.75	**98.81**	89.74
OA::		76.42	91.25	93.82	95.98	97.54	96.04	91.95	96.83	**98.15**
AA::		67.91	82.96	89.23	92.02	94.38	95.13	86.76	94.86	**97.5**
K::		73.05	89.98	92.95	95.32	97.2	95.49	90.82	96.39	**97.89**

Figure 11 displays the classification maps produced by various approaches for the Indian Pines dataset. For the SVM approach, the classification map appears very noisy if spatial features are not considered. Through the use of neighborhood spatial information, the EPF and 2D-SSA techniques can suppress spot-wise misclassification to a large extent, but these methods do not preserve the detailed structures of the HSI well enough.

However, by adopting superpixel-based approaches, the generated classification map becomes much smoother, and more accurate estimates are obtained in the detailed region. With the utilization of multi-scale approaches (like ASMGSSK, MSuperPCA, and 2D-MSSA), the amount of misclassification is further reduced. Still, even with multi-scale approaches, landcover boundaries are frequently misplaced. As can be observed from Figure 11, the proposed approach effectively solved the above-mentioned problems due to its considerate utilization of spectral and spatial features.

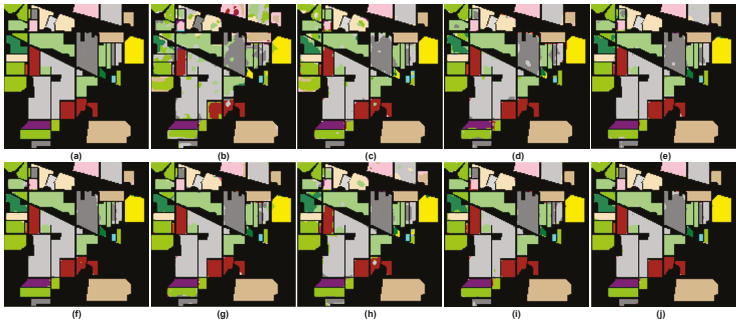

Figure 11. (**a**) Ground Truth Image, Classification Maps of (**b**) SVM (**c**) EPF (**d**) SCMK (**e**) R2MK (**f**) ASMGSSK (**g**) MsuperPCA (**h**) 2D-SSA (**i**) 2D-MSSA (**j**) SP-SSA for Indian Pines dataset.

3.4.2. Results from the Pavia University Dataset

Quantitative results are presented in Table 3. The proposed SP-SSA method still achieved higher classification accuracy and ranked first among all the compared methods, closely followed by the ASMGSSK algorithm. Also, in comparison to EPF, SCMK, R2MK, 2D-SSA, MSuperPCA, and 2D-MSSA techniques, the average improvement of the proposed approach is over 4.41%, 3.64%, 2.09%, 2.37%, 1.3%, and 1.48%, respectively. For comparison, the top results in the tables are boldfaced. In Figure 12, different classification maps are shown, based on various testing methods applied to the PU dataset.

According to Figure 12, the classification map for SVM still continues to remain noisy. Both EPF and 2D-SSA can generate a relatively smooth result; however, some significant regions remain undetected (e.g., the detailed areas). The superpixel-based methods (SCMK, R2MK, ASMGSSK, and MSuperPCA) and SSA-based approach (2D-SSA and 2D-MSSA) offer significantly improved performance, but the proposed 2D-SSA method remains the most promising approach as it outperforms all the compared algorithms.

Table 3. Classification results for the Pavia University Dataset with 2% training for SVM, EPF, SCMK, R2MK, ASMGSSK, MsuperPCA, 2D-SSA, 2D-MSSA, and SP-SSA algorithms.

Class	Samples	SVM	EPF	SCMK	R2MK	ASMGSSK	MsuperPCA	2DSSA	2DMSSA	SP-SSA
Asphalt	6631	90.79	96.33	94.01	95.43	**99.23**	97.19	97.12	97.61	98.94
Meadows	18,649	99.54	98.06	99.14	99.78	99.76	99.83	99.52	99.45	**99.85**
Gravel	2099	53.12	80.86	83.69	90.81	91.85	89.73	89.35	90.53	**94.17**
Trees	3064	81.9	83.81	87.34	93.8	98.22	95.53	96.24	95.76	**99**
Painted metal sheets	1345	93.04	**100**	99.17	**100**	99.17	**100**	99.47	99.46	**100**
Bare Soil	5029	89.64	94.15	96.46	96.81	99.6	98.01	95.76	98.52	**99.74**
Bitumen	1330	55.48	89.74	86.86	91.71	**99.42**	94.54	85.97	97.21	98.85
Self-Blocking Bricks	3682	87.92	91.47	90.97	90.97	94.69	93.05	89.11	92.64	**95.62**
Shadows	947	90.75	90.19	97.12	98.17	98.59	**98.89**	95.69	88.67	98.76
OA::		90.71	94.53	95.3	96.85	98.67	97.64	96.57	97.46	**98.94**
AA::		82.47	91.62	92.75	95.28	97.84	96.31	94.25	95.54	**98.33**
K::		87.57	92.73	93.76	95.82	98.23	96.87	95.44	96.63	**98.6**

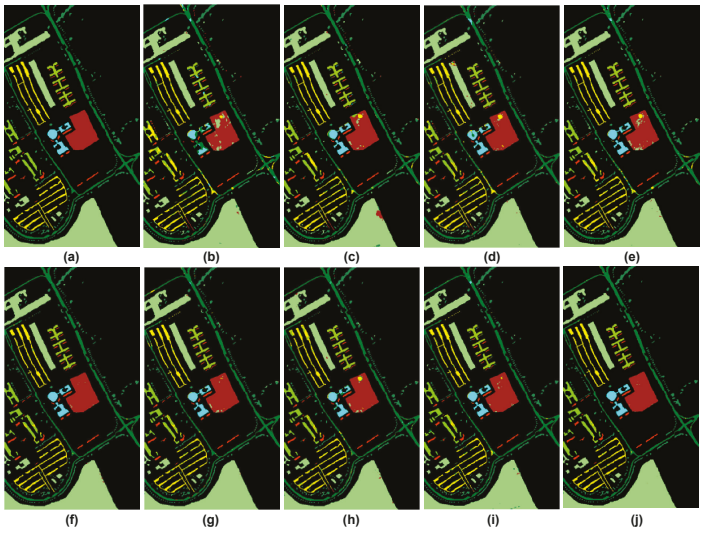

Figure 12. (**a**) Ground Truth Image, Classification Maps of (**b**) SVM (**c**) EPF (**d**) SCMK (**e**) R2MK (**f**) ASMGSSK (**g**) MsuperPCA (**h**) 2D-SSA (**i**) 2D-MSSA (**j**) SP-SSA for the Indian Pines dataset.

3.4.3. Results from the Salinas Dataset

The visual classification maps and quantitative results obtained by various classifiers on the Salinas dataset are shown in Figure 13 and Table 4, respectively. In the table, the best results are shown in bold. Based on the visual quality as well as objective metrics, it can be observed that the proposed SP-SSA method outperformed other competing approaches. In addition, compared with the 2D-SSA method that globally reconstructs the image using fixed-size embedded windows, the SP-SSA method considers the local spatial information by reconstructing each superpixel individually, which helps in further reducing the disturbances and improving the class assignment.

Table 4. Classification Results for the Salinas Dataset with 1% training for SVM, EPF, SCMK, R2MK, ASMGSSK, MsuperPCA, 2D-SSA, 2D-MSSA, and SP-SSA algorithms

Class	Samples	SVM	EPF	SCMK	R2MK	ASMGSSK	MsuperPCA	2DSSA	2DMSSA	SP-SSA
Brocoli-green-weeds-1	2009	99.74	98.43	99.44	99.85	99.36	99.39	98.83	**100**	99.64
Brocoli-green-weeds-2	3726	**100**	99.92	**100**	98.62	**100**	99.82	**100**	**100**	99.96
Fallow	1976	93.34	99.31	99.9	**100**	99.71	99.89	99.64	99.64	**100**
Fallow-rough-plow	1394	96.37	97.28	98.52	98	98.26	98.56	97.38	97.54	**98.67**
Fallow-smooth	2678	91.19	99.06	97.77	99.42	98.72	99.75	98.42	99.25	**99.63**
Stubble	3959	**100**	99.92	98.54	99.92	**100**	**100**	**100**	**100**	**100**
Celery	3579	99.18	99.65	99.14	99.54	99.8	99.78	**100**	99.88	99.96
Grapes-untrained	11,271	91.38	92.49	94.6	95.2	96.77	95.76	95	96.31	**97.91**
Soil-vinyard-develop	6203	97.34	99.88	99.65	99.98	99.82	99.96	99.66	99.95	**100**
Corn-senesced-green-weeds	3278	93.96	97.37	**98.96**	97.42	98.47	98.24	96.73	98.3	98.82
Lettuce-romaine-4wk	1068	81.66	96.55	96.81	97.78	97.99	97.92	97.24	97.86	**99.87**
Lettuce-romaine-5wk	1927	98.03	**100**	**100**	**100**	**100**	**100**	**100**	**100**	**100**
Lettuce-romaine-6wk	916	98.85	97.01	97.41	99.55	99.69	**99.76**	99.74	99.69	99.69
Lettuce-romaine-7wk	1070	92.92	98.23	99.13	98.17	99.07	98.86	**99.78**	99.47	99.73
Vinyard-untrained	7268	82.69	90.41	91.32	92.28	95.89	92.98	94.21	95.58	**97.7**
Vinyard-vertical-trellis	1807	95.63	99.13	90.3	99.83	99.6	99.82	98.57	99.29	**99.92**
OA::		93.64	96.56	96.82	97.5	98.43	97.89	97.63	98.33	**99.1**
AA::		94.52	97.79	97.59	98.47	98.95	98.78	98.45	98.92	**99.47**
K::		92.91	96.17	96.46	97.21	98.25	97.65	97.36	98.14	**99**

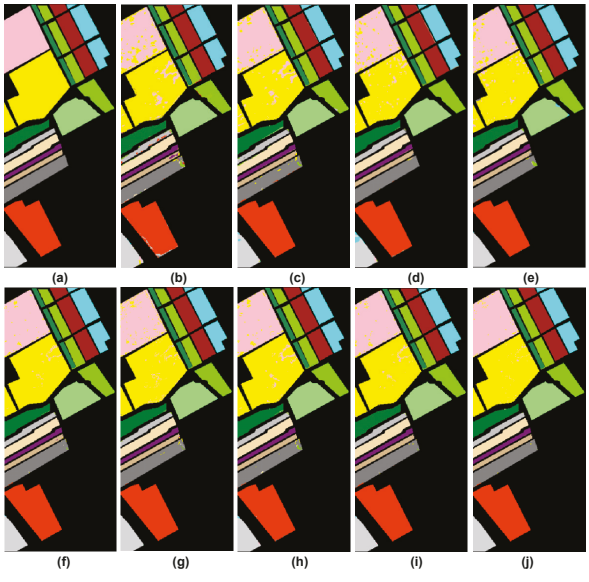

Figure 13. (**a**) Ground Truth Image, Classification Maps of (**b**) SVM (**c**) EPF (**d**) SCMK (**e**) R2MK (**f**) ASMGSSK (**g**) MsuperPCA (**h**) 2D-SSA (**i**) 2D-MSSA (**j**) SP-SSA for Salinas dataset.

3.4.4. Results from the Houston 2018 Dataset

The quantitative results for the Houston 2018 dataset with 0.2% training samples from each class are presented in Table 5. The corresponding classification map is shown in Figure 14. The best results from the tables are displayed in bold font for comparison. As observed from Table 5, the proposed methods are robust and achieve good classification results even for challenging scenes. The proposed approach improves accuracy from 68.19% to 83.57% for the SVM method. In this case also, the superpixel-based approaches (SCMK, R2MK) display superior performance as compared to non-superpixel based methods (EPF, 2DSSA). Here also, multi-scale window approaches (ASMGSSK, MsuperPCA, and 2D-MSSA) outperform fixed-window based methods as different scales of spatial features are incorporated into the analysis. Figure 14 also highlights the superiority of the proposed method. The salt and pepper noise is reduced by a greater extent, and a smoother classification map is produced with the proposed method.

Table 5. Classification results for the Houston Dataset with 0.2% training for SVM, EPF, SCMK, R2MK, ASMGSSK, MsuperPCA, 2D-SSA, 2D-MSSA, and SP-SSA algorithms.

Class	Samples	SVM	EPF	SCMK	R2MK	ASMGSSK	MsuperPCA	2DSSA	2DMSSA	SP-SSA
Healthy grass	9799	62.84	65.71	73	74.49	81.46	76.44	76.64	**84.51**	79.28
Stressed grass	32,502	84.4	85.08	83.83	86.42	89.88	88.67	83.7	90.99	**91.33**
Artificial turf	684	**100**	98.83	**100**	99.41	**100**	**100**	**100**	**100**	**100**
Evergreen trees	13,588	83.72	73.99	80.15	84.76	87.77	82.43	80.43	**91.13**	87.37
Deciduous trees	5048	43.98	36.75	50.54	51.74	63.82	55.89	46.38	58.26	**73.94**
Bare earth	4516	79.32	82.67	86.28	88.46	94.01	91.1	80.64	89.04	**96.21**
Water	266	66.42	67.8	61.89	68.06	83.08	68.18	74.62	66.92	**85.71**
Residential buildings	39,762	68.26	77.29	77.52	79.2	84.37	82	74.76	78.07	**87.39**
Non-residential buildings	223,684	82.57	85.51	87.3	88.31	91.64	89.18	86.05	90.63	**92.73**
Roads	45,810	40.41	43.7	46.79	47.33	58.86	51.39	42.75	53.25	**63.89**
Sidewalks	34,002	31.36	35.3	37.58	37.51	43.74	39.25	33.65	**51.35**	49.71
Crosswalks	1516	4.96	9.02	8.63	9.12	13.66	9.26	7.62	5.2	**14.21**
Major thoroughfares	46,358	50.97	55.91	59.41	63.04	72.53	65.1	58.17	60.83	**75.48**
Highways	9849	49.7	60.35	61.19	63.93	73.83	70.78	59.55	68.92	**78.56**
Railways	6937	79.92	85.83	92	89.52	95.29	88.07	80.22	95.84	**97.29**

Table 5. *Cont.*

Class	Samples	SVM	EPF	SCMK	R2MK	ASMGSSK	MsuperPCA	2DSSA	2DMSSA	SP-SSA
Paved parking lots	11,475	54.91	63.2	74.02	69.99	**84.58**	74.63	64.9	74.18	84.33
Unpaved parking lots	149	58.78	83.11	83.67	77.03	81.63	85.71	81.08	81.76	**93.06**
Cars	6578	43.99	47	49.33	59.66	65.09	53.78	54.51	62.85	**70.22**
Trains	5365	40.83	40.54	58.92	51.3	77.4	61.14	52.66	79.19	**79.96**
Stadium seats	6824	86.42	93.25	87.78	93.86	96.62	94.18	83.53	**98.71**	98.43
OA::		68.19	71.64	74.1	75.48	81.32	77.2	72.11	79.08	**83.57**
AA::		60.69	64.54	67.99	69.16	76.96	71.36	66.09	74.08	**79.95**
K::		59.13	63.41	66.52	68.28	75.82	70.55	63.94	72.61	**78.73**

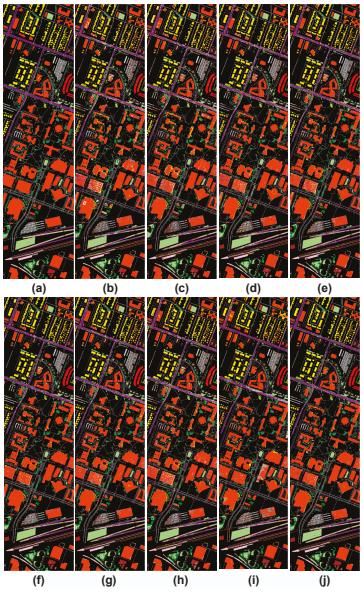

Figure 14. (**a**) Ground Truth Image, Classification Maps of (**b**) SVM (**c**) EPF (**d**) SCMK (**e**) R2MK (**f**) ASMGSSK (**g**) MsuperPCA (**h**) 2D-SSA (**i**) 2D-MSSA (**j**) SP-SSA for Houston 2018 dataset.

3.4.5. Statistical Evaluation

The effectiveness of the proposed method was statistically evaluated using McNemar's test. The classification results for all the test cases were compared using this test. The McNemar's test is defined as in Equation (12), where it is assumed that two generic algorithms, named Algorithm 1 and Algorithm 2 are compared.

$$Z = \frac{f_{12} - f_{21}}{\sqrt{f_{12} + f_{21}}} \tag{12}$$

In the equation above, f_{12} indicates the number of samples correctly classified by Algorithm 1 and incorrectly classified by Algorithm 2, and f_{12} indicates the number of samples for the opposite case. The performance of Algorithm 1 is better than Algorithm 2 if $Z > 0$. The differences between Algorithm 1 and Algorithm 2 are statistically significant if $|Z| > 1.96$. In our case, Algorithm 1 is the algorithm proposed in our manuscript, and Algorithm 2 is —sequentially— each one from the list of standard algorithms: SVM, EPF, SCMK, R2MK, ASMGSSK, MsuperPCA, 2DSSA, 2DMSSA.

McNemar's test between the proposed SP-SSA algorithm and the algorithms listed above for the Indian Pines, Pavia University, Salinas, and Houston 2018 datasets are provided in Table 6. The test result clearly reveals that the classification results for the

proposed method were significantly better—in a McNemar's statistical sense—compared with other approaches.

Table 6. Statistics of the McNemar Test for the Indian Pines, Pavia University, Salinas, and Houston 2018 datasets.

Z	Indian Pines	Pavia University	Salinas	Houston 2018
	Proposed Method (SP-SSA)			
SVM	42.534	56.342	37.215	61.512
EPF	39.152	48.186	25.113	57.084
SCMK	27.467	37.428	21.421	43.115
R2MK	23.615	28.521	18.472	39.721
ASMGSSK	10.624	16.832	8.351	18.521
MsuperPCA	21.524	19.441	11.486	35.431
2DSSA	34.321	31.084	15.321	51.322
2DMSSA	16.819	23.217	9.091	27.634

3.5. Advantage of Proposed Method over 2D-SSA

3.5.1. Applying SP-SSA on General Images

In the proposed approach, 2D-SSA is applied on each and every superpixel segmented region. Hence, it can be considered as a local 2D-SSA approach that can extract accurate spatial information on each single object. In the case of global 2D-SSA, features are over-smoothed, and features are not prominent for specific classes. In local 2D-SSA instead, object-specific texture information can be highlighted. In Figure 15, the popular cameraman image and an artificial test image are used to demonstrate the effectiveness of the proposed approach over the 2D-SSA approach.

When the cameraman image is reconstructed using the 2D-SSA method, the Mean Square Error (MSE) comes out to 115.8865; however, when the same image is reconstructed using the proposed SP-SSA approach, the MSE reduces to 93.0468. A similar behavior is also observed with the test image. With the proposed SP-SSA method, the MSE reduces to 237.1038 from 287.5323. This signifies that the proposed method can reconstruct an image with minimum error and can effectively integrate local information during the reconstruction process.

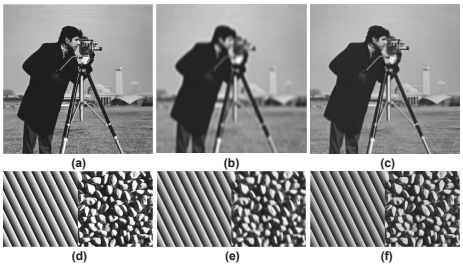

Figure 15. (**a**) Cameraman image (**b**) 2D-SSA Reconstructed image [MSE = 115.8865] (**c**) SP-SSA reconstructed image [MSE = 93.0468] (**d**) Test image (**e**) 2D-SSA Reconstructed image [MSE = 287.5323] (**f**) SP-SSA reconstructed image [MSE = 237.1038].

3.5.2. Applying SP-SSA on HSI

The HSI is composed of a stack of 2D images carrying valuable information about each spectral band. To demonstrate the effectiveness of the proposed method, a randomly selected spectral band at 667 nm was considered for our analysis. Figure 16b,c contains the scene as reconstructed by *2D-SSA* and *SP-SSA*, respectively. Since the HSI was acquired over a large area, it includes multiple objects with different textural information. This is a typical case where object-specific reconstruction works better than direct reconstruction.

Textural information can be highlighted accurately by using local reconstruction as opposed to global reconstruction. The error in SP-SSA-based reconstruction is indeed lower as compared to 2D-SSA-based reconstruction. The same conclusion can also be drawn from Figure 16.

In the case of 2D-SSA-based reconstruction, the Mean Square Error (MSE) is 612.4349, while, in the case of SP-SSA-based reconstruction, the MSE is 504.5685. Figure 16d,e contains the difference image for 2D-SSA-based reconstruction and SP-SSA-based methods. It can be clearly observed that edge information is preserved with the proposed method. The SP-SSA-based reconstruction is applied to all spectral bands and generates a modified hypercube with preserved local structure information and minimum noise level. These latter features generally lead to better classification performance.

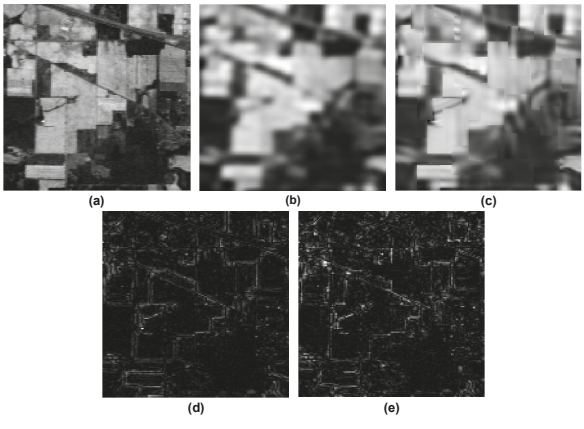

Figure 16. (**a**) Original scene at band 667 nm (**b**) Reconstructed scene by 2D-SSA (**c**) Reconstructed scene by SP-SSA (**d**) Difference image for the 2D-SSA reconstructed scene (**e**) Difference image for the SP-SSA reconstructed scene.

4. Conclusions and Future Scope

Feature extraction is one of the most crucial steps in HSI classification. It is essential to capture comprehensive spatial and spectral information for accurate feature extraction. For image reconstruction, the conventional 2D-SSA algorithm usually extracts spatial features directly by applying the embedding window to the entire image. However, HSI scenes frequently encompass a broader area and contain several items. As a result, spatial information pertaining to local objects must be recovered. To solve this problem, in the proposed method, a superpixel-based SSA technique was presented, which can capture the object specific spatio-spectral information accurately.

In this work, the original HSI was first divided into various semantic sub-regions by the superpixel segmentation algorithm. Next, each segment was reconstructed individually by applying 2D-SSA. The generated reconstructed HSI was then classified using the SVM classifier, and the final classification map was produced. Local characteristics may be collected effectively in the suggested method since 2D-SSA is applied at the superpixel level. However, two parameters must be adjusted: the amount of superpixels and the embedding window size. Future developments will aim at finding the optimal criteria to determine the parameters of the procedure and to investigate relationships between the characteristics of the HSI and quality of the results.

Author Contributions: Conceptualization, P.K.B. and R.P.; methodology, S.S.; software, R.P. and S.S.; validation, S.S., R.P. and P.K.B.; formal analysis, S.S.; investigation, S.S. and R.P.; resources, F.D. and P.K.B.; data curation, S.S.; writing—original draft preparation, S.S.; writing—review and editing, F.D.; visualization, S.S. and F.D.; supervision, F.D.; project administration, F.D. and P.K.B. All authors have read and agreed to the published version of the manuscript.

Funding: This research received no external funding.

Institutional Review Board Statement: Not applicable.

Informed Consent Statement: Not applicable.

Data Availability Statement: Publicly available datasets have been utilized for conducting the experiments. Details are provided in the text of the paper.

Conflicts of Interest: The authors declare no conflict of interest.

References

1. Imani, M.; Ghassemian, H. An overview on spectral and spatial information fusion for hyperspectral image classification: Current trends and challenges. *Inf. Fusion* **2020**, *59*, 59–83. [CrossRef]
2. Fabiyi, S.D.; Vu, H.; Tachtatzis, C.; Murray, P.; Harle, D.; Dao, T.K.; Andonovic, I.; Ren, J.; Marshall, S. Varietal classification of rice seeds using RGB and hyperspectral images. *IEEE Access* **2020**, *8*, 22493–22505. [CrossRef]
3. Fox, N.; Parbhakar-Fox, A.; Moltzen, J.; Feig, S.; Goemann, K.; Huntington, J. Applications of hyperspectral mineralogy for geoenvironmental characterisation. *Miner. Eng.* **2017**, *107*, 63–77. [CrossRef]
4. Chen, Y.; Zhu, K.; Zhu, L.; He, X.; Ghamisi, P.; Benediktsson, J.A. Automatic design of convolutional neural network for hyperspectral image classification. *IEEE Trans. Geosci. Remote Sens.* **2019**, *57*, 7048–7066. [CrossRef]
5. Bitar, A.W.; Cheong, L.F.; Ovarlez, J.P. Sparse and low-rank matrix decomposition for automatic target detection in hyperspectral imagery. *IEEE Trans. Geosci. Remote Sens.* **2019**, *57*, 5239–5251. [CrossRef]
6. Tu, B.; Wang, J.; Kang, X.; Zhang, G.; Ou, X.; Guo, L. KNN-based representation of superpixels for hyperspectral image classification. *IEEE J. Sel. Top. Appl. Earth Obs. Remote Sens.* **2018**, *11*, 4032–4047. [CrossRef]
7. Melgani, F.; Bruzzone, L. Classification of hyperspectral remote sensing images with support vector machines. *IEEE Trans. Geosci. Remote Sens.* **2004**, *42*, 1778–1790. [CrossRef]
8. Li, J.; Bioucas-Dias, J.M.; Plaza, A. Spectral–spatial hyperspectral image segmentation using subspace multinomial logistic regression and Markov random fields. *IEEE Trans. Geosci. Remote Sens.* **2011**, *50*, 809–823. [CrossRef]
9. Lv, Q.; Niu, X.; Dou, Y.; Xu, J.; Lei, Y. Classification of hyperspectral remote sensing image using hierarchical local-receptive-field-based extreme learning machine. *IEEE Geosci. Remote Sens. Lett.* **2016**, *13*, 434–438. [CrossRef]
10. Chen, Y.; Nasrabadi, N.M.; Tran, T.D. Hyperspectral image classification using dictionary-based sparse representation. *IEEE Trans. Geosci. Remote Sens.* **2011**, *49*, 3973–3985. [CrossRef]
11. Rodarmel, C.; Shan, J. Principal component analysis for hyperspectral image classification. *Surv. Land Inf. Sci.* **2002**, *62*, 115–122.
12. Wang, J.; Chang, C.I. Independent component analysis-based dimensionality reduction with applications in hyperspectral image analysis. *IEEE Trans. Geosci. Remote Sens.* **2006**, *44*, 1586–1600. [CrossRef]
13. Bandos, T.V.; Bruzzone, L.; Camps-Valls, G. Classification of hyperspectral images with regularized linear discriminant analysis. *IEEE Trans. Geosci. Remote Sens.* **2009**, *47*, 862–873. [CrossRef]
14. Ma, L.; Crawford, M.M.; Tian, J. Local manifold learning-based *k*-nearest-neighbor for hyperspectral image classification. *IEEE Trans. Geosci. Remote Sens.* **2010**, *48*, 4099–4109. [CrossRef]
15. Patro, R.N.; Subudhi, S.; Biswal, P.K.; Dell'Acqua, F. A Review on Unsupervised Band Selection Techniques: Land Cover Classification for Hyperspectral Earth Observation Data. *IEEE Geosci. Remote Sens. Mag.* **2021**, *9*, 72–111. [CrossRef]
16. Patro, R.N.; Subudhi, S.; Biswal, P.K. Spectral clustering and spatial Frobenius norm-based Jaya optimisation for BS of hyperspectral images. *IET Image Process.* **2019**, *13*, 307–315. [CrossRef]
17. Benediktsson, J.A.; Palmason, J.A.; Sveinsson, J.R. Classification of hyperspectral data from urban areas based on extended morphological profiles. *IEEE Trans. Geosci. Remote Sens.* **2005**, *43*, 480–491. [CrossRef]
18. Dalla Mura, M.; Benediktsson, J.A.; Waske, B.; Bruzzone, L. Morphological attribute profiles for the analysis of very high resolution images. *IEEE Trans. Geosci. Remote Sens.* **2010**, *48*, 3747–3762. [CrossRef]
19. Ghamisi, P.; Dalla Mura, M.; Benediktsson, J.A. A survey on spectral–spatial classification techniques based on attribute profiles. *IEEE Trans. Geosci. Remote Sens.* **2015**, *53*, 2335–2353. [CrossRef]
20. Guo, X.; Huang, X.; Zhang, L. Three-dimensional wavelet texture feature extraction and classification for multi/hyperspectral imagery. *IEEE Geosci. Remote Sens. Lett.* **2014**, *11*, 2183–2187.
21. Huang, X.; Liu, X.; Zhang, L. A multichannel gray level co-occurrence matrix for multi/hyperspectral image texture representation. *Remote Sens.* **2014**, *6*, 8424–8445. [CrossRef]
22. Ye, Z.; Fowler, J.E.; Bai, L. Spatial–spectral hyperspectral classification using local binary patterns and Markov random fields. *J. Appl. Remote Sens.* **2017**, *11*, 035002. [CrossRef]

23. Jia, S.; Shen, L.; Li, Q. Gabor feature-based collaborative representation for hyperspectral imagery classification. *IEEE Trans. Geosci. Remote Sens.* **2015**, *53*, 1118–1129.
24. Tomasi, C.; Manduchi, R. Bilateral filtering for gray and color images. In Proceedings of the Sixth International Conference onComputer Vision, Bombay, India, 4–7 January 1998; pp. 839–846.
25. Sun, W.; Messinger, D.W. Trilateral filter on multispectral imagery for classification and segmentation. In *Algorithms and Technologies for Multispectral, Hyperspectral, and Ultraspectral Imagery XVII*; International Society for Optics and Photonics: Bellingham, WA, USA, 2011; Volume 8048, p. 80480Y.
26. Kang, X.; Li, S.; Benediktsson, J.A. Spectral–spatial hyperspectral image classification with edge-preserving filtering. *IEEE Trans. Geosci. Remote Sens.* **2014**, *52*, 2666–2677. [CrossRef]
27. Kang, X.; Li, S.; Benediktsson, J.A. Feature extraction of hyperspectral images with image fusion and recursive filtering. *IEEE Trans. Geosci. Remote Sens.* **2014**, *52*, 3742–3752. [CrossRef]
28. Subudhi, S.; Patro, R.; Biswal, P.K. Bilateral kernel extraction from pca for classification of hyperspectral images. *PFG–J. Photogramm. Remote Sens. Geoinf. Sci.* **2019**, *87*, 205–221. [CrossRef]
29. Zabalza, J.; Ren, J.; Zheng, J.; Han, J.; Zhao, H.; Li, S.; Marshall, S. Novel two-dimensional singular spectrum analysis for effective feature extraction and data classification in hyperspectral imaging. *IEEE Trans. Geosci. Remote Sens.* **2015**, *53*, 4418–4433. [CrossRef]
30. Zabalza, J.; Qing, C.; Yuen, P.; Sun, G.; Zhao, H.; Ren, J. Fast implementation of two-dimensional singular spectrum analysis for effective data classification in hyperspectral imaging. *J. Frankl. Inst.* **2018**, *355*, 1733–1751. [CrossRef]
31. Ma, P.; Ren, J.; Zhao, H.; Genyun, S.; Murray, P.; Zheng, J. Multiscale 2D singular spectrum analysis and principal component analysis for spatial-spectral noise-robust feature extraction and classification of hyperspectral images. *IEEE J. Sel. Top. Appl. Earth Obs. Remote Sens.* **2020**, *14*, 1233–1245. [CrossRef]
32. Fu, H.; Sun, G.; Ren, J.; Zhang, A.; Jia, X. Fusion of PCA and Segmented-PCA Domain Multiscale 2-D-SSA for Effective Spectral-Spatial Feature Extraction and Data Classification in Hyperspectral Imagery. *IEEE Trans. Geosci. Remote Sens.* **2020**. [CrossRef]
33. Subudhi, S.; Patro, R.N.; Biswal, P.K.; Dell'Acqua, F. A Survey on Superpixel Segmentation as a Preprocessing Step in Hyperspectral Image Analysis. *IEEE J. Sel. Top. Appl. Earth Obs. Remote Sens.* **2021**, *14*, 5015–5035. [CrossRef]
34. Fang, L.; Li, S.; Duan, W.; Ren, J.; Benediktsson, J.A. Classification of hyperspectral images by exploiting spectral–spatial information of superpixel via multiple kernels. *IEEE Trans. Geosci. Remote Sens.* **2015**, *53*, 6663–6674. [CrossRef]
35. Liu, J.; Wu, Z.; Xiao, Z.; Yang, J. Region-based relaxed multiple kernel collaborative representation for hyperspectral image classification. *IEEE Access* **2017**, *5*, 20921–20933. [CrossRef]
36. Sun, L.; Ma, C.; Chen, Y.; Shim, H.J.; Wu, Z.; Jeon, B. Adjacent superpixel-based multiscale spatial-spectral kernel for hyperspectral classification. *IEEE J. Sel. Top. Appl. Earth Obs. Remote Sens.* **2019**, *12*, 1905–1919. [CrossRef]
37. Jiang, J.; Ma, J.; Chen, C.; Wang, Z.; Cai, Z.; Wang, L. SuperPCA: A superpixelwise PCA approach for unsupervised feature extraction of hyperspectral imagery. *IEEE Trans. Geosci. Remote Sens.* **2018**, *56*, 4581–4593. [CrossRef]
38. Chen, Y.; Lin, Z.; Zhao, X.; Wang, G.; Gu, Y. Deep learning-based classification of hyperspectral data. *IEEE J. Sel. Top. Appl. Earth Obs. Remote Sens.* **2014**, *7*, 2094–2107. [CrossRef]
39. Chen, Y.; Zhao, X.; Jia, X. Spectral–spatial classification of hyperspectral data based on deep belief network. *IEEE J. Sel. Top. Appl. Earth Obs. Remote Sens.* **2015**, *8*, 2381–2392. [CrossRef]
40. Chen, Y.; Jiang, H.; Li, C.; Jia, X.; Ghamisi, P. Deep feature extraction and classification of hyperspectral images based on convolutional neural networks. *IEEE Trans. Geosci. Remote Sens.* **2016**, *54*, 6232–6251. [CrossRef]
41. Mou, L.; Ghamisi, P.; Zhu, X.X. Deep recurrent neural networks for hyperspectral image classification. *IEEE Trans. Geosci. Remote Sens.* **2017**, *55*, 3639–3655. [CrossRef]
42. Zhu, L.; Chen, Y.; Ghamisi, P.; Benediktsson, J.A. Generative adversarial networks for hyperspectral image classification. *IEEE Trans. Geosci. Remote Sens.* **2018**, *56*, 5046–5063. [CrossRef]
43. Stutz, D.; Hermans, A.; Leibe, B. Superpixels: An evaluation of the state-of-the-art. *Comput. Vis. Image Underst.* **2018**, *166*, 1–27. [CrossRef]
44. Achanta, R.; Shaji, A.; Smith, K.; Lucchi, A.; Fua, P.; Süsstrunk, S. SLIC superpixels compared to state-of-the-art superpixel methods. *IEEE Trans. Pattern Anal. Mach. Intell.* **2012**, *34*, 2274–2282. [CrossRef] [PubMed]
45. Xue, Z.; Zhou, S.; Zhao, P. Active learning improved by neighborhoods and superpixels for hyperspectral image classification. *IEEE Geosci. Remote Sens. Lett.* **2018**, *15*, 469–473. [CrossRef]
46. Tarabalka, Y.; Fauvel, M.; Chanussot, J.; Benediktsson, J.A. SVM-and MRF-based method for accurate classification of hyperspectral images. *IEEE Geosci. Remote Sens. Lett.* **2010**, *7*, 736–740. [CrossRef]
47. Chi, M.; Bruzzone, L. Semisupervised classification of hyperspectral images by SVMs optimized in the primal. *IEEE Trans. Geosci. Remote Sens.* **2007**, *45*, 1870–1880. [CrossRef]
48. Chang, C.C.; Lin, C.J. LIBSVM: A library for support vector machines. *ACM Trans. Intell. Syst. Technol.* **2011**, *2*, 1–27. [CrossRef]

applied sciences

MDPI

Review

Spatial Analysis for Landscape Changes: A Bibliometric Review

Maria Danese * and Dario Gioia

Institute of Cultural Heritage-National Council of Research, C.da S. Loja, Tito Scalo, 85100 Potenza, Italy; dario.gioia@cnr.it
* Correspondence: maria.danese@cnr.it; Tel.: +39-0971427324

Abstract: The main aim of this study is to analyze from a bibliometric point of view the research trend in spatial analysis for landscape changes using the records published in the Web of Science database in the last twenty years. Several parameters such as documents published per year, sources of documents, number of citations as well as VOSviewer software and GIS are used for the analysis of different metrics such as the number of citations, co-authorship network, and keyword occurrences. Analysis of the number of papers, their keywords, and authorships countries shows the research trend in the specific topics of the spatial analysis for landscape changes and consequently can constitute a benchmark for researchers who approach this research topic.

Keywords: spatial analysis; landscape changes; bibliometric mapping; Web of Science

Citation: Danese, M.; Gioia, D. Spatial Analysis for Landscape Changes: A Bibliometric Review. *Appl. Sci.* **2021**, *11*, 10078. https://doi.org/10.3390/app112110078

Academic Editor: Nadia Giuffrida

Received: 24 September 2021
Accepted: 25 October 2021
Published: 27 October 2021

1. Introduction

Spatial analysis saw a big improvement in the last few decades thanks to the parallel growth of Information Computer Technologies (ICT), both from the hardware and from the software development point of view. Since then, many research fields have been taking advantage of the spatial analysis discipline. Between these, there are all the studies directly concerned with human- and natural-induced landscape changes. Bibliometric analysis of "hot" research topics is a growing tool for the investigation of emerging disciplines, cooperations, publication impact, and new research trends [1]. In recent years, such an approach has been adopted by several authors to quantitatively delineate the global trend of different research topics or wider disciplines [2–6], highlighting the usefulness of the method to study the past and future direction of research patterns. Moreover, the recent availability of wider databases and innovative software of bibliometric analysis provides new tools for the deeper visual and statistical analysis of temporal and geographic global distribution in research trends [1]. In this work, we carry out a bibliometric analysis of the emerging research topic of the spatial analysis of landscape changes with the aim to investigate the topic's research pattern in the last two decades and to guide researchers to understand future trends.

Landscape changes are very important for the past, present, and future of the Earth and consequently for human life; consequently, as it is shown in this paper, the study of landscape changes through the help of spatial analysis has grown in recent decades and become a hot topic. For this reason, there are many articles belonging to the Ecology, Territorial Planning and Earth Science sectors. Just some examples of the themes afforded in these areas are papers that use spatial analysis for understanding how landscape changes impact species distribution over space and their interaction with environments [7,8], the quantification of natural resources, such as water [9], forests [10–12], and, more in general, of ecosystem services [13,14], and multi-temporal analysis of satellite images and maps as a tool to reconstruct land-use changes and rates of geomorphological processes [15–17]. One of the most effective approaches to investigate natural landscape changes is the geomorphological one, which benefits from recent advances in the development of software

and algorithms of digital elevation model (DEM) comparison [18,19], image change detection [20,21], and landscape evolution models [22–25]. Moreover, sustainability is a big topic connected with this research line and there are many articles concerning it [26–28], together with analysis connected to climate change [29–31] and pollution quantification [32–34]. However, there are other disciplines such as Archaeology or Historical studies [35–37], or fire analysis [38–40], that are strictly connected to the wider topic of landscape changes.

From what has been said, it is now clear that to consider "spatial analysis for landscape changes" (from here s.a.l.c.) implies covering a very broad area because there are many topics and, at the same time, there are many types of spatial analysis that could be used to investigate these changes, from more traditional methods [41] to more intelligent data analysis [42].

Consequently, the main aim of this paper is to clarify topics, trends, and methods that are connected to the research line of s.a.l.c. through a comprehensive and accurate bibliometric analysis during the last twenty years.

2. Methodology

2.1. Bibliometric Search Engine, Tools, and Software Used for S.A.L.C. Analysis

To retrieve the scientific literature for this paper, we used the Web of Science database (WoS). Among the most popular bibliographic databases of research papers such as Scopus, WoS, and Google Scholar, we chose WoS because it represents the best compromise among database completeness and cataloguing of higher rank journals [43].

This research was conducted by using the combination of s.a.l.c. keywords, written between the quotation marks, in order to include at the same time all the four keywords and by looking for them inside the title, abstract, and keywords of the scientific paper. Then, the analysis excluded from the research all the WoS categories including the life science disciplines, such as biotechnology, applied microbiology, immunology, oncology, etc.

Regarding the time of publication, two temporal ranges were considered.

The first range considers years from 2001 to 2020, in order to study the general characteristics of scientific literature in the highlighted topic.

The second range considers the same period, from 2001 to 2020, but is divided into four five-year intervals, in order to investigate the long-term literature trends.

To achieve this goal, the following tools were used: first, some tools present inside WoS were used to extract some statistics and graphs; second, an open-source Geographic Information System, QGIS (open source software, downloadable at the site https://www.qgis.org/it/site/, accessed on 10 October 2021), was used to analyze the geographic distribution of selected works; third, for more specific diagrams, the VOSviewer software was used. It is a free software [44] based on text-mining and it is useful to construct bibliometric maps.

The bibliometric mapping discipline, also called science mapping, recently appeared in order to look for relationships between documents, keywords, or authors [45,46], and with the main aim to investigate the structure and the dynamics of a topic [1,47].

In the literature, other software programs exist for bibliometric mapping, such as SCImat [48] or CiteSpace [49]. Some software reviews are present in [50,51]. We chose VOSviewer for its simplicity, flexibility, and clearness of the results.

2.2. VOSviewver Diagrams

Concerning the use of VOSviewer, it offers many useful tools for bibliographic analysis. In this paper, the following diagrams were used:

- The keyword co-occurrence map. It is a distance graph showing the connection between the keywords included in the selected bibliography. If the terms co-occur inside the same phrases, a higher relevance score is assigned to them. Consequently, terms that are linked and near each other in the map are more related. With the co-occurrence map, it is then possible to analyze the main keywords that characterize the state of the art in a domain field. With this type of analysis, VOSviewer returns the

graph showing links between key terms, which are also divided into clusters; these clusters are in turn built up on the basis of the co-occurrences of terms inside the paper titles. Moreover, the number of occurrences and the total link strength are associated with each term.

- The co-authorship cluster map. In this diagram, the countries where the authors belong are represented as nodes. A bigger node consequently means that more authors come from that country. Lines instead represent the relationship between co-authors coming from different countries.
- The overlay map between keyword co-occurrences and the year when the papers of the studied bibliography were mostly cited. As in the previous maps, nodes and their sizes still represent the number of keyword occurrences, and the lines still represent the strength of co-occurrences between terms, but in this case, the colors represent the citation year.
- Density visualization of the co-occurrences map. This type of graphic facilitates the reading of hot-spots and cold-spots of the keyword with a higher or lower density of co-occurrences [44].

3. Results

3.1. General Quantitative Results

The first result, obtained from the research in Web of Science, is the quantification of the citations and publications existing in the research field s.a.l.c. A total of 8409 records were found, with a minimum of 86 in 2001 and a maximum of 862 in 2020. Figure 1 shows a consistent increase both in the publication and in the citation number, except for two light drops between years 2002–2003 and 2016–2017. There was also a little decrease in 2020. However, we have to remember that 2020 was an exceptional year because of the COVID-19 pandemic, and this could influence the number and the topic of the worldwide research papers.

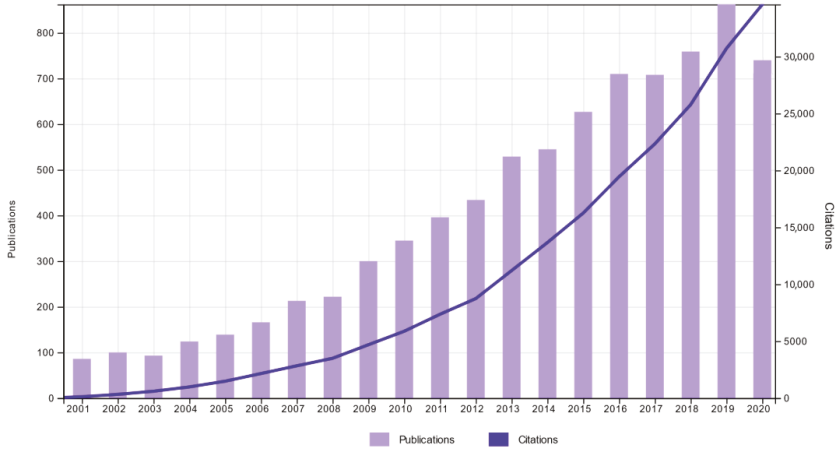

Figure 1. Diagram representing the number of citations and publications reported by Web of Science from 2000 to 2020.

3.2. Result Heterogeneity

In the results obtained by Web of Science, the first aspect that emerges, as expected and explained in the introduction, is the heterogeneity of categories. This aspect is clearly highlighted in Figure 2, where the composition of the first ten categories is visualized in a tree map. Visual inspection of the map highlights that the main categories working in these sectors are environmental disciplines such as Environmental Sciences (in 1st place

with 2349 documents, corresponding to 27.6% of the total data), Ecology (2nd place, 2337, 27.4%), Multidisciplinary Geosciences (3rd place, 1323, 15.5%), and Physical Geography (4th place, 1236, 14.5%). Moreover, it is possible to discover a first trend, not directly asked with the query conducted in the Web of Science database. In fact, categories such as Remote Sensing (873, 10.2%) and the Imaging Science Photographic Technology categories (528, 6.2%) are, respectively, classified in 5th and 9th place, suggesting the first delineation of the main techniques and approaches related to the s.a.l.c.

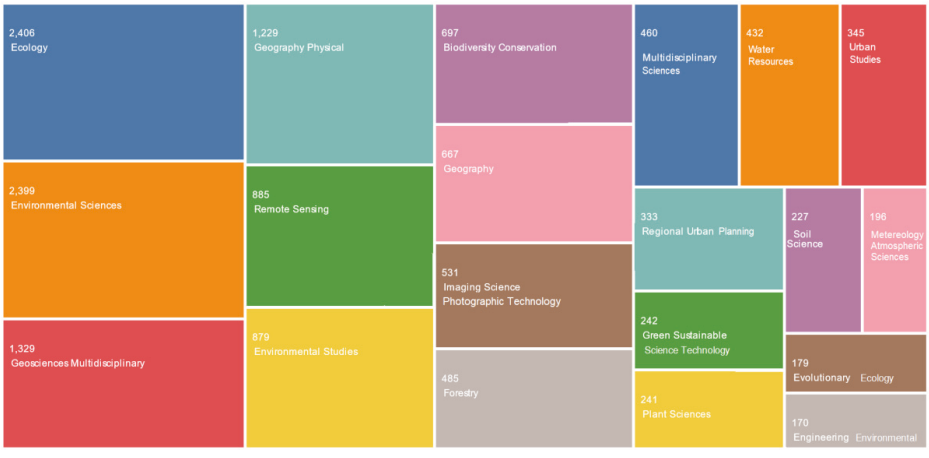

Figure 2. Tree map of the first twenty Web of Science categories where the works about spatial analysis for landscape archaeology are published.

3.3. Spatial Distribution of S.A.L.C.

S.a.l.c. literature authorship is spatially distributed all around the world, even if a preliminary analysis of the results indicates a relevant prevalence of European-related papers coming from 129 different countries. Figure 3 shows the frequency of documents found for each country and classified in deciles. The first five countries interested in the research area are the United States of America (with 2765 documents, 32.9%), China (1205, 14.3%), Germany (888, 10.0%), the United Kingdom (836, 10.0%), and Canada (628, 7.5%). It is worth noting that the countries that seem not involved in the research topics and present zero articles or very few articles (1 or 2) are prevalently located in the African continent.

It is also interesting to look at the co-authorship map between countries (Figure 4), and the four main geographical clusters found that are those with the following rank: (1st) the USA, (2nd) China, (3rd) Germany, and (4th) the Netherlands.

3.4. Co-Occurrence Map of Keywords of the Whole Period

Concerning the co-occurrence map calculated in the period between 2016 and 2020, four main clusters were found. The prevailing keywords of these clusters are the following (the number of the cluster is just nominal, not ordinal):

- Cluster 1 (Figure 5a, red cluster, a total of 40 items): the keyword with the most occurrences is climate change (1323). Here, secondary terms, besides the word climate (349), express the different aspects of landscape connected to climate change, from vegetation (573) to soil (146) and its erosion (97).
- Cluster 2 (Figure 5a, green cluster, a total of 69 items): the "head" or main terms are biodiversity (769 occurrences), pattern (896), and conservation (778), while minor terms are diversity (428), ecology (330), fragmentation (367), landscape ecology (152), habitat (231), connectivity (190), and landscape connectivity (86). It is interesting to note that the keyword "spatial autocorrelation" (94) was inserted in this cluster

instead of the "method" cluster (the Cluster 3), even if, of course, the link with it remains through keywords GIS, land-use change, remote sensing, and, most of all, urbanization, which is strictly linked with topics such as the protection or conservation of biodiversity.

- Cluster 3 (Figure 5a, blue cluster, a total of 62 items): here it is possible to highlight two sub-clusters. The first one is prevalently a methodological one, with the main terms GIS (502) and remote sensing (427). The second one is more related to the urban and planning application fields, represented by the main words land-use change (666) and urbanization (431). Terms linked to both are representative of the types of analysis conducted and the instrument used, such as classification (359), the different names of remote sensors, change detection (104), spatial metrics (44), and simulation (165). Moreover, other secondary terms explain where these methods are applied: for urban growth studies (117) and urban expansion (79).
- Cluster 4 (Figure 5a, light green cluster, a total of 40 items): the main word is landscape (1172), while secondary terms are management (560), impact (629), ecosystem services (362), indicators (170), and vulnerability (112). As it is also possible to see from the other minor terms, it is a cluster more oriented to the evaluation of landscape resources, sustainability, and resilience.

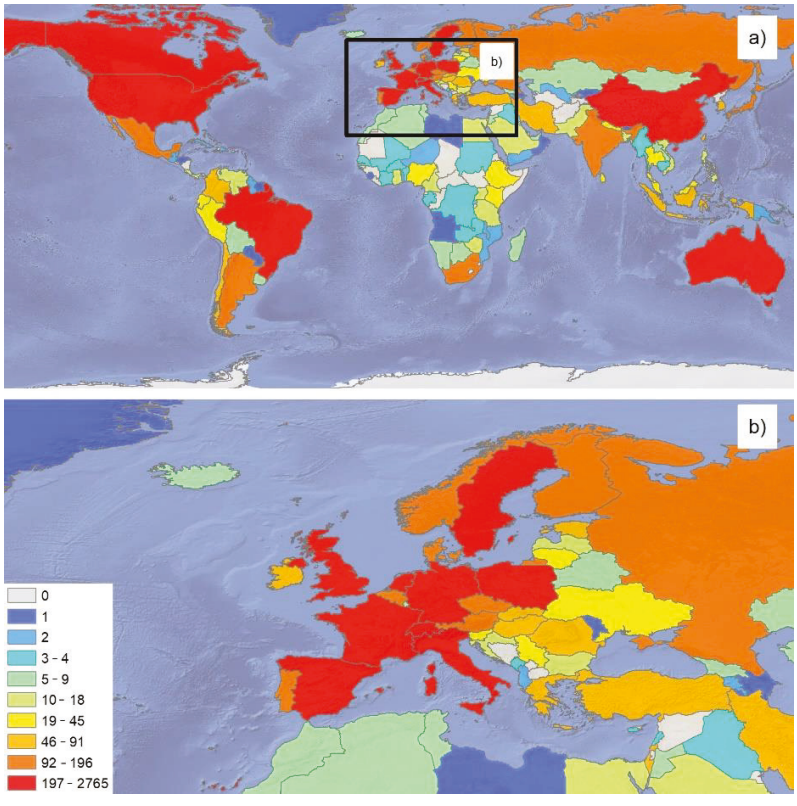

Figure 3. Spatial distribution of the countries of article authorship (**a**) in the World and (**b**) in Europe. World background taken from @ naturalearthdata.com. The graph was extracted using QGIS software.

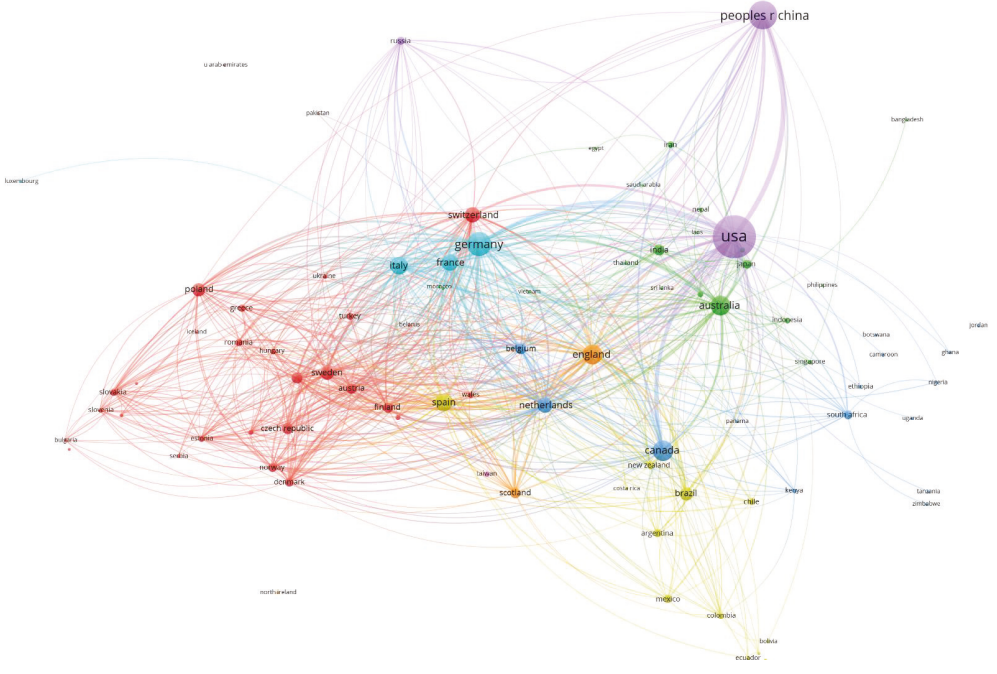

Figure 4. Co-authorship cluster map. Graph obtained by VOSviewer software.

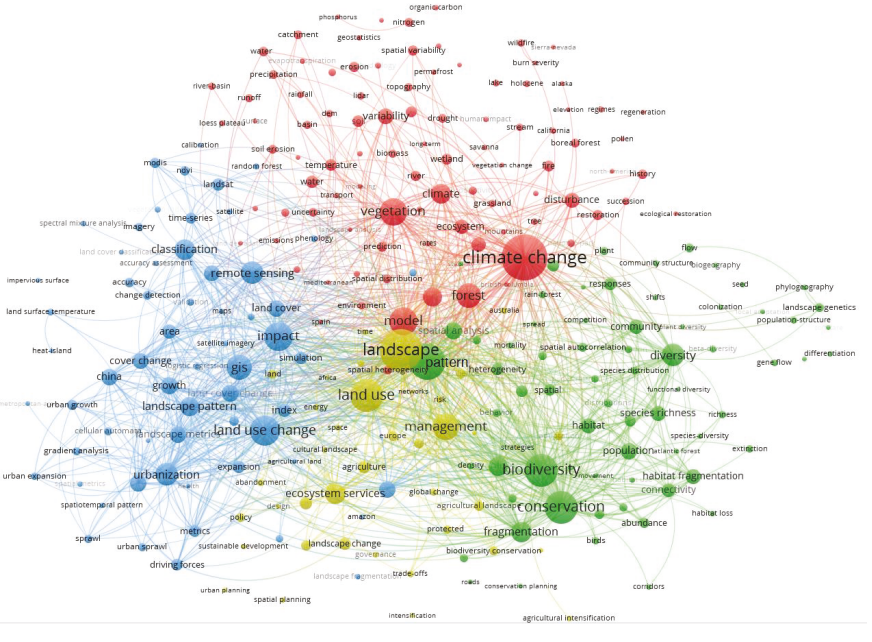

(**a**)

Figure 5. *Cont*.

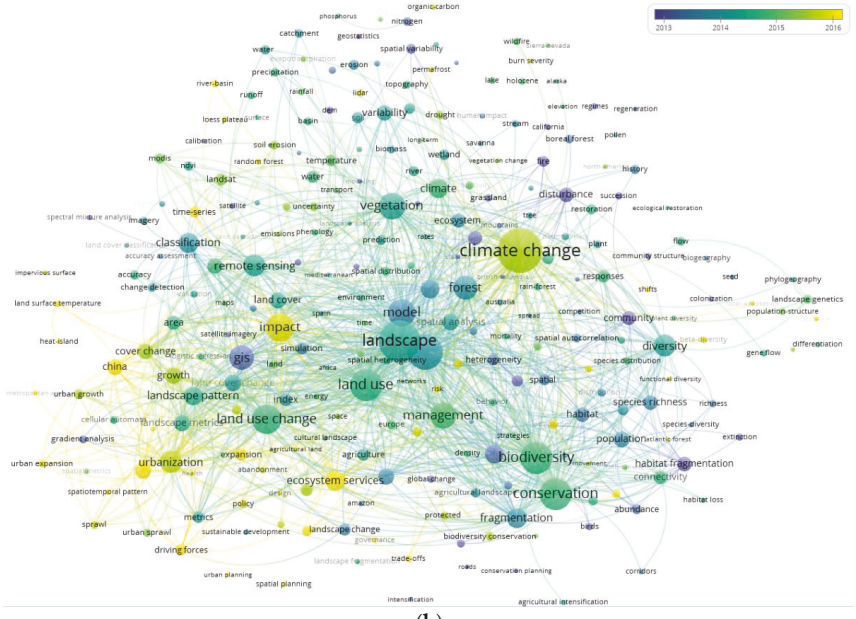

(**b**)

Figure 5. (**a**) Co-occurrence map (period: 2001–2020); (**b**) overlay visualization between key terms and their citation year. Graphs made with VOSviewer software.

By "main word", we meant words with the major frequencies clustered by the software.

Together with the co-occurrence map, we extracted a map where the overlay between terms and the citation year is shown (Figure 5b): it shows the most cited keywords over the years. In the legend, in particular, the years between 2012 and 2016 are highlighted because this is the temporal range with the largest number of citations. In particular, the most recently cited keywords since 2016 are climate change and ecosystem service, while "older" ones (and actually, they are still consolidated in the literature) are GIS and remote sensing.

3.5. Density Map for Interval of 5 Years

In order to investigate the trend in s.a.l.c. research topics on a shorter-term period, we extracted the density map of keywords for four different intervals of 5 years. The interpretation of the maps (Figure 6) could become clearer with the help of data and histograms reported in Figure 7, where occurrence frequencies of the keywords are reported and schematized. Visual inspection of the maps suggests that the two common keywords in the top five list are "landscape" and "pattern". These two words are clearly connected to the main topic of this research. Instead, we can see, for the first two temporal blocks (2001–2005 and 2006–2010), that the other keywords are "model" and "GIS", which are related to the methodological aspects of the research. These two terms, in particular, have a great increase in the second time block (i.e., from 2006 to 2010). Here, the keyword "climate change" also appears. The latter becomes more significant in the third block (2011–2015) and also increases in the 2016–2020 interval. The keyword "climate change" is further reinforced by the last keyword of the top five list, respectively, in 2011–2015, with the terms "biodiversity" and "conservation", and in 2016–2020, with the terms "impact" and, again, "conservation".

Finally, Figure 7 shows the number of occurrences and the related histograms of the keywords already cited in Section 3.4, which considers the most important terms for each

cluster found in the total period between 2001 and 2020. This is performed to observe the trend of main keywords (in bold, Figure 7) and some of the secondary keywords.

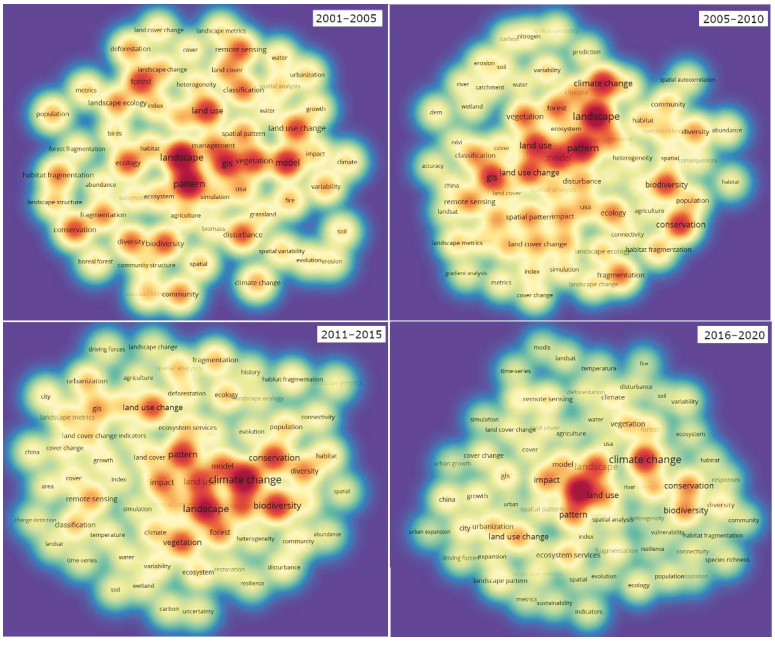

Figure 6. Density map. Obtained with VOSviewer.

	Keyword	2001–2005	2006–2010	2011–2015	2016–2020
Cluster 1	**climate change**	36	135	407	62
	climate	0	0	90	188
	vegetation	10	83	190	264
	soil	12	23	40	67
	erosion	24	29	0	0
Cluster 2	**biodiversity**	65	102	253	383
	pattern	13	169	245	417
	conservation	31	117	227	402
	diversity	26	64	140	197
	ecology	24	70	95	133
	fragmentation	19	78	101	164
	model	13	126	161	269
	landscape ecolog	14	42	38	0
	habitat	0	46	80	88
	connectivity	0	190	56	97
	spatial autocorre	0	20	0	0
Cluster 3	**GIS**	19	125	120	211
	remote sensing	12	69	120	208
	land use change	15	99	188	345
	urbanization	11	50	99	268
	classification	38	66	99	168
	change detection	0	0	36	0
	spatial metrics	0	0	0	44
	simulation	12	36	39	76
	urban growth	0	0	0	71
	urban expansion	0	0	0	64
Cluster 4	**landscape**	15	203	328	572
	management	14	68	174	295
	impact	17	61	162	392
	ecosystem servic	0	0	80	271
	indicator	0	0	46	99
	vulnerability	0	0	0	70

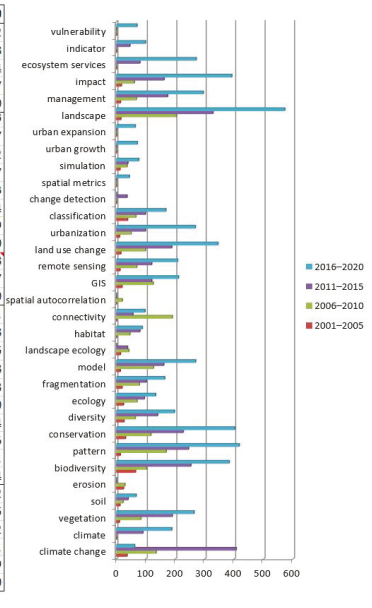

Figure 7. Occurrences and related histograms for the main keywords observed in the 2001–2020 period in order to observe their trend in the four periods.

3.6. Types of Spatial Analysis

Although spatial analysis is a relatively broad term adopted for different and wide research disciplines, an analysis of keywords can be useful to extract information about the main methods and approaches used in s.a.l.c research. To this aim, data were cleaned manually and only keywords concerning methods were left in the analysis. Moreover, keywords with a broader meaning such as "spatial analysis", "remote sensing", or "geospatial analysis" were excluded.

A synoptic scheme of such an analysis is reported in Figure 8, where one can observe the overlay between the co-occurrences map and its overlay with the publication year. Table 1 shows the first 50 keywords, in order of importance for their occurrences: the two top keywords represent, respectively, the traditional method used to analyze a landscape and one of the more innovative methods. In fact, the keyword "classification" (359 occ.) can be correlated to the results of the landscape analysis, whereas the second one (i.e., "simulation", 205 occ.) has a strong connection with the approaches adopted for the validation of the results or landscape modeling. Other relevant keywords are the tools used by spatial analysis, such as "indicators" (170 occ.) and "metrics" (156 occ.), or more innovative and specific methods such as "cellular automaton" (113 occ.), "change detection" (104 occ.), "spatial autocorrelation" (103 occ.), "gradient analysis" (84 occ.), "species distribution model" (82 occ.), and "regression" (80 occ.). Among them, "cellular automation" is maybe the most innovative, since has been recently introduced and represents a spatially distributed evolution of artificial intelligence algorithms. Finally, in 10th place, we find the term "(DEM, 72 occ.)", which represents the basic elements of most of the landscape analysis approaches. Additional information about research trends in the s.a.l.c. topic can be inferred from the temporal variation of the keyword occurrences: for example, the prevalence of keywords such as DEM, statistical analysis, data analysis, or regression in the 2012–2013 period (blue tones in Figure 8) seems to suggest research approaches mainly based on visual inspection and basic statistical analysis, while the appearance of peculiar terms in 2016 such as random forest, Markov chain, machine learning, or cellular automata clearly indicates a transition toward the automatic or semi-automatic classification of landscape changes.

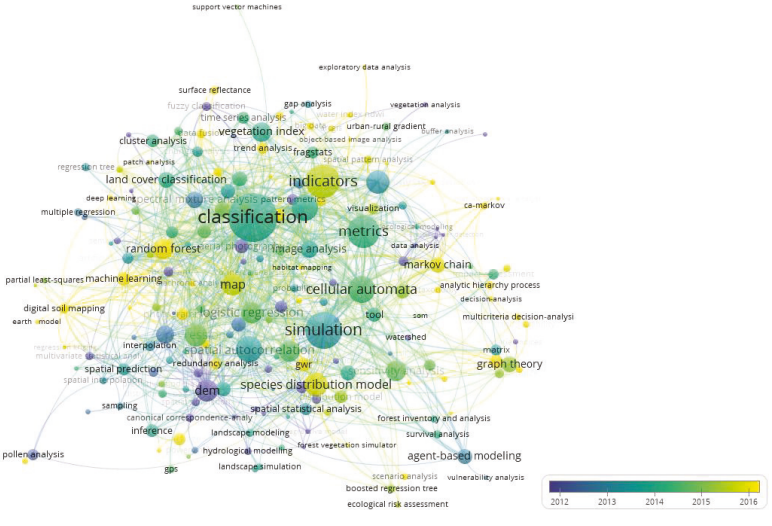

Figure 8. Overlay map for the types of spatial analysis more occurrent in s.a.l.c. research topic. Made with VOSviewer.

Table 1. First 100 keywords with the highest number of occurrences.

Keyword	Occ.[1]	Keyword	Occ.
01 classification	359	26 agent-based modeling	34
02 simulation	205	27 statistical analysis	34
03 indicators	170	28 autocorrelation	33
04 metrics	156	29 aerial photography	32
05 cellular automata	113	30 pattern analysis	32
06 change detection	104	31 tool	32
07 spatial autocorrelation	103	32 hot spot analysis	31
08 gradient analysis	84	33 leaf index	31
09 species distribution model	82	34 geographically weighted regression	30
10 regression	80	35 machine learning	29
11 DEM	72	36 segmentation	29
12 map	71	37 network analysis	28
13 density	70	38 inference	27
14 logistic regression	67	39 cluster analysis	26
15 random forest	65	40 distribution model	26
16 sensitivity analysis	62	41 intensity	25
17 vegetation index	60	42 fractal	24
18 geostatistics	51	43 neural network	23
19 image analysis	45	44 r-package	23
20 spectral mixture analysis	44	45 spatial statistical analysis	23
21 land cover classification	40	46 fragstats	22
22 graph theory	37	47 photogrammetry	22
23 Markov chain	36	48 spatial prediction	22
24 object-based classification	36	49 time series analysis	22
25 pca	35	50 swat	21

[1] Occurrences.

4. Discussion and Concluding Remarks

In this paper, a detailed bibliometric investigation of the research trend in spatial analysis for landscape changes using the records published in the Web of Science database in the last twenty years was carried out. Such an approach has been widely used to drive scientists that need to understand the hot topic of a research field or territory (see, for example, [2–4,52–54]).

Our analysis was conducted with the help of three different software packages: the analysis utility offered by WoS, a GIS software (QGIS), and a specific software for bibliometric mapping, VOSviewer. The results highlight that the topic has received increasing attention in the last two decades. As a matter of fact, we observed a constant and exponential increase in the number of papers and citations since 2000. Such an increase can be partly ascribed to: (i) the growing availability of high-resolution DEMs and remote sensing images; (ii) automatic tools or algorithms of landscape classification and the analysis of land-use changes.

Our results also suggest that the research topic is multidisciplinary, ranging from different disciplines such as Environmental Sciences, Earth Sciences, and Ecology, and it is mainly conducted by Chinese, European, and North American research groups. Moreover, on the basis of the statistical analysis of keyword occurrences, it is possible to reconstruct the following main research patterns:

- The literature concerning climate change and the different aspects connected to it, such as the changes in vegetation and soil, grows in particular in the second decade. In spite of this, in the twenty years considered here, we observe the largest pattern in keywords and the highest number of citations;
- The more representative disciplinary areas are urban and territorial planning and ecology. There are two bigger keyword clusters, respectively, headed by land-use changes and biodiversity, conservation and patterns. Additionally, this area shows an increase in occurrences in all the analyzed periods;

- A third interesting research pattern shows that the two previously cited fields (i.e., urban and territorial planning and ecology) are not considered only as two separated sectors, but there is a correct trial to integrate them with management, impact estimation, and, most of all, with the diffusion of ecosystem services. Such a trend can be mainly observed in recent years;
- Analysis of the frequency distribution of keywords and their temporal trend seems to reveal a modification in the research focus: in particular, the prevalence of keywords such as "Remote Sensing", GIS, and "Land Use" in the early 20th century suggests a methodological approach mainly based on visual inspection or basic GIS analysis of DEMs and satellite images. The spreading of terms such as "classification" or "simulation" and the appearance of keywords such as "cellular automation", "artificial neural network", or "random forest" indicate a clear modification of the research methods, which evolve toward computer-based automation or unsupervised detection of landscape patterns and changes;
- Considering the availability of algorithms and tools useful for fast and accurate analysis of landscape changes in larger areas, we argue that the disciplines/research fields such as geomorphology and the digital reconstruction of historical landscapes could have a relevant growth in the next few years. For example, similar topics can benefit from the growing availability of landscape evolution models [25,55,56] and tools for the visual analysis and reconstruction of historical landscapes [57,58].

To achieve a deeper understanding of the research trend, each map in a wide research field such as s.a.l.c. would request a widening of the analysis and the reading of results in the different clusters and thematic areas identified. This would provide enough material for many other future studies in order to identify an internal state of the art and trends of those subsectors.

Author Contributions: Conceptualization, M.D. and D.G.; methodology, M.D. and D.G.; software, M.D and D.G.; validation, M.D. and D.G.; formal analysis, M.D. and D.G.; investigation, M.D. and D.G.; resources, M.D. and D.G.; data curation, M.D. and D.G.; writing—original draft preparation, M.D. and D.G.; writing—review and editing, M.D. and D.G.; visualization, M.D. and D.G. All authors have read and agreed to the published version of the manuscript.

Funding: This research received no external funding.

Institutional Review Board Statement: Not applicable.

Informed Consent Statement: Not applicable.

Data Availability Statement: All the data used in this paper can be found at the Web of Science search engine (https://www.webofscience.com/wos/woscc/basic-search, accessed on 10 October 2021).

Conflicts of Interest: The authors declare no conflict of interest.

References

1. Noyons, E.C.M.; Moed, H.F.; Luwel, M. Combining mapping and citation analysis for evaluative bibliometric purposes: A bibliometric study. *J. Am. Soc. Inf. Sci.* **1999**, *50*, 115–131. [CrossRef]
2. Bezak, N.; Mikoš, M.; Borelli, P.; Alewell, C.; Alvarez, P.; Alexandre, J.; Anache, A.; Baartman, J.; Ballabio, C.; Biddoccu, M.; et al. Soil erosion modelling: A bibliometric analysis. *Environ. Res.* **2021**, *197*, 111087. [CrossRef]
3. Su, X.; Li, X.; Kang, Y. A Bibliometric Analysis of Research on Intangible Cultural Heritage Using CiteSpace. *SAGE Open* **2019**, *9*, 2158244019840119. [CrossRef]
4. Niu, B.; Yuan, J.; Peng, S.; Zhang, X. Global trends in sediment-related research in earth science during 1992–2011: A bibliometric analysis. *Scientometrics* **2014**, *98*, 511–529. [CrossRef]
5. Gariano, S.L.; Guzzetti, F. Landslides in a changing climate. *Earth-Sci. Rev.* **2016**, *162*, 227–252. [CrossRef]
6. Reichenbach, P.; Rossi, M.; Malamud, B.D.; Mihir, M.; Guzetti, F. A review of statistically-based landslide susceptibility models. *Earth-Sci. Rev.* **2018**, *180*, 60–91. [CrossRef]
7. Frey, S.; Fisher, J.T.; Burton, A.C. Investigating animal activity patterns and temporal niche partitioning using camera-trap data: Challenges and opportunities. *Remote Sens. Ecol. Conserv.* **2017**, *3*, 123–132. [CrossRef]

8. Kay, S.L.; Fischer, J.W.; Monaghan, A.J.; Beasley, J.C.; Boughton, R.; Campbell, T.A.; Cooper, S.M.; Ditchkoff, S.S.; Hartley, S.B.; Kilgo, J.C.; et al. Quantifying drivers of wild pig movement across multiple spatial and temporal scales. *Mov. Ecol.* **2017**, *5*, 14. [CrossRef]
9. Lin, L.; Li, M.; Chen, H.; Lai, X.; Zhu, H.; Wang, H. Integrating landscape planning and stream quality management in mountainous watersheds: A targeted ecological planning approach for the characteristic landscapes. *Ecol. Indic.* **2020**, *117*, 106557. [CrossRef]
10. Brock, P.M.; Fornace, K.M.; Grigg, M.J.; Anstey, N.M.; William, T.; Cox, J.; Drakeley, C.J.; Ferguson, H.M.; Kao, R.R. Predictive analysis across spatial scales links zoonotic malaria to deforestation. *Proc. R. Soc. B Biol. Sci.* **2019**, *286*, 20182351. [CrossRef]
11. Lin, Y.; Hu, X.; Zheng, X.; Hou, X.; Zhang, Z.; Zhou, X.; Qiu, R.; Lin, J. Spatial variations in the relationships between road network and landscape ecological risks in the highest forest coverage region of China. *Ecol. Indic.* **2019**, *96*, 392–403. [CrossRef]
12. Zhou, W.Q.; Zhang, S.; Yu, W.J.; Wang, J.; Wang, Q. Effects of Urban Expansion on Forest Loss and Fragmentation in Six Megaregions, China. *Remote Sens.* **2017**, *9*, 991. [CrossRef]
13. Garcia-Nieto, A.P.; Geijzendorffer, I.R.; Baro, F.; Roche, P.K.; Bondeau, A.; Cramer, W. Impacts of urbanization around Mediterranean cities: Changes in ecosystem service supply. *Ecol. Indic.* **2018**, *91*, 589–606. [CrossRef]
14. Wang, J.; Zhou, W.; Pickett, S.T.A.; Yu, W.; Li, W. A multiscale analysis of urbanization effects on ecosystem services supply in an urban megaregion. *Sci. Total Environ.* **2019**, *662*, 824–833. [CrossRef] [PubMed]
15. Gioia, D.; Amodio, A.M.; Maggio, A.; Sabia, C.A. Impact of Land Use Changes on the Erosion Processes of a Degraded Rural Landscape: An Analysis Based on High-Resolution DEMs, Historical Images, and Soil Erosion Models. *Land* **2021**, *10*, 673. [CrossRef]
16. Nampak, H.; Pradhan, B.; Rizeei, H.M.; Park, H.J. Assessment of land cover and land use change impact on soil loss in a tropical catchment by using multitemporal SPOT-5 satellite images and Revised Universal Soil Loss Equation model. *Land Degrad. Dev.* **2018**, *29*, 3440–3455. [CrossRef]
17. Fortugno, D.; Boix-Fayos, C.; Bombino, G.; Denisi, P.; Quinonero Rubio, J.M.; Tamburino, V.; Zema, D.A. Adjustments in channel morphology due to land-use changes and check dam installation in mountain torrents of Calabria (southern Italy). *Earth Surf. Process. Landf.* **2017**, *42*, 2469–2483. [CrossRef]
18. Han, S.H. Thematic map construction of erosion and deposition in rivers using GIS-based DEM comparison technique. *J. Korean Soc. Surv. Geod. Photogramm. Cartogr.* **2016**, *34*, 153–159. [CrossRef]
19. Hugenholtz, C.H.; Whitehead, K.; Brown, O.W.; Barchyn, T.E.; Moornam, B.J.; LeClair, A.; Riddell, K.; Hamilton, T. Geomorphological mapping with a small unmanned aircraft system (sUAS): Feature detection and accuracy assessment of a photogrammetrically-derived digital terrain model. *Geomorphology* **2013**, *194*, 16–24. [CrossRef]
20. Anders, N.S.; Seijmonsbergen, A.C.; Bouten, W. Geomorphological change detection using object-based feature extraction from multioral lidar data. *IEEE Geosci. Remote Sens. Lett.* **2013**, *10*, 1587–1591. [CrossRef]
21. Conforti, M.; Mercuri, M.; Borrelli, L. Morphological changes detection of a large earthflow using archived images, lidar-derived dtm, and uav-based remote sensing. *Remote Sens.* **2021**, *13*, 120. [CrossRef]
22. Coulthard, T.J.; van de Wiel, M.J. Modelling long term basin scale sediment connectivity, driven by spatial land use changes. *Geomorphology* **2017**, *277*, 265–281. [CrossRef]
23. Ramirez, J.A.; Zischg, A.P.; Schürmann, S.; Zimmerman, M.; Weingartner, R.; Coulthard, T.; Keiler, M. Modeling the geomorphic response to early river engineering works using CAESAR-Lisflood. *Anthropocene* **2020**, *32*, 100266. [CrossRef]
24. Gioia, D.; Schiattarella, M. Modeling Short-Term Landscape Modification and Sedimentary Budget Induced by Dam Removal: Insights from LEM Application. *Appl. Sci.* **2020**, *10*, 7697. [CrossRef]
25. Gioia, D.; Lazzari, M. Testing the Prediction Ability of LEM-Derived Sedimentary Budget in an Upland Catchment of the Southern Apennines, Italy: A Source to Sink Approach. *Water* **2019**, *11*, 991. [CrossRef]
26. Broto, V.C. Energy landscapes and urban trajectories towards sustainability. *Energy Policy* **2017**, *108*, 755–764. [CrossRef]
27. Cumming, G.S.; Morrison, T.H.; Hughes, T.P. New Directions for Understanding the Spatial Resilience of Social-Ecological Systems. *Ecosystems* **2017**, *20*, 649–664. [CrossRef]
28. Zhou, W.; Pickett, S.T.A.; Cadenasso, M.L. Shifting concepts of urban spatial heterogeneity and their implications for sustainability. *Landsc. Ecol.* **2017**, *32*, 15–30. [CrossRef]
29. Ackerly, D.D.; Loarie, S.R.; Cornwell, W.K.; Weiss, S.B.; Hamilton, H.; Branciforte, R.; Kraft, N.J.B. The geography of climate change: Implications for conservation biogeography. *Divers. Distrib.* **2010**, *16*, 476–487. [CrossRef]
30. Post, E.; Stenseth, N.C. Climatic variability, plant phenology, and northern ungulates. *Ecology* **1999**, *80*, 1322–1339. [CrossRef]
31. Sork, V.L.; Aitken, S.N.; Dyer, R.J.; Eckert, A.J.; Legendre, P.; Neale, D.B. Putting the landscape into the genomics of trees: Approaches for understanding local adaptation and population responses to changing climate. *Tree Genet. Genomes* **2013**, *9*, 901–911. [CrossRef]
32. Weng, Q.; Yang, S. Urban Air Pollution Patterns, Land Use, and Thermal Landscape: An Examination of the Linkage Using GIS. *Environ. Monit. Assess.* **2006**, *117*, 463–489. [CrossRef]
33. Liu, Y.; Wu, J.; Yu, D. Characterizing spatiotemporal patterns of air pollution in China: A multiscale landscape approach. *Ecol. Indic.* **2017**, *76*, 344–356. [CrossRef]
34. Volk, M.; Hirschfeld, J.; Dehnhardt, A.; Schmidt, G.; Bohn, C.; Liersch, S.; Gassman, P.W. Integrated ecological-economic modelling of water pollution abatement management options in the Upper Ems River Basin. *Ecol. Econ.* **2008**, *66*, 66–76. [CrossRef]

35. Kantner, J. The Archaeology of Regions: From Discrete Analytical Toolkit to Ubiquitous Spatial Perspective. *J. Archaeol. Res.* **2007**, *16*, 37–81. [CrossRef]
36. Banerjee, R.; Srivastava, P.K. Reconstruction of contested landscape: Detecting land cover transformation hosting cultural heritage sites from Central India using remote sensing. *Land Use Policy* **2013**, *34*, 193–203. [CrossRef]
37. Fyfe, R.M. Bronze Age landscape dynamics: Spatially detailed pollen analysis from a ceremonial complex. *J. Archaeol. Sci.* **2012**, *39*, 2764–2773. [CrossRef]
38. Conedera, M.; Tinner, W.; Neff, C.; Meurer, M.; Dickens, A.F.; Krebs, P. Reconstructing past fire regimes: Methods, applications, and relevance to fire management and conservation. *Quat. Sci. Rev.* **2009**, *28*, 555–576. [CrossRef]
39. Keane, R.E.; Cary, G.J.; Davies, I.D.; Flannigan, M.; Gardner, R.H.; Lavorel, S.; Lenihan, J.M.; Li, C.; Rupp, T. A classification of landscape fire succession models: Spatial simulations of fire and vegetation dynamics. *Ecol. Model.* **2004**, *179*, 3–27. [CrossRef]
40. Niklasson, M.; Granstrom, A. Numbers and sizes of fires: Long-term spatially explicit fire history in a Swedish boreal landscape. *Ecology* **2000**, *81*, 1484–1499. [CrossRef]
41. Seto, K.C.; Fragkias, M. Quantifying spatiotemporal patterns of urban land-use change in four cities of China with time series landscape metrics. *Landsc. Ecol.* **2005**, *20*, 871–888. [CrossRef]
42. Parker, D.C.; Manson, S.; Janssen, M.A.; Hoffmann, M.J.; Deadman, P. Multi-Agent Systems for the Simulation of Land-Use and Land-Cover Change: A Review. *Ann. Assoc. Am. Geogr.* **2003**, *93*, 314–337. [CrossRef]
43. Pranckutė, R. Web of Science (WoS) and Scopus: The Titans of Bibliographic Information in Today's Academic World. *Publications* **2021**, *9*, 12. [CrossRef]
44. van Eck, N.J.; Waltman, L. Software survey: VOSviewer, a computer program for bibliometric mapping. *Scientometrics* **2010**, *84*, 523–538. [CrossRef]
45. Small, H. Visualizing science by citation mapping. *J. Am. Soc. Inf. Sci.* **1999**, *50*, 799–813. [CrossRef]
46. Morris, S.A.; Van Der Veer Martens, B. Mapping research specialties. *Annu. Rev. Inf. Sci. Technol.* **2008**, *42*, 213–295. [CrossRef]
47. Börner, K.; Chen, C.; Boyack, K.W. Visualizing knowledge domains. *Annu. Rev. Inf. Sci. Technol.* **2003**, *37*, 179–255. [CrossRef]
48. Cobo, M.J.; López-Herrera, A.G.; Herrera-Viedma, E.; Herrera, F. SciMAT: A new science mapping analysis software tool. *J. Am. Soc. Inf. Sci. Technol.* **2012**, *63*, 1609–1630. [CrossRef]
49. Chen, C. CiteSpace II: Detecting and visualizing emerging trends and transient patterns in scientific literature. *J. Am. Soc. Inf. Sci. Technol.* **2006**, *57*, 359–377. [CrossRef]
50. Cobo, M.J.; López-Herrera, A.G.; Herrera-Viedma, E.; Herrera, F. Science mapping software tools: Review, analysis, and cooperative study among tools. *J. Am. Soc. Inf. Sci. Technol.* **2011**, *62*, 1382–1402. [CrossRef]
51. Moral-Muñoz, J.A.; López-Herrera, A.G.; Herrera-Viedma, E.; Cobo, M.J. Science mapping analysis software tools: A review. In *Springer Handbook of Science and Technology Indicators*; Springer: Cham, Switzerland, 2019; pp. 159–185.
52. Gizzi, F.T.; Proto, M.; Potenza, M.R. The Basilicata region (Southern Italy): A natural and 'human-built' open-air laboratory for manifold studies. Research trends over the last 24 years (1994–2017). *Geomat. Nat. Hazards Risk* **2019**, *10*, 433–464. [CrossRef]
53. Odenwald, S.F. A citation study of earth science projects in citizen science. *PLoS ONE* **2020**, *15*, e0235265. [CrossRef] [PubMed]
54. Agapiou, A.; Lysandrou, V. Remote sensing archaeology: Tracking and mapping evolution in European scientific literature from 1999 to 2015. *J. Archaeol. Sci. Rep.* **2015**, *4*, 192–200. [CrossRef]
55. Poeppl, R.; Coulthard, T.; Keesstra, S.; Keiler, M. Modeling the impact of dam removal on channel evolution and sediment delivery in a multiple dam setting. *Int. J. Sediment Res.* **2019**, *34*, 537–549. [CrossRef]
56. Hancock, G.; Coulthard, T.; Martinez, C.; Kalma, J. An evaluation of landscape evolution models to simulate decadal and centennial scale soil erosion in grassland catchments. *J. Hydrol.* **2011**, *398*, 171–183. [CrossRef]
57. Danese, M.; Biscione, M.; Coluzzi, R.; Lasaponara, R.; Murgante, B.; Masini, N. An integrated methodology for medieval landscape reconstruction: The case study of Monte Serico. In Proceedings of the International Conference on Computational Science and Its Applications, Seoul, Korea, 29 June–2 July 2009; Springer: Berlin/Heidelberg, Germany, 2009; pp. 320–340.
58. Roubis, D.; Sogliani, F.; Gabellone, F.; Danese, M.; Gnesi, D. Archaeological Landscapes through GIS (Cost Surface Analysis) and Virtual Reality, A case study on the monastic site of Jure Vetere (Calabria—Italy). In Proceedings of the 36th CAA Conference—On the Road to Reconstructing the Past. Computer Applications and Quantitative Methods in Archaeology, Budapest, Hungary, 2–6 April 2008.

MDPI
St. Alban-Anlage 66
4052 Basel
Switzerland
Tel. +41 61 683 77 34
Fax +41 61 302 89 18
www.mdpi.com

Applied Sciences Editorial Office
E-mail: applsci@mdpi.com
www.mdpi.com/journal/applsci

MDPI
St. Alban-Anlage 66
4052 Basel
Switzerland

Tel: +41 61 683 77 34
Fax: +41 61 302 89 18

www.mdpi.com

ISBN 978-3-0365-2863-2